Control Volume Analysis of Rectangular Ducts with Arbitrary Mean-Flow, Transverse Wall Impedances, and Temperature Discontinuity

by

Connor D. Morehead

A thesis submitted to the Graduate Faculty of
Auburn University
in partial fulfilment of the
requirements for the Degree of Master of Science

Auburn, Alabama
May 2, 2020

Keywords: Control, Volume, Analysis, Acoustics, Combustion, Instability

Approved by
Dr. David E. Scarborough, Chair, Assistant Professor of Aerospace Engineering
Dr. Roy J. Hartfield, Walt and Virginia Woltosz Professor of Aerospace Engineering
Dr. Vinamra Agrawal, Assistant Professor of Aerospace Engineering

Abstract

Combustion instabilities (CIs) are a consistent and ubiquitous problem for industrial burners, rockets, and gas turbines. Reduced order acoustic models are often used to analyze combustion instabilities. Typically, reduced order models incorporate a few important parameters based on the application and are limited in complexity by design. Combining a small number of parameters quickly causes the underlying equations to become untenable, necessitating the use of numerical methods, computational models, and experimentation. Therefore, reduced order models which include many relevant parameters that are still computationally inexpensive are desirable. This thesis proposes a linear control volume analysis (CVA) based around the assumptions of linear acoustics and planar acoustic wave propagation. Transverse wall impedance, axial mean-flow, and transverse mean flow are explicitly accounted for in the derivation. The resulting governing equation imbeds three-dimensional information from the transverse wall impedance, axial mean flow, and transverse mean flow into a plane wave solution. Thus, the effects of transverse wall impedance, axial mean-flow, and transverse mean flow can be investigated directly. The governing equation developed from the CVA equation reduces to the classical analytical wave equation in one dimension when eliminating the wall impedances and mean flow. The CVA is applied to two duct acoustic problems: a closed – closed duct and a constant mass flow-rate – nozzle duct. These application problems include the effects of transverse wall impedance, axial mean-flow, transverse mean-flow, and temperature.

Acknowledgements

I would like to thank my Dr. Scarborough and my committee, Dr. Hartfield and Dr. Agrawal, for their continued guidance and patience.

I would like to thank my girlfriend Isabelle, whom without I would never have come close to finishing. She is the North Star of my life, and this thesis is no exception to that.

I would also like to thank my family, particularly my parents, Carol and Dan, and my grandparents, Charles David and Marcia, for their continual support and love.

Table of Contents

List of Tables

List of Figures

List of Symbols

a	=	Speed of sound
A	=	Forward acoustic plane wave pressure coefficient
B	=	Rearward acoustic plane wave pressure coefficient
C	=	Forward acoustic plane wave velocity coefficient or generic constant of integration
D	=	Length, rearward acoustic plane wave velocity coefficient, or the convective derivative
e	=	Mathematical constant e
f	=	Frequency or general function
i	=	Imaginary unit, index
I	=	Identity matrix
j	=	Integer
k	=	Wavenumber
m	=	Integer
M	=	Mach number

n = Unit vector, integer

$\mathcal{O}$ = Bachmann – Landau order symbol

p = Pressure

q = Heat release

S = Surface area

t = Time

T = Temperature, separation of variables solution, or Lighthill's tensor

v = Velocity

V = Volume

x = Transverse coordinate or placeholder variable

X = Separation of variables solution

y = Transverse coordinate or placeholder variable

Y = Separation of variables solution

z = Axial coordinate

Z = Acoustic impedance or separation of variables solution

$\mathcal{Z}$ = Normalized acoustic impedance

$\mathbb{Z}$ = Set of all integers

β = Placeholder variable

γ	=	Adiabatic index
δ	=	Prefix for infinitesimal quantities or Kronecker delta
Δ	=	Laplacian
η	=	Displacement or time dependent coefficients used in Galerkin Series
θ	=	Acoustic resistance
ξ	=	Control volume analysis parameters
π	=	Mathematical constant pi
ρ	=	Density
σ	=	Cauchy stress tensor
τ	=	Traceless part of the Cauchy stress tensor
Y	=	Axial flow velocity coefficient
Υ	=	Normalized axial flow velocity coefficient
χ	=	Acoustic reactance
ψ	=	Eigen-solution used in Galerkin series or placeholder variable
ω	=	Angular frequency
∂	=	Partial derivative
∇	=	Del operator
$\otimes$	=	Outer product

Subscripts, Superscripts, and Other Accents

β_b = Baseline case

β_{co} = Cut-off quantity

β_{CS} = Control surface

β_{CV} = Control volume

β_{Mun} = Refers to Munjal's solution

$\beta_{r/i}$ = Real and imaginary component, respectively

β_t = Transverse quantity

$\beta_{x/y}$ = Transverse component, x or y

β_z = Axial component

β_0 = Steady component

$\beta_{1/2/etc}$ = Refers to specific control surfaces or sub-ducts

$\beta^{\pm}$ = Forward or rearward travelling wave component, respectively

β' = Unsteady component or partial derivative

$\dot{\beta}$ = Time rate of change

$\hat{\beta}$ = Unit vector

$\vec{\beta}$ = Vector

$\underline{\beta}$ = Matrix

$\xi_{v/M}$ = Transverse mean-flow parameter in its non-normalized and normalized forms, respectively

$\xi_{Z/\mathcal{Z}}$ = Transverse impedance parameter in its non-normalized and normalized forms, respectively

Chapter 1

Introduction

Combustion instabilities are a physical phenomenon that occurs when perturbations in the heat release rate of the combustion process couples with perturbations in the acoustic field within the combustor. The acoustic and heat release rate oscillations form a feedback loop in which the amplitude of oscillations grow. These violent oscillations reduce the lifespan of engine components and can even damage or destroy the combustor itself.

Historically, combustion driven oscillations were first observed in 1777 in the form of "singing flames" by Higgins [1]. Combustion instabilities were nothing more than an academic curiosity until the advent of internal combustion engines. Since then, combustion instabilities have been observed in many types of combustors, but they are a particularly prevalent in industrial furnaces, rockets, and gas turbines. Combustion instabilities in these systems can cause thrust oscillations, enhanced thermal stresses to combustor walls, and mechanical loads that cause cycle fatigue in system components [2]. These issues can easily cause damage to expensive combustors, themselves part of bigger systems. Therefore, there has been considerable research into the prediction and mitigation of combustion instabilities in many different types of systems.

The combustion instability feedback loop can be broken into three steps. Heat release rate fluctuations add energy into the acoustic field and cause acoustic and velocity fluctuations. These fluctuations then excite flow oscillations and fuel/oxidizer oscillations. These oscillations then perturb the heat release further which completes the cycle [2].

Combustion instabilities were first described mathematically by Rayleigh in his seminal work *The Theory of Sound* [3]. Rayleigh's observations on combustion instabilities are encapsulated in Rayleigh's criterion shown below:

$$\int p' \dot{q} \, dt \, dV > 0 \tag{1.0.1}$$

In equation (1.0.1) p' is the unsteady pressure and $\dot{q}$ is the unsteady heat release. If the unsteady heat release is in phase with the unsteady acoustic pressure, energy will be dumped into the system and the oscillations will grow in amplitude. Such a system is linearly unstable. If p' and $\dot{q}$ are out of phase, energy is removed from the system (e.g. damping) and therefore the system is linearly stable. It is important to note that Rayleigh's criterion is used when analyzing linear stability of combustion systems. In linearly unstable systems, the amplitude of oscillations will increase unless a non-linear damping mechanism exists. In this case the oscillations will reach a limit cycle when the non-linear damping is equal to the driving provided by the combustion instability. This thesis does not consider non-linear effects.

To analyze combustion instabilities, both combustion and acoustics are considered. Investigations of CI's can be divided into 3 categories: reduced order, numerical, and experimental methods. Reduced methods are any method which uses simplifying assumptions to reduce the complexity of the governing equations. Reduced order methods need not be analytical, and very often must be solved numerically due to the inherent complexity of acoustics, fluid dynamics, and combustion. Reduced order methods are attractive due to the low computational cost and physical insight contained within the solution. Due to the complexity of combustion systems analytical options quickly become untenable. In such cases, numerical techniques are used. Numerical methods take the governing equations and numerically solve them, yielding high accuracy

solutions at an appropriately high computational cost. Numerical solutions do not provide the same physical insight into the solution that analytical solutions provide. As computational tools become more sophisticated and powerful, numerical methods have become increasingly popular. Computational fluid dynamics (CFD), a numerical method, has become a commonly used tool in modern engineering practice [4]. Lastly are experimental efforts. Experimental efforts are typically very costly, but the data they provide is invaluable, as they serve to validate analytical and numerical approaches and to extend the field with new observations of combustion phenomena. Experimental methods will not be discussed in this paper. For recent reviews of combustion instabilities see [2] and [5].

This thesis is primarily concerned with reduced order methods. Despite the advantages and prevalent use of numerical approaches when dealing with CIs, reduced order methods are still desirable to help understand the physics of a given CI problem. Analytical methods can also be integrated into design tools to offer fast and "ballpark" results to expedite the design phase. Finally, reduced order models are often combined with an acoustic network model of 1D acoustic elements which allows reduced order models to approximate more complex systems. As such, there is merit in studying reduced order approaches to CIs.

Chapter 2

Background and Literature Review

This section begins with a brief survey of the relevant the literature, specifically targeting the development of the acoustic boundary condition and higher-dimensional non-numerical analyses. This is followed by an introduction to a few relevant acoustics concepts in relation to combustion. Next is a small overview of the acoustic wave equations. This is followed by considering numerous acoustic boundary conditions. The chapter ends by looking at two common solution methods for dealing with inhomogeneous wave equations, and briefly outlines the control volume analysis carried out in subsequent chapters.

2.1 - Literature Review

The traditional analytical approach to acoustics problems is to develop and solve the acoustic wave equation. For full detail on the derivation, see refs [6], [7], and [8]. Approaches to CIs can be broken down in terms of the dimensionality, i.e. 1D, 2D, 3D. 1D approaches are common due to their relative simplicity. A one-dimensional acoustic analysis was first used in application to combustion instabilities by Merk [9]. This method has been applied to a variety of systems [10, 11, 12, 13]. When considering higher order dimensions, numerical methods are often used. It is possible to use an acoustic network of 1D acoustic elements to describe CI problems in 3 dimensions [14]. Analytical acoustic analyses which feature multi-dimensional effects are only available in simple geometries. Efforts to include a non-uniform mean flow profile includes work by Rienstra [15] which solves Pridmore-Brown equation in 2D and axisymmetric 3D lined ducts.

The impedance of a boundary is sufficient to describe the acoustic boundary conditions without flow. The acoustic boundary condition in the presence of flow was first derived by Ingard [16] then generalized by Myers [17]. They described how the impedance of a boundary is affected by mean flow grazing past it. This boundary condition has been shown to be mathematically ill-posed in ref [18], and has also been shown to fail by experiment [19] as well. A modification of this boundary condition to include an inviscid boundary layer was proposed by separately by Brambley [20], and Rienstra and Darau [21], both accurate to first order. Brambley used the method of matched asymptotic expansions to account for the inviscid boundary layer and Rienstra and Darau assumed the presence of a finite boundary layer with a given thickness. Auregan et al. [22] also modified the Myer's condition by introducing a term that accounts for the effects of a viscous boundary layer. Gabard [23] performs a comparison between the two proposed inviscid modifications and compared them with an exact numerical solution and found that the modification by Brambley is a suitable correction to the Myer's condition. Khamis and Brambley [24] proposed a modification of Brambley's original modification which is accurate to second order. Khamis and Brambley derived a corrected Myers boundary condition including viscous effects from the linearized compressible Navier-Stokes equations [25]. In a subsequent paper, they confirmed the analysis by Gabard and showed very close agreement between their derived viscous condition and numerical results [26].

2.2 - Acoustics in Combustion

The interactions between acoustics and combustion is complicated. In the derivation of the wave equation with combustion, the energy equation is considered. An analytical model of flame-acoustic interactions from first principles is unavailable, so approximate methods are used. One common method is to use flame transfer functions. Flame transfer functions describe the amplitude

and phase of the flame response to acoustic disturbances as a function of frequency. A simple and often used flame transfer function is the n-τ model. In the n-τ model the unsteady heat release is related to velocity disturbances based on a time lag τ. It is then a simple matter to insert the unsteady heat release into the governing equations. A downside to using flame transfer functions is they must be scaled and validated through experimentation.

Another common technique used in CI modelling problems is the transfer matrix method (TMM). The method discretizes a system into individual regions. In each region, approximations are made that reduce the complexity of the problem. Between each element there are a set of matching conditions between state variables. Each set therefore has a set of governing equations which can be put into matrix form. These matrices are then multiplied together to describe how to transfer the state variables from component to component. The solution is then closed by the boundary conditions on either end of the system. In this way, a network of smaller elements is built together to form a more complex system. For examples, see [27, 28].

CI phenomena are often non-linear. To characterize the stability of non-linear systems, linear analyses are not sufficient. For instance, the linear acoustics often predict a positive growth rate which suggests the system is unstable. However, due to non-linear damping mechanisms the system might reach an equilibrium point in which the driving and damping are equal. In this case the system reaches a limit cycle. A common example of this is a Helmholtz resonator. Helmholtz resonators serve to passively dampen acoustic oscillations in a duct. They consist of a large volume connected to the duct via a small neck. The resonator acts like a spring-mass system. The large volume of air acts like the spring and the stiffness of the air inside the neck is the mass. The acoustic oscillations in the duct force the mass of air in the neck to vibrate. If the frequency of the forcing is close to the resonant frequency of the resonator, acoustic energy is dissipated in the

resonator volume. For more information on Helmholtz resonators, see refs [29, 30, 27, 31]. Considering non-linear effects greatly complicates the governing equations and is therefore mostly approached with numerical techniques. Non-linear effects can be "tacked-on" to linear analyses by inserting the non-linearity in the heat release or boundary conditions [32, 33]. Non-linear acoustic effects are not considered in this thesis.

CIs themselves are often referred to by the frequency at which they occur. Low frequency combustion instabilities, commonly referred to as "rumble" are typically in the range of 50-150 Hz. Higher frequency instabilities are often called "screech." Low order models have been used to analyze low frequency instabilities [34]. A common distinction between flames is whether they are acoustically compact. An acoustically compact flame is one in which the flame length or nozzle dimension is small when compared to the acoustic wavelength. In these cases, the spatial distribution of the heat release is not important. This greatly simplifies the flame modelling as it can be modeled as a time dependent function, with the spatial dependence integrated out.

2.3 - The Acoustic Wave Equation

Acoustic disturbances can be treated as a perturbation about the ambient properties, i.e. a Reynolds decomposition of the pressure, density, and particle velocity:

$$\begin{aligned} p &= p_0 + p' \\ \rho &= \rho_0 + \rho' \\ v &= v_0 + v' \end{aligned} \tag{2.2.1}$$

The wave propagation is assumed to be isentropic, lossless, and to have small amplitudes. This third approximation is referred to as the small signal approximation. The linearized continuity equation is:

$$\rho_0 \frac{\partial v_z'}{\partial z} + \frac{\partial \rho'}{\partial t} = 0 \tag{2.2.2}$$

where z is the spatial coordinate, and t is time. Next, the linearized momentum equation is:

$$\rho_0 \frac{\partial v_z'}{\partial t} + \frac{\partial p'}{\partial z} = 0 \tag{2.2.3}$$

u can be eliminated from equations (2.2.2) and (2.2.3) by combining the two.

$$\frac{\partial^2 \rho'}{\partial t^2} - \frac{\partial^2 p'}{\partial z^2} = 0 \tag{2.2.4}$$

To relate the pressure and density, an equation of state is used. The wave propagation has been assumed to be isentropic, thus:

$$a_0^2 = \left(\frac{\partial p'}{\partial \rho'} \right)_s \tag{2.2.5}$$

The subscript s denotes an isentropic process (constant entropy). From equation (2.2.5) the following relations can be implied.

$$\rho' = \frac{1}{a_0^2} p', \quad \frac{\partial \rho'}{\partial t} = \frac{1}{a_0^2} \frac{\partial p'}{\partial t}, \quad \frac{\partial \rho'}{\partial z} = \frac{1}{a_0^2} \frac{\partial p'}{\partial z} \tag{2.2.6}$$

Removing ρ from equation (2.2.4) yields the one-dimensional lossless small signal wave equation:

$$\left(\frac{\partial^2}{\partial t^2} - a_0^2 \frac{\partial^2}{\partial z^2} \right) p' = 0 \tag{2.2.7}$$

Before moving on to more advanced versions of the wave equation, first consider how equation (2.2.7) might be solved. The most common starting place is separation of variables. Assume a separable solution of the form:

$$p' = Z(z)T(t) \tag{2.2.8}$$

Equation (2.2.8) is inserted into equation (2.2.7) to obtain:

$$\frac{T''}{T} - a_0^2 \frac{Z''}{Z} = 0 \tag{2.2.9}$$

Equation (2.2.9) holds for all values of t and z if both terms are constant, i.e.:

$$\begin{aligned} \frac{T''}{T} &= -\omega^2 \\ \frac{Z''}{Z} &= -k_z^2 \end{aligned} \tag{2.2.10}$$

The wave equation has been reduced to two ordinary differential equations:

$$\begin{aligned} T'' + a_0^2 k_z^2 T &= 0 \\ Z'' - \frac{\omega^2}{a_0^2} Z &= 0 \end{aligned} \tag{2.2.11}$$

Possible solutions for these two equations are:

$$\begin{aligned} T &= e^{-i\omega t} \\ Z &= Ae^{+ik_z z} + Be^{-ik_z z} \end{aligned} \tag{2.2.12}$$

The solution for T is a time-harmonic solution. The solution for Z is a plane-wave solution. Each term represents a plane of constant phase travelling in the $+z$ and $-z$ directions, respectively. Plane wave solutions are important as they are usually early attempts at a solution, and, as

mentioned earlier, they represent solutions in which the transverse waves have low frequencies. Finally, the wave number k_z can be related to the angular frequency ω via equation (2.2.9):

$$k^2 = k_z^2 \tag{2.2.13}$$

where $k = \frac{\omega}{a_0}$.

The move to three-dimensional space is straightforward. The continuity and momentum equations become:

$$\begin{aligned} \rho_0 \vec{\nabla} \cdot \vec{v}' + \frac{\partial \rho'}{\partial t} &= 0 \\ \rho_0 \frac{\partial \vec{v}'}{\partial t} + \vec{\nabla} p' &= 0 \end{aligned} \tag{2.2.14}$$

Combining these two equations leads to the three-dimensional lossless small signal wave equation:

$$\left(\frac{\partial^2}{\partial t^2} - a_0^2 \Delta \right) p' = 0 \tag{2.2.15}$$

Equation (2.2.15), like equation (2.2.7), can be solved with separation of variables. After separating, one possible solution is:

$$p'(x,y,z,t) = \left(C_1 e^{+ik_x x} + C_2 e^{-ik_x x} \right) \left(C_3 e^{+ik_y y} + C_4 e^{-ik_y y} \right) \left(C_5 e^{+ik_z z} + C_6 e^{-ik_z z} \right) e^{-i\omega t} \tag{2.2.16}$$

with

$$k^2 = k_x^2 + k_y^2 + k_z^2 \tag{2.2.17}$$

Equation (2.2.17) is often referred to as the dispersion relation. If the time dependence is assumed to be harmonic, as it is in equation (2.2.16), equation (2.2.15) can be re-written as:

$$\left(\Delta + k^2\right) f = 0 \tag{2.2.18}$$

Equation (2.2.18) is the Helmholtz equation. The unsteady pressure p' has been replaced with the general function f, as the Helmholtz equation governs both the unsteady pressure and velocity.

Convection can be incorporated into the wave equation by again modifying the continuity and momentum equations:

$$\begin{aligned} \rho_0 \vec{\nabla} \cdot \vec{v}' + \frac{D\rho'}{Dt} &= 0 \\ \rho_0 \frac{D\vec{v}'}{Dt} + \vec{\nabla} p' &= 0 \end{aligned} \tag{2.2.19}$$

D / Dt is the material derivative.

$$\frac{D}{Dt} = \frac{\partial}{\partial t} + \vec{v}_0 \cdot \vec{\nabla} \tag{2.2.20}$$

With $\vec{v}_0 = \left(v_x, v_y, v_z\right)$. Combining the equations (2.2.19) together yields the three-dimensional convected lossless small signal wave equation:

$$\left(\frac{D^2}{Dt^2} - a_0^2 \Delta \right) p' = 0 \tag{2.2.21}$$

Using separation of variables, the solution is of the form:

$$p' = X(x)\, Y(y)\, Z(z)\, T(t) \tag{2.2.22}$$

Before inserting equation (2.2.22) into equation (2.2.21), the latter is expanded to:

$$\frac{\partial^2 p'}{\partial t^2}+\left(v_x^2-a_0^2\right)\frac{\partial^2 p'}{\partial x^2}+\left(v_y^2-a_0^2\right)\frac{\partial^2 p'}{\partial y^2}+\left(v_z^2-a_0^2\right)\frac{\partial^2 p'}{\partial z^2}$$
$$+2v_x\frac{\partial^2 p'}{\partial x\partial t}+2v_y\frac{\partial^2 p'}{\partial y\partial t}+2v_z\frac{\partial^2 p'}{\partial z\partial t}+2v_xv_y\frac{\partial^2 p'}{\partial x\partial y}+2v_xv_z\frac{\partial^2 p'}{\partial x\partial z}+2v_yv_z\frac{\partial^2 p'}{\partial y\partial z}=0 \tag{2.2.23}$$

Plugging equation (2.2.22) into (2.2.23) and simplifying yields:

$$\frac{T''}{T}+\left(v_x^2-a_0^2\right)\frac{X''}{X}+\left(v_y^2-a_0^2\right)\frac{Y''}{Y}+\left(v_z^2-a_0^2\right)\frac{Z''}{Z}$$
$$+2\left(v_x\frac{X'T'}{XT}+v_y\frac{Y'T'}{YT}+v_z\frac{Z'T'}{ZT}+v_xv_y\frac{X'Y'}{XY}+v_xv_z\frac{X'Z'}{XZ}+v_yv_z\frac{Y'Z'}{YZ}\right)=0 \tag{2.2.24}$$

Equation (2.2.24) features a number of mixed terms, making it impossible to solve with traditional separation of variables. However, separable solutions still exist. For instance, if the components of p', that is X, Y, Z, and T, are such that they are equal to a constant times their derivative, then every term in equation (2.2.24) is indeed constant. Therefore, if they are all functions of the form Ce^{kx} then then the solution is separable. This disallows the solutions from being a linear combination of exponentials, such as a typical solution of the form:

$$X=C_1e^{+ik_xx}+C_2e^{-ik_xx} \tag{2.2.25}$$

Therefore the solution to equation (2.2.24) consists of waves only travelling in one direction in their respective dimensions. For the time solution, this works just fine, as time harmonic solutions is the typical form of T. However, this is not a suitable solution for full three-dimensional spatial solutions in ducts. If there is only in-line mean flow equation (2.2.24) becomes:

$$\frac{T''}{T}-a_0^2\left(\frac{X''}{X}+\frac{Y''}{Y}\right)+\left(v_z^2-a_0^2\right)\frac{Z''}{Z}+2v_z\frac{Z'T'}{ZT}=0 \tag{2.2.26}$$

With assumption of a harmonic time dependence, equation (2.2.26) separates readily, with the caveat that the solution must be a traveling wave in either the $+z$ or $-z$ direction. A standing wave solution is not a solution to equation (2.2.26) unless there is no mean flow at all.

Despite the complexity equation (2.2.21), consider the effects of a viscous medium. The continuity and momentum equations are:

$$\begin{aligned} \frac{D\rho}{Dt} + \rho\vec{\nabla}\cdot\vec{v} &= 0 \\ \rho\frac{D\vec{v}}{Dt} &= \vec{\nabla}\cdot\underline{\sigma} \end{aligned} \tag{2.2.27}$$

where $\underline{\sigma}$ is the Cauchy stress tensor. It can be decomposed into two parts:

$$\underline{\sigma} = -p\underline{I} + \underline{\tau} \tag{2.2.28}$$

where $\underline{I}$ is the 3x3 identity matrix and $\underline{\tau}$ is the traceless part of the Cauchy stress tensor, also called the deviatoric stress tensor. Note that all variables have dropped the prime notation, but they are still unsteady quantities. Thus equation (2.2.27) becomes:

$$\begin{aligned} \frac{D\rho}{Dt} + \rho\vec{\nabla}\cdot\vec{v} &= 0 \\ \rho\frac{D\vec{v}}{Dt} + \vec{\nabla}p &= \vec{\nabla}\cdot\underline{\tau} \end{aligned} \tag{2.2.29}$$

Equations (2.2.29) are a form of the Navier-Stokes equations (NSE) without body forces included. These equations are widely studied in a variety of forms. They are deemed so important their solution is one of the seven Millennium Prizes offered by the Clay Mathematics Institute [35]. Approaching the NSE from an acoustics point of view was first performed by Lighthill in 1952 [36]. He took equations (2.2.29) and rearranged them to the form:

$$\frac{\partial^2 \rho}{\partial t^2} - a_0^2 \Delta \rho = \frac{\partial^2 T_{ij}}{\partial x_i \partial x_j} \tag{2.2.30}$$

with

$$T_{ij} = \rho v_i v_j - \tau_{ij} + \left(p - a_0^2 \rho \right) \delta_{ij} \tag{2.2.31}$$

where δ_{ij} is the Kronecker delta. Equation (2.2.30) is Lighthill's equation and (2.2.31) is the Lighthill tensor, both presented using Einstein notation. Together they are known as Lighthill's acoustic analogy. They are referred to as an analogy because the equations are not reached from first principles. Rather, they are reached by manipulating the NSE into an inhomogeneous wave equation. The inhomogeneous terms are then analyzed as acoustic sources of excitation.

2.4 - Acoustic Boundary Conditions

Many acoustic systems feature liners. In traditional acoustic ducts, liners take the form of porous materials that serve to absorb and attenuate acoustic energy in the duct. In combustors, liners serve to contain the combustion process and manipulate airflow into and out of the combustor. These liners are typically made from alloys with advanced coatings in order to withstand high temperatures. Liners represent surfaces for acoustic waves to interact with, and they are typically handled mathematically with impedances.

Once a solution to a wave equation is reached, boundary conditions are used to calculate the remaining constants. For combustion, these boundary surfaces are typically the combustor walls, liners, or inlet and outlet planes. A variety of boundary conditions can be used to describe acoustic interactions with these surfaces, but the most common acoustic boundary conditions are rigid, pressure release, and impedance boundary conditions.

A rigid wall boundary condition is where the boundary is assumed to be perfectly rigid acoustically. That is, the boundary does not deform with any amount of incoming acoustic energy. This is encapsulated simply with:

$$\hat{n}_s \cdot \vec{v}\,|_s = 0 \tag{2.3.1}$$

In this way the velocity components going into the surface are, by definition, 0. The normal unit vector can be defined to point either into or out of the surface. In this thesis, the default direction of unit normal is out of the control volume.

The next most basic assumption is the pressure release boundary condition. This boundary condition marks the interface between the region of wave propagation and an exterior environment. The exterior environment is quiescent, i.e. there is no acoustic disturbance, hence:

$$p'\,|_s = 0 \tag{2.3.2}$$

Finally, there are impedance boundary conditions. According to Blackstock, "[impedance] is often described as the ratio of a 'push' variable … to a corresponding 'flow' variable". For acoustics, the push variable is the acoustic pressure and the 'flow' variable is the particle velocity. For a surface, the average pressure over the surface is taken. For the particle velocity through the surface, again the average is taken. The component of the average velocity pointing into the surface is taken. Thus:

$$Z \equiv \frac{p_{avg}{}'}{-\hat{n}_s \cdot \vec{v}_{avg}{}'} \tag{2.3.3}$$

As noted previously, the decision to take the component *into* the surface is arbitrary and can just as easily be taken *out* of the surface. From equation (2.3.3) it can be readily seen that $Z = \pm\infty$

corresponds to a rigid boundary condition and $Z = 0$ corresponds to a pressure release boundary condition.

In the same way electrical impedance depends on the frequency of the voltage source, acoustic impedance depends on the frequency of the acoustic disturbance. Impedance also varies with the flow moving through the duct and the surface itself. The dependence of the impedance on the frequency and flow variables can be modeled or interpolated from experimental data. Complicated forms of the impedance are excluded from this thesis for the sake of brevity. Myers developed the following boundary condition from the reasoning that no void can occur at the interface of the fluid and the boundary.

$$\vec{v}' \cdot \hat{n} = -\left(\frac{p'}{Z}\right) - \left(\frac{1}{i\omega}\right)\vec{v}_0 \cdot \vec{\nabla}\left(\frac{p'}{Z}\right) + \left(\frac{p'}{i\omega Z}\right)\hat{n} \cdot \left(\hat{n} \cdot \vec{\nabla} \otimes \vec{v}_0\right) \tag{2.3.4}$$

Here $\otimes$ is the outer product. Myers assumed a harmonic time dependence of $\exp(i\omega t)$. Assuming that Z is constant with respect to time and space across the given boundary and multiplying through by $i\omega$, it is possible to re-introduce time derivatives to obtain:

$$Z = \left(\frac{Dp'}{Dt} - p'\hat{n} \cdot \left(\hat{n} \cdot \vec{\nabla} \otimes \vec{v}_0\right)\right) \Big/ \left(-\frac{\partial \vec{v}'}{\partial t} \cdot \hat{n}\right) \tag{2.3.5}$$

In rectangular geometries, it is standard to define the coordinates of the duct aligning with the duct itself. This leads to the unit vectors $\hat{n}$ aligning with the principle unit vectors $\hat{n}_x$, $\hat{n}_y$, and $\hat{n}_z$. Therefore, there are three options in this geometry:

$$
\begin{aligned}
Z_{\hat{n}_x} &= \left(\frac{Dp'}{Dt} - p' \frac{\partial v_x}{\partial x} \right) \Bigg/ \left(-\frac{\partial \vec{v}'}{\partial t} \cdot \hat{n} \right) \\
Z_{\hat{n}_y} &= \left(\frac{Dp'}{Dt} - p' \frac{\partial v_y}{\partial y} \right) \Bigg/ \left(-\frac{\partial \vec{v}'}{\partial t} \cdot \hat{n} \right) \\
Z_{\hat{n}_z} &= \left(\frac{Dp'}{Dt} - p' \frac{\partial v_z}{\partial z} \right) \Bigg/ \left(-\frac{\partial \vec{v}'}{\partial t} \cdot \hat{n} \right)
\end{aligned}
\tag{2.3.6}
$$

If the outer product of the del operator and the time-independent mean-flow $\vec{v}_0$ is 0 then equation (2.3.5) becomes, regardless of the chosen geometry:

$$
Z = \frac{Dp' / Dt}{-\partial \vec{v}' / \partial t \cdot \hat{n}} \tag{2.3.7}
$$

Equation (2.3.7) is the acoustic boundary condition used in this thesis.

The previous boundary conditions have been wall boundary conditions. However not all boundaries are walls. Inlets and outlets of combustors are both boundaries and have associated boundary conditions. There are many options. However, this work will focus on two: The constant mass-flow rate and nozzle boundary conditions.

The constant mass-flow rate boundary condition is straightforward. The mass-flow rate at a given cross section is assumed to be constant. The mass flow rate is given by $\dot{m} = \rho v A$. Performing a Reynolds decomposition and neglecting purely steady and non-linear terms yields

$$
\rho_0 v_z' + v_{z,0} \frac{p'}{a_0^2} = 0 \tag{2.3.8}
$$

Equation (2.3.8) is the constant mass flow rate boundary condition.

The choked compact nozzle boundary condition is given by Marble and Candle [37]:

$$\frac{p'/p_0}{v'/a_0} = \frac{2\gamma}{M(\gamma-1)} \tag{2.3.9}$$

The properties in equation (2.3.9) are evaluated at the entrance plane of the nozzle. Equation (2.3.9) was derived assuming that the nozzle is choked. Equation (2.3.9) can also be written as

$$\frac{Z}{\rho_0 a_0} = \frac{2\gamma}{M(\gamma-1)} \tag{2.3.10}$$

In this case it is seen that the nozzle boundary condition equivalent to imposing a resistive impedance condition at the exit plane of the combustor.

2.5 - Solution Methods

Beyond separation of variables, there are few analytical approaches to solve complicated wave equations. Two common methods for solving the inhomogeneous wave equation are the Green's function method and the Galerkin expansion.

Starting with Green's function method, it is used to solve not just the inhomogeneous wave equation, but any inhomogeneous boundary value problem. Green's function method works by considering the differential equation in question in terms of a linear differential operator. A Green's function is obtained from the differential operator. The solution to the differential equation is then solved as an integral of the Green's function. Thus, the approach centers around posing the boundary value problem carefully and determining the appropriate Green's function. While this method results in an analytical solution, it is in the form of integrals, which usually must be computed numerically. Furthermore, it is difficult to extract the harmonic frequencies of the duct with a Green's function method. For more details, see [38]. Lastly, Green's function method does not work with inhomogeneous boundary conditions, such as the Myers-Ingard boundary condition.

Another prominent method is to use a Galerkin series. Assume the form of the acoustic pressure is:

$$p'(x,t) = \sum_{m=1}^{\infty} \eta_m(t)\psi_m(x) \tag{2.4.1}$$

Note that only one dimension is considered for brevity. The functions $\psi_m(x)$ are the eigen-solutions of the homogeneous wave equation that satisfy the same boundary conditions as the pressure with eigenfrequencies ω_m. $\eta_m(t)$ are the unknown time-dependent coefficients. One would then plug the pressure perturbation, equation (2.4.1), into an equation like (2.2.7), but with inhomogeneous terms. In this way the equation can be integrated over *x*. The remaining equation for the coefficients is complicated and usually not tractable if the inhomogeneous terms depend on the local flow. Various approximations can be made to make the analysis tractable, and with said approximations the eigenfrequencies can be solved for. If these approximations are not made, then numerical approaches are used. For more details, see [30].

The approach presented in this thesis is a control volume analysis (CVA). The first step is to define a control volume which encapsulates the region of wave propagation, most likely the combustion chamber. The control volume will be infinitesimally thin in the direction of wave propagation of interest. One then applies the integral forms of the conservation of mass and conservation of momentum equations to the control volume. A Reynolds decomposition on the acoustic variables is then performed. The wave propagation is assumed to be planar, which makes the analysis tractable. Equivalently, the low-frequency approximation is applied in the transverse directions. The resulting conservation equations are then combined into an inhomogeneous wave equation, henceforth referred to as the CVA equation. The inhomogeneous part of the CVA

equation depends on the transverse wall impedances and bulk transverse mean-flows in the control volume. The CVA equation is then used in conjunction with the planar wave solution to calculate the wave number. This wave number depends directly on the eigenfrequency of the system and the transverse mean-flow and impedances.

This solution can then easily be applied to systems to obtain the eigenfrequencies of the system and the planar mode shapes in the direction of propagation. This is one of the main advantages of using this method, as it incorporates the transverse wall impedances and mean-flows. More complicated systems, such as those with featuring inhomogeneous temperature distributions or non-uniform cross section, are approached via the network model. This flexibility allows this method to be applied to a wide variety of systems without having to re-derive the governing equations. Unfortunately, most systems result in a transcendental equation for the eigenfrequency, leading to a numerical solution. It is worthwhile to note that these are not numerical solutions to partial differential equations, but rather an analytical solution which does not permit a closed form solution. Even in such cases, the wavenumber of the wave propagation in the direction of interest is analytical. Furthermore, with the network model, any mode shapes obtained are also analytical.

Chapter 3

Control Volume Analysis

Consider a rectangular combustor with dimensions D_x, D_y, D_z. Consider the following control volume.

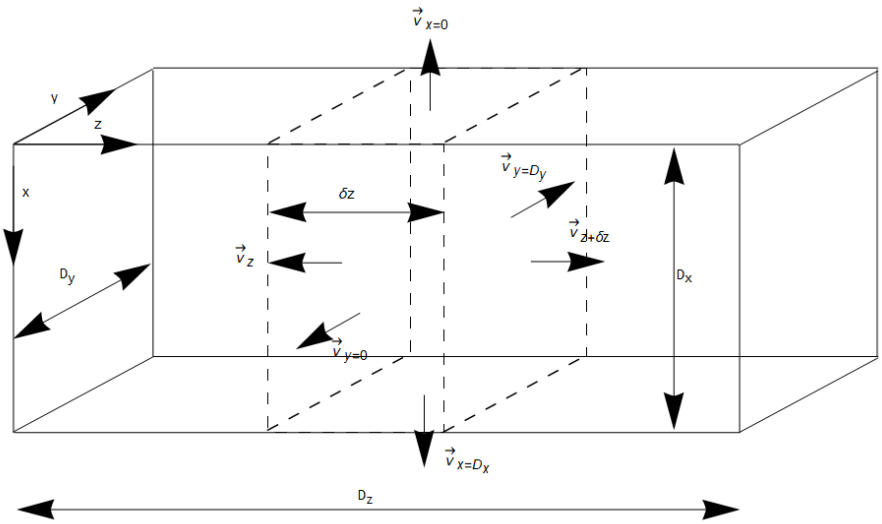

Figure 3.1: Control Volume

All velocities are pointing outward since the positive unit normal for each control surface point out of the control volume. Thus, each velocity is drawn such that it takes on a positive value from the perspective of each control surface. This thesis considers the primary direction of wave propagation to be in the z direction, the axial direction. There is mean flow into/out of the control volume through each control surface. The length δz is an infinitesimal length. The basic procedure of the analysis is as follows. Begin with the integral continuity equation. A Reynold's decomposition is then taken over the acoustic variables p, ρ, and v. Then the isentropic equation

of state and the Myers-Ingard boundary condition are used to "bake-in" the transverse mean flows and boundary conditions into the continuity equation itself. Next the same procedure is carried out over the integral momentum equation. The momentum equation is a vector equation, and thus the axial component is taken, as the wave propagation is planar. The two resulting equations are combined into a full wave-like equation which has the transverse mean-flow and impedance imbedded within it. The axial wavenumber, k_z, is then calculated analytically, along with the acoustic velocity.

3.1 - Conservation of Mass

One begins with the continuity equation in the integral form:

$$\frac{\partial}{\partial t}\left(\int_{CV}\rho dV\right)+\int_{CS}\rho(\vec{v}\cdot\hat{n})dS=0 \tag{3.1.1}$$

First the integrals are carried out over the control volume. The density and velocity over each control surface are assumed to be constant. This just leaves the density to integrate over. However, with an additional assumption that will be made later, these integrals become trivial. One can take the low-frequency approximation in the x and y directions. This allows the integrals to be carried out trivially. At this stage the continuity equation is

$$\begin{aligned}&\frac{\partial\rho}{\partial t}+\frac{(\rho v)_{z+\delta z}-(\rho v)_z}{\delta z}\\&\quad+\frac{1}{D_x}\left(\left(\rho(\vec{v}\cdot\hat{n})\right)_{x=D_x}+\left(\rho(\vec{v}\cdot\hat{n})\right)_{x=0}\right)+\frac{1}{D_y}\left(\left(\rho(\vec{v}\cdot\hat{n})\right)_{y=D_y}+\left(\rho(\vec{v}\cdot\hat{n})\right)_{y=0}\right)=0\end{aligned} \tag{3.1.2}$$

The second term is the limit definition of the derivative of the quantity ρv with respect to z. A Reynolds decomposition of velocity and density is performed. After simplification equation (3.1.2) becomes:

$$\frac{\partial \rho_0}{\partial t}+\frac{\partial \rho'}{\partial t}+\frac{\partial}{\partial z}\left(\rho_0 v_{z,0}+\rho_0 v_z{}'+\rho' v_{z,0}\rho' v_z{}'\right)$$
$$+\frac{1}{D_x}\left(\left(\rho_0\vec{v}_0+\rho_0\vec{v}'+\rho'\vec{v}_0+\rho'\vec{v}'\right)_{x=D_x}\cdot\hat{n}_{x=D_x}+\left(\rho_0\vec{v}_0+\rho_0\vec{v}'+\rho'\vec{v}_0+\rho'\vec{v}'\right)_{x=0}\cdot\hat{n}_{x=0}\right)$$
$$+\frac{1}{D_y}\left(\left(\rho_0\vec{v}_0+\rho_0\vec{v}'+\rho'\vec{v}_0+\rho'\vec{v}'\right)_{y=D_y}\cdot\hat{n}_{y=D_y}+\left(\rho_0\vec{v}_0+\rho_0\vec{v}'+\rho'\vec{v}_0+\rho'\vec{v}'\right)_{y=0}\cdot\hat{n}_{y=0}\right)=0$$

(3.1.3)

Note that the Reynolds decomposition introduces a steady and unsteady equation. As acoustic waves are unsteady pressure oscillations, the resulting unsteady equation is taken. Furthermore, products of unsteady terms are neglected, as this analysis is linear, and those terms are nonlinear.

$$\frac{\partial \rho'}{\partial t}+\frac{\partial}{\partial z}\left(\rho_0 v_z{}'+\rho' v_{z,0}\right)$$
$$+\frac{1}{D_x}\left(\left[\rho_0\vec{v}'+\rho'\vec{v}_0\right]_{x=D_x}\cdot\hat{n}_{x=D_x}+\left[\rho_0\vec{v}'+\rho'\vec{v}_0\right]_{x=0}\cdot\hat{n}_{x=0}\right) \qquad (3.1.4)$$
$$+\frac{1}{D_y}\left(\left[\rho_0\vec{v}'+\rho'\vec{v}_0\right]_{y=D_y}\cdot\hat{n}_{y=D_y}+\left[\rho_0\vec{v}'+\rho'\vec{v}_0\right]_{y=0}\cdot\hat{n}_{y=0}\right)=0$$

One can then utilize the isentropic equation of state and the boundary condition on the transverse walls to modify the third and fourth terms in equation (3.1.4). The isentropic equation of state is:

$$\rho'=\frac{p'}{a_0^2} \qquad (3.1.5)$$

As noted in section II, the boundary conditions on the transverse walls are not as straight forward as simply as an impedance condition due to the presence of flow in the *z* direction. Instead the Ingard-Myer boundary condition is used on these walls, equation (2.3.7). In order to take advantage of this boundary condition the following form of the unsteady pressure is assumed.

$$p'(z,t)=\left(Ae^{+ik_z^+ z}+Be^{-ik_z^- z}\right)e^{-i\omega t} \qquad (3.1.6)$$

Plugging equation (3.1.6) into equation (2.3.7)

$$Z_W = -\left(1 \mp v_{z,0}\frac{k_z^{\pm}}{\omega}\right)\frac{p'}{\hat{n}_W \cdot \vec{v}_W{}'} \tag{3.1.7}$$

Equations (3.1.5) and (3.1.7) are inserted into equation (3.1.4).

$$\begin{aligned}
&\frac{1}{a_0^2}\frac{\partial p'}{\partial t} + \frac{\partial}{\partial z}\left(\rho_0 v_z{}' + \frac{v_{z,0}}{a_0^2}p'\right) \\
&\quad + \frac{1}{D_x}\left(\left(\frac{\vec{v}_0 \cdot \hat{n}}{a_0^2}p' - \left(1 \mp v_{z,0}\frac{k_z^{\pm}}{\omega}\right)\frac{\rho_0}{Z}p'\right)_{x=D_x} + \left(\frac{\vec{v}_0 \cdot \hat{n}}{a_0^2}p' + \left(1 \mp v_{z,0}\frac{k_z^{\pm}}{\omega}\right)\frac{\rho_0}{Z}p'\right)_{x=0}\right) \\
&\quad + \frac{1}{D_y}\left(\left(\frac{\vec{v}_0 \cdot \hat{n}}{a_0^2}p' - \left(1 \mp v_{z,0}\frac{k_z^{\pm}}{\omega}\right)\frac{\rho_0}{Z}p'\right)_{y=D_y} + \left(\frac{\vec{v}_0 \cdot \hat{n}}{a_0^2}p' + \left(1 \mp v_{z,0}\frac{k_z^{\pm}}{\omega}\right)\frac{\rho_0}{Z}p'\right)_{y=0}\right) = 0
\end{aligned} \tag{3.1.8}$$

To continue p' is pulled out of the 3rd and 4th terms.

$$\begin{aligned}
&\frac{1}{a_0^2}\frac{\partial p'}{\partial t} + \frac{\partial}{\partial z}\left(\rho_0 v_z{}' + \frac{v_{z,0}}{a_0^2}p'\right) \\
&\quad + \left(\begin{array}{l}
\dfrac{1}{D_x}\left(\dfrac{1}{a_0^2}\left(v_{0,x=D_x} - v_{0,x=0}\right) - \left(1 \mp v_{z,0}\dfrac{k_z^{\pm}}{\omega}\right)\rho_0\left(\dfrac{1}{Z_{x=D_x}} + \dfrac{1}{Z_{x=0}}\right)\right) \\
+\dfrac{1}{D_y}\left(\dfrac{1}{a_0^2}\left(v_{0,y=D_y} - v_{0,y=0}\right) - \left(1 \mp v_{z,0}\dfrac{k_z^{\pm}}{\omega}\right)\rho_0\left(\dfrac{1}{Z_{y=D_y}} + \dfrac{1}{Z_{y=0}}\right)\right)
\end{array}\right)p' = 0
\end{aligned} \tag{3.1.9}$$

The unsteady pressure at opposite sides of the transverse walls of the control volume have been assumed to be approximately equal. To understand what this approximation means imagine the frequency of the acoustic wave becoming incredibly low. Graphically, this would stretch the pressure wave out like a slinky being stretched. Continuing with this analogy, as the slinky is

stretched further eventually it would become a straight wire. Thus, the low frequency approximation has been taken in the *x* and *y* directions. The following definition is made.

$$\begin{aligned}\xi^{\pm} \equiv & \frac{1}{D_x}\left(\frac{1}{a_0^2}\left((v_0\cdot\hat{n})_{x=0}+(v_0\cdot\hat{n})_{x=D_x}\right)-\left(1\mp v_{z,0}\frac{k_z^{\pm}}{\omega}\right)\rho_0\left(\frac{1}{Z_{x=D_x}}+\frac{1}{Z_{x=0}}\right)\right) \\ & +\frac{1}{D_y}\left(\frac{1}{a_0^2}\left((v_0\cdot\hat{n})_{y=0}+(v_0\cdot\hat{n})_{y=D_y}\right)-\left(1\mp v_{z,0}\frac{k_z^{\pm}}{\omega}\right)\rho_0\left(\frac{1}{Z_{y=D_y}}+\frac{1}{Z_{y=0}}\right)\right)\end{aligned} \tag{3.1.10}$$

Thus, the continuity equation is

$$\frac{1}{a_0^2}\frac{\partial p'}{\partial t}+\frac{\partial}{\partial z}\left(\rho_0 v_z{}'+\frac{v_{z,0}}{a_0^2}p'\right)+\xi^{\pm}p'=0 \tag{3.1.11}$$

Note that all the wall impedances and wall velocities are all contained in the term ξ. Furthermore the $\pm$ in the constant is introduced due to the presence of flow in the direction of propagation, i.e. $+z$. Also note the second term is the spatial derivative of the mass flow-rate, equation (2.3.8). Compare equation (3.1.11) to the traditional, one-dimensional, linear convected continuity equation below.

$$\frac{1}{a_0^2}\frac{\partial p'}{\partial t}+\frac{v_{z,0}}{a_0^2}\frac{\partial p'}{\partial z}+\rho_0\frac{\partial v_z{}'}{\partial z}=0 \tag{3.1.12}$$

From this comparison it is easy to see the additional term introduced. The extra term requires that both the transverse velocities and wall impedances be non-zero. Otherwise, equation (3.1.11) reduces to equation (3.1.12). This extra term is a forcing term, as it depends on the unsteady acoustic pressure, and not one of its derivatives.

3.2 - Conservation of Momentum

Consider the integral form of the momentum equation.

$$\frac{\partial}{\partial t}\left(\int_{CV}\rho\vec{v}dV\right)+\int_{CS}\rho\vec{v}\left(\vec{v}\cdot\vec{n}\right)dS=-\int_{CS}p\vec{n}dS+\sum F \tag{3.2.1}$$

The method proceeds the same as with the continuity equation. First, neglect body forces on the control volume and carry out the integrals over the control volume and control surfaces. Since only plane waves in z are considered the momentum equation is dotted with $\hat{z}$.

$$\begin{aligned}
&\frac{\partial}{\partial t}\left(\rho\left(\vec{v}\cdot\hat{z}\right)D_xD_y\delta z\right)\\
&\quad+\rho\left(\vec{v}_{z=z}\cdot\hat{z}\right)\left(\vec{v}_{z=z}\cdot\hat{n}_{z=z}\right)D_xD_y+\rho\left(\vec{v}_{z=z+\delta z}\cdot\hat{z}\right)\left(\vec{v}_{z=z+\delta z}\cdot\hat{n}_{z=z+\delta z}\right)D_xD_y\\
&\quad+\rho\left(\vec{v}_{x=0}\cdot\hat{z}\right)\left(\vec{v}_{x=0}\cdot\hat{n}_{x=0}\right)D_y\delta z+\rho\left(\vec{v}_{x=D_x}\cdot\hat{z}\right)\left(\vec{v}_{x=D_x}\cdot\hat{n}_{x=D_x}\right)D_y\delta z\\
&\quad+\rho\left(\vec{v}_{y=0}\cdot\hat{z}\right)\left(\vec{v}_{y=0}\cdot\hat{n}_{y=0}\right)D_x\delta z+\rho\left(\vec{v}_{y=D_y}\cdot\hat{z}\right)\left(\vec{v}_{y=D_y}\cdot\hat{n}_{y=D_y}\right)D_x\delta z\\
&\quad+p_{x=0}\left(\hat{n}_{x=0}\cdot\hat{z}\right)D_y\delta z+p_{x=D_x}\left(\hat{n}_{x=D_x}\cdot\hat{z}\right)D_y\delta z=0\\
&\quad+p_{y=0}\left(\hat{n}_{y=0}\cdot\hat{z}\right)D_x\delta z+p_{y=D_y}\left(\hat{n}_{y=D_y}\cdot\hat{z}\right)D_x\delta z=0\\
&\quad+p_{z=z}\left(\hat{n}_{z=z}\cdot\hat{z}\right)D_xD_y+p_{z=z+\delta z}\left(\hat{n}_{z=z+\delta z}\cdot\hat{z}\right)D_xD_y=0
\end{aligned} \tag{3.2.2}$$

Most of these dot products can be carried out trivially. In particular, the pressure components on x and y walls vanish due to taking the z component of the momentum equation. However, the velocities entering and exiting the sidewall have some component in the z-direction. That is, some amount of z momentum is carried into the control volume through the transverse walls. Therefore, those velocities dotted with $\hat{z}$ do not vanish. Instead, assume that the z component of the average of the z velocity at the location z and $z=z+\delta z$.

$$\vec{v}_{x=0}\cdot\hat{z}=\vec{v}_{x=D_x}\cdot\hat{z}=\vec{v}_{y=0}\cdot\hat{z}=\vec{v}_{y=D_y}\cdot\hat{z}=\frac{v_z+v_{z+\delta z}}{2} \tag{3.2.3}$$

While this seems dubious, remember that the control volume is a finite infinitesimal sliver, and any contribution to the z momentum from the transverse walls must be infinitesimal. Equation (3.2.2) reduces to

$$\begin{aligned}&\frac{\partial}{\partial t}\left(\rho v_z\right)\\&\quad+\frac{\left(\left(\rho v^2\right)_{z+\delta z}-\left(\rho v^2\right)_z\right)}{\delta z}\\&\quad+\left(\frac{v_z+v_{z+\delta z}}{2}\right)\left(\frac{\rho(\vec{v}\cdot\hat{n})_{x=D_x}+\rho(\vec{v}\cdot\hat{n})_{x=0}}{D_x}+\frac{\rho(\vec{v}\cdot\hat{n})_{y=D_y}+\rho(\vec{v}\cdot\hat{n})_{y=0}}{D_y}\right)\\&\quad+\frac{p_{z=z+\delta z}-p_{z=z}}{\delta z}=0\end{aligned}\tag{3.2.4}$$

The second and last terms in equation (3.2.4) are both limit definitions of derivatives and reduce to said derivatives. However, there is still a $z+\delta z$ term. Using Taylor's theorem

$$\begin{aligned}&v_{z+\delta z}=v_z+\frac{1}{1!}\frac{\partial v_z}{\partial z}\left(z+\delta z-z\right)+\frac{1}{2!}\frac{\partial^2 v_z}{\partial z^2}\left(z+\delta z-z\right)^2+\cdots\\&\rightarrow\\&\quad v_{z+\delta z}=v_z+\frac{\partial v_z}{\partial z}\delta z+\mathcal{O}\left(\delta z^2\right)\end{aligned}\tag{3.2.5}$$

Inserting equation (3.2.5) into equation (3.2.4) yields

$$\begin{aligned}&\frac{\partial}{\partial t}\left(\rho v_z\right)+\frac{\partial}{\partial z}\left(\rho v_z^2\right)\\&\quad+\left(v_z+\frac{1}{2}\frac{\partial v_z}{\partial z}\delta z\right)\left(\frac{\rho(\vec{v}\cdot\hat{n})_{x=D_x}-\rho(\vec{v}\cdot\hat{n})_{x=0}}{D_x}+\frac{\rho(\vec{v}\cdot\hat{n})_{y=D_y}-\rho(\vec{v}\cdot\hat{n})_{y=0}}{D_y}\right)+\frac{\partial p}{\partial z}=0\end{aligned}$$

(3.2.6)

As with continuity a Reynolds decomposition is applied to equation (3.2.6). After taking the unsteady equation, neglecting terms of $\mathcal{O}\left(\delta z^2\right)$, and some re-arranging

$$\frac{\partial}{\partial t}\left(\rho_0 v_z{}' + \rho' v_{z,0}\right) + \frac{\partial}{\partial z}\left(2\rho_0 v_{z,0} v_z{}' + \rho' v_{z,0}^2\right)$$
$$+\left(v_{z,0} + v_z{}'\right)\left(\begin{array}{l}\dfrac{(\rho_0\vec{v}_0 + \rho'\vec{v}_0 + \rho_0\vec{v}')_{x=D_x}\cdot\hat{n}_{x=D_x} + (\rho_0\vec{v}_0 + \rho'\vec{v}_0 + \rho_0\vec{v}')_{x=0}\cdot\hat{n}_{x=0}}{D_x} \\ + \dfrac{(\rho_0\vec{v}_0 + \rho'\vec{v}_0 + \rho_0\vec{v}')_{y=D_y}\cdot\hat{n}_{y=D_y} + (\rho_0\vec{v}_0 + \rho'\vec{v}_0 + \rho_0\vec{v}')_{y=0}\cdot\hat{n}_{y=0}}{D_y}\end{array}\right) \quad (3.2.7)$$
$$+\frac{\partial p'}{\partial z} = 0$$

After a bit more algebra and rearranging

$$\rho_0\frac{\partial v_z{}'}{\partial t} + \rho_0 v_{z,0}\frac{\partial v_z{}'}{\partial z} + v_z{}'\left(\frac{\rho_0(\vec{v}_0\cdot\hat{n})_{x=D_x} + \rho_0(\vec{v}_0\cdot\hat{n})_{x=0}}{D_x} + \frac{\rho_0(\vec{v}_0\cdot\hat{n})_{y=D_y} + \rho_0(\vec{v}_0\cdot\hat{n})_{y=0}}{D_y}\right) + \frac{\partial p'}{\partial z}$$
$$+ v_{z,0}\left[\begin{array}{l}\dfrac{\partial\rho'}{\partial t} + \rho_0\dfrac{\partial v_z{}'}{\partial z} + v_{z,0}\dfrac{\partial\rho'}{\partial z} + \dfrac{(\rho'\vec{v}_0 + \rho_0\vec{v}')_{x=D_x}\cdot\hat{n}_{x=D_x}(\rho'\vec{v}_0 + \rho_0\vec{v}')_{x=0}\cdot\hat{n}_{x=0}}{D_x} \\ \qquad + \dfrac{(\rho'\vec{v}_0 + \rho_0\vec{v}')_{y=D_y}\cdot\hat{n}_{y=D_y}(\rho'\vec{v}_0 + \rho_0\vec{v}')_{y=0}\cdot\hat{n}_{y=0}}{D_y}\end{array}\right] = 0$$

(3.2.8)

Upon closer inspection the term in brackets is actually equation (3.1.4) and therefore equal to zero. Therefore equation (3.2.8) becomes

$$\rho_0\frac{\partial v_z{}'}{\partial t} + \rho_0 v_{z,0}\frac{\partial v_z{}'}{\partial z} + \xi_0 v_z{}' + \frac{\partial p'}{\partial z} = 0 \quad (3.2.9)$$

with

$$\xi_0 \equiv \frac{\rho_0}{D_x}\left((\vec{v}_0\cdot\hat{n})_{x=0} + (\vec{v}_0\cdot\hat{n})_{x=D_x}\right) + \frac{\rho_0}{D_y}\left((\vec{v}_0\cdot\hat{n})_{y=0} + (\vec{v}_0\cdot\hat{n})_{y=D_y}\right) \quad (3.2.10)$$

Take a moment to compare equation (3.2.9) to the traditional, linear, one-dimensional convected momentum equation.

$$\rho_0 \frac{\partial v_z}{\partial t} + \rho_0 v_{z,0} \frac{\partial v_z}{\partial z} + \frac{\partial p}{\partial z} = 0 \tag{3.2.11}$$

As with the continuity equation, equation (3.1.11), an extra term has been introduced. This term depends on the transverse velocities entering (or exiting) the control volume. Just like the extra term in equation (3.1.11), this extra term is a forcing term, depending on the particle velocity itself, rather than one of its derivatives. It is interesting to note that the final version of this momentum equation does not "see" the impedance condition on the transverse walls at all.

3.3 - Combination

The next step is to combine equations (3.1.11) and (3.2.9) into a wave-like equation that can be used to look at wave propagation. First, take the partial derivative with respect to z of equation (3.2.9)

$$\rho_0 \frac{\partial^2 v_z'}{\partial z \partial t} + \rho_0 v_{z,0} \frac{\partial^2 v_z'}{\partial z^2} + \xi_0 \frac{\partial v_z'}{\partial z} + \frac{\partial^2 p'}{\partial z^2} = 0 \tag{3.3.1}$$

Next take the partial derivative with respect to t of equation (3.1.11).

$$\frac{1}{a_0^2} \frac{\partial^2 p'}{\partial t^2} + \frac{\partial^2}{\partial z \partial t} \left(\rho_0 v_z' + \frac{v_{z,0}}{a_0^2} p' \right) + \xi^{\pm} \frac{\partial p'}{\partial t} = 0 \tag{3.3.2}$$

Next equation (3.3.1) is subtracted from equation (3.3.2).

$$\frac{1}{a_0^2} \frac{\partial^2 p'}{\partial t^2} + \frac{v_{z,0}}{a_0^2} \frac{\partial^2 p'}{\partial z \partial t} + \xi^{\pm} \frac{\partial p'}{\partial t} - \rho_0 v_{z,0} \frac{\partial^2 v_z'}{\partial z^2} - \xi_0 \frac{\partial v_z'}{\partial z} - \frac{\partial^2 p'}{\partial z^2} = 0 \tag{3.3.3}$$

In order to change derivatives of particle velocity to unsteady acoustic pressures, one can make use of equation (3.1.11), rearranged to

$$\frac{\partial v_z{}'}{\partial z} = -\frac{1}{a_0^2 \rho_0}\frac{\partial p'}{\partial t} - \frac{v_{z,0}}{a_0^2 \rho_0}\frac{\partial p'}{\partial z} - \frac{\xi^{\pm}}{\rho_0} p' \tag{3.3.4}$$

and differentiated to

$$\frac{\partial^2 v_z{}'}{\partial z^2} = -\frac{1}{a_0^2 \rho_0}\frac{\partial^2 p'}{\partial z \partial t} - \frac{v_{z,0}}{a_0^2 \rho_0}\frac{\partial^2 p'}{\partial z^2} - \frac{\xi^{\pm}}{\rho_0}\frac{\partial p'}{\partial z} \tag{3.3.5}$$

Plugging equations (3.3.4) and (3.3.5) into equation (3.3.3) and simplifying yields

$$\frac{\partial^2 p'}{\partial t^2} + 2v_{z,0}\frac{\partial^2 p'}{\partial z \partial t} + \left(v_{z,0}^2 - a_0^2\right)\frac{\partial^2 p'}{\partial z^2} + \left(a_0^2 \xi^{\pm} + \frac{\xi_0}{\rho_0}\right)\left(\frac{\partial p'}{\partial t} + v_{z,0}\frac{\partial p'}{\partial z}\right) + \frac{a_0^2 \xi_0 \xi^{\pm}}{\rho_0} p' = 0 \tag{3.3.6}$$

As with the continuity and momentum equations it is a useful orienting measure to compare this equation to the traditional one-dimensional convected linear wave equation.

$$\frac{\partial^2 p'}{\partial t^2} + 2v_{z,0}\frac{\partial^2 p'}{\partial z \partial t} + \left(v_{z,0}^2 - a_0^2\right)\frac{\partial^2 p'}{\partial z^2} = 0 \tag{3.3.7}$$

As expected, convected terms are introduced. However, there are three additional terms. It is difficult to view equation (3.3.6) directly in terms of the added impedance and transverse velocities in this model. To accomplish this, consider two new constants:

$$\xi_v \equiv \frac{1}{D_x}\left((\vec{v}_0 \cdot \hat{n})_{x=0} + (\vec{v}_0 \cdot \hat{n})_{x=D_x}\right) + \frac{1}{D_y}\left((\vec{v}_0 \cdot \hat{n})_{y=0} + (\vec{v}_0 \cdot \hat{n})_{y=D_y}\right) \tag{3.3.8}$$

$$\xi_Z \equiv \frac{1}{D_x}\left(\frac{1}{Z_{x=D_x}} + \frac{1}{Z_{x=0}}\right) + \frac{1}{D_y}\left(\frac{1}{Z_{y=D_y}} + \frac{1}{Z_{y=0}}\right) \tag{3.3.9}$$

These constants are referred to as the mean-flow parameters and impedance parameters, respectively. In terms of these two new quantities, the previous ξ terms are:

$$\begin{aligned} \xi^{\pm} &= \frac{\xi_v}{a_0^2} - \left(1 \mp v_{z,0} \frac{k_z^{\pm}}{\omega}\right) \rho_0 \xi_Z \\ \xi_0 &= \rho_0 \xi_v \end{aligned} \tag{3.3.10}$$

Substitution of equation (3.3.10) into equation (3.3.6) and subsequent simplification yields:

$$\begin{aligned} &\frac{\partial^2 p'}{\partial t^2} + 2v_{z,0} \frac{\partial^2 p'}{\partial z \partial t} + \left(v_{z,0}^2 - a_0^2\right) \frac{\partial^2 p'}{\partial z^2} \\ &\quad + \left(2\xi_v - a_0^2 \rho_0 \xi_Z \left(1 \mp v_{z,0} \frac{k_z^{\pm}}{\omega}\right)\right)\left(\frac{\partial p'}{\partial t} + v_{z,0} \frac{\partial p'}{\partial z}\right) \\ &\quad + \xi_v \left(\xi_v - a_0^2 \rho_0 \xi_Z \left(1 \mp v_{z,0} \frac{k_z^{\pm}}{\omega}\right)\right) p' = 0 \end{aligned} \tag{3.3.11}$$

With the effects of wall impedances and transverse velocities separated out, a few notes: The forcing term requires non-zero transverse mean-flow in order to appear, while there is also an impedance dependence. Each impedance effect has two parts. First, they have part which is purely dependent on the impedances, and a second part which depends on the mean flow in the z direction. This is the Myers-Ingard boundary condition in action. If another boundary condition were used on the transverse walls, these terms would change accordingly. As a final notational change, one can change the velocities, angular frequency, and impedances to Mach numbers, the wave number, and normalized impedances respectively:

$$
\begin{aligned}
M_\beta &= \frac{v_\beta}{a_0} \\
k_0 &= \frac{\omega}{a_0} \\
\mathcal{Z}_\beta &= \frac{Z_\beta}{\rho_0 a_0}
\end{aligned}
\tag{3.3.12}
$$

Exchange ξ_v for ξ_M and ξ_Z for $\xi_{\mathcal{Z}}$:

$$
\begin{aligned}
\xi_M &\equiv \frac{\xi_v}{a_0} = \frac{1}{D_x}\left((M_0\hat{n}_v\cdot\hat{n}_W)_{x=0} + (M_0\hat{n}_v\cdot\hat{n}_W)_{x=D_x}\right) + \frac{1}{D_y}\left((M_0\hat{n}_v\cdot\hat{n}_W)_{y=0} + (M_0\hat{n}_v\cdot\hat{n}_W)_{y=D_y}\right) \\
\xi_{\mathcal{Z}} &\equiv \rho_0 a_0 \xi_Z = \frac{1}{D_x}\left(\frac{1}{\mathcal{Z}_{x=D_x}} + \frac{1}{\mathcal{Z}_{x=0}}\right) + \frac{1}{D_y}\left(\frac{1}{\mathcal{Z}_{y=D_y}} + \frac{1}{\mathcal{Z}_{y=0}}\right)
\end{aligned}
$$

(3.3.13)

In equation (3.3.13), $\hat{n}_v$ and $\hat{n}_W$ refer to the direction of mean-flow through the given control surface and the unit normal of the given control surface, respectively. Equation (3.3.11) becomes:

$$
\begin{aligned}
&\frac{1}{a_0^2}\frac{\partial^2 p'}{\partial t^2} + \left(M_{z,0}^2 - 1\right)\frac{\partial^2 p'}{\partial z^2} + 2\frac{M_{z,0}}{a_0}\frac{\partial^2 p'}{\partial z \partial t} \\
&\quad + \left(2\xi_M - \xi_{\mathcal{Z}}\left(1 \mp M_{z,0}\frac{k_z^\pm}{k_0}\right)\right)\left(\frac{1}{a_0}\frac{\partial p'}{\partial t} + M_{z,0}\frac{\partial p'}{\partial z}\right) \\
&\quad + \xi_M\left(\xi_M - \xi_{\mathcal{Z}}\left(1 \mp M_{z,0}\frac{k_z^\pm}{k_0}\right)\right)p' = 0
\end{aligned}
\tag{3.3.14}
$$

3.4 - Calculation of $\mathbf{k_z^\pm}$ and $\mathbf{v_z'}$

One can use equation (3.3.11)/(3.3.14) in combination with the assumed plane wave solution, equation (3.1.6), to calculate $k_z^\pm$ in terms of the angular frequency, mean flow velocities, and wall impedances. Simply plug equation (3.1.6) into equation (3.3.11)/(3.3.14). Note that one

must plug in one plane wave at a time. That is, set either A or B to 0. Both solutions are encapsulated in $k_z^{\pm}$.

$$\left(M_{z,0}^2\left(1+i\frac{\xi_{\mathcal{Z}}}{k_0}\right)-1\right)\left(k_z^{\pm}\right)^2 \mp M_{z,0}\left(2k_0+2i(\xi_M+\xi_{\mathcal{Z}})-\frac{\xi_M\xi_{\mathcal{Z}}}{k_0}\right)k_z^{\pm} + k_0\left(k_0+i(2\xi_M+\xi_{\mathcal{Z}})\right)-\xi_M\left(\xi_M+\xi_{\mathcal{Z}}\right)=0 \tag{3.4.1}$$

At this point quadratic equation is used to solve for $k_z^{\pm}$.

$$k_z^{\pm} = \frac{\pm M_{z,0}\left(k_0\left(1+i\frac{\xi_M+\xi_{\mathcal{Z}}}{k_0}\right)-\frac{\xi_M\xi_{\mathcal{Z}}}{2k_0}\right)-\sqrt{\left(\frac{M_{z,0}\xi_M\xi_{\mathcal{Z}}}{2k_0}\right)^2+k_0^2\left(1+i\frac{\xi_M}{k_0}\right)\left(1+i\frac{\xi_M+\xi_{\mathcal{Z}}}{k_0}\right)}}{M_{z,0}^2\left(1+i\frac{\xi_{\mathcal{Z}}}{k_0}\right)-1} \tag{3.4.2}$$

Note the $\pm$ is not from quadratic equation. Rather, it is associated with the forward and rearward travelling waves. The $\pm$ from quadratic equation is the – in front of the radical. It was chosen in order to match the axial wavenumber for a rigid duct with no transverse mean-flow. It is often necessary to look at the acoustic velocity as well. Based on the plane wave solution for the pressure, one expects the acoustic velocity to be planar as well. Thus:

$$v'(z,t)=\left(\mathrm{C}e^{+ik_z^+z}+\mathrm{D}e^{-ik_z^-z}\right)e^{-i\omega t} \tag{3.4.3}$$

In order to calculate C and D, typically one uses equation (3.2.11). Instead use the version of the momentum equation in this thesis, equation (3.2.9), is used. Substituting equations (3.4.3) and (3.1.6) into equation (3.2.9) yields:

$$\left(\left(i\xi_v+\left(\omega+i\rho_0a_0^2\xi_Z\right)\left(1-v_{z,0}\frac{k_z^+}{\omega}\right)\right)\mathrm{A}-\rho_0a_0^2k_z^+\mathrm{C}\right)e^{+ik_z^+z}$$
$$+\left(\left(i\xi_v+\left(\omega+i\rho_0a_0^2\xi_Z\right)\left(1+v_{z,0}\frac{k_z^-}{\omega}\right)\right)\mathrm{B}+\rho_0a_0^2k_z^-\mathrm{D}\right)e^{-ik_z^-z}=0 \tag{3.4.4}$$

Equation (3.4.4) represents two separate equations: one in which C is eliminated in terms of A, and one in which D is eliminated in terms of B. However, there is one small issue. In considering both the forward and reverse travelling waves, there is an extra $\pm$. This inconsistency is quickly removed by recognizing that each equation only addresses one direction of plane the plane wave. Therefore, the first equation takes on the signs of the forward travelling wave and the second equation takes on the signs of the rearward travelling wave. Solving the two equations for C and D yields:

$$\mathrm{C}=\frac{\mathrm{A}}{\rho_0a_0^2k_z^+}\left(i\xi_v+\left(\omega+i\rho_0a_0^2\xi_Z\right)\left(1-v_{z,0}\frac{k_z^+}{\omega}\right)\right)$$
$$\mathrm{D}=-\frac{\mathrm{B}}{\rho_0a_0^2k_z^-}\left(i\xi_v+\left(\omega+i\rho_0a_0^2\xi_Z\right)\left(1+v_{z,0}\frac{k_z^-}{k_0}\right)\right) \tag{3.4.5}$$

Plugging equations (3.4.5) into equation (3.4.3) yields:

$$v'\left(z,t\right)=\frac{1}{\rho_0a_0^2}\left(\mathrm{Y}^+\mathrm{A}e^{+ik_z^+z}-\mathrm{Y}^-\mathrm{B}e^{-ik_z^-z}\right)e^{-i\omega t}$$
$$\mathrm{Y}^\pm=\frac{1}{k_z^\pm}\left(i\xi_v+\left(\omega+i\rho_0a_0^2\xi_Z\right)\left(1\mp v_{z,0}\frac{k_z^\pm}{\omega}\right)\right) \tag{3.4.6}$$

Or in its normalized form:

$$
\begin{aligned}
v'(z,t) &= \frac{1}{\rho_0 a_0}\left(\Upsilon^{+}\mathrm{A}e^{+ik_z^{+}z} - \Upsilon^{-}\mathrm{B}e^{-ik_z^{-}z}\right)e^{-ia_0k_0t} \\
\Upsilon^{\pm} &= \frac{1}{k_z^{\pm}}\left(i\xi_M + \left(k_0 - i\xi_{\mathcal{Z}}\right)\left(1 \mp M_{z,0}\frac{k_z^{\pm}}{k_0}\right)\right)
\end{aligned}
\tag{3.4.7}
$$

Equations (3.1.6), (3.4.6)/(3.4.7), (3.3.11)/(3.3.14), and (3.4.2) are the primary equations resulting from this analysis.

Chapter 4

Initial Validation

Validation of the control volume analysis is primarily done by comparing this control volume solution to the wave equation of various forms. First compare equation (3.3.11) to the 1D wave equation:

$$\frac{\partial^2 p'}{\partial t^2} - a_0^2 \frac{\partial^2 p'}{\partial z^2} = 0 \tag{4.0.1}$$

This exact equation is recovered if all velocities are set to 0 and all impedances are set to ∞. Furthermore, it can be seen that one can also recover the convected 1D wave equation, equation (3.3.7), by setting all transverse velocities to 0 and transverse impedances to ∞ in equation (3.3.11) . While these comparisons give some confidence in the application the CVA, there is no analytical reference for the transverse impedances and mean-flows considered together. Nevertheless, there are analytical solutions to the wave equation with some of these effects. Furthermore, it useful to consider if the low frequency approximation has been correctly applied. In order to accomplish this, consider the full 3D solution presented by Munjal in *Acoustics of Ducts and Mufflers* [7], both with and without mean-flow in the direction of propagation. Note that Munjal's original work has been slightly modified to match this thesis' choice of time convention, definition of impedance, and dimensions of the duct.

4.1 - Rectangular Duct with Compliant Walls (Munjal)

Beginning without mean-flow consider the 3D wave equation:

$$\left(\frac{\partial^2}{\partial t^2} - a_0^2 \nabla^2\right) p = 0 \tag{4.1.1}$$

By utilizing separation of variables a possible solution of (4.1.1) is;

$$p(x,y,z,t) = \left(C_1 e^{+ik_z z} + C_2 e^{-ik_z z}\right)\left(C_3 e^{+ik_x x} + e^{-ik_x x}\right)\left(C_4 e^{+ik_y y} + e^{-ik_y y}\right) e^{-i\omega t} \tag{4.1.2}$$

Now the impedance conditions are applied at the walls. They are:

$$\begin{aligned} -\frac{p(0,y,z,t)}{\vec{v}_x(0,y,z,t)\cdot\hat{n}_{x=0}} &= -\frac{p(D_x,y,z,t)}{\vec{v}_x(D_x,y,z,t)\cdot\hat{n}_{x=D_x}} = Z_x \\ -\frac{p(x,0,z,t)}{\vec{v}_y(x,0,z,t)\cdot\hat{n}_{y=0}} &= -\frac{p(x,D_y,z,t)}{\vec{v}_y(x,D_y,z,t)\cdot\hat{n}_{y=D_y}} = Z_y \end{aligned} \tag{4.1.3}$$

The unit vectors point out of the control volume for their respective surfaces. In order to utilize equations (4.1.3) u_x and u_y must be obtained. This is done via the linear momentum equation in *x* and *y*. Note that the *x* and *y* equations will be analogous to one another, and therefore only *x* equations will be shown for the derivation. The linear momentum equation in *x* is:

$$\rho_0 \frac{\partial v_x}{\partial t} + \frac{\partial p}{\partial x} = 0 \tag{4.1.4}$$

Because time harmonic behavior is assumed equation (4.1.4) can be simplified to

$$v_x = -\frac{i}{\omega\rho_0}\frac{\partial p}{\partial x} \tag{4.1.5}$$

Equation (4.1.2) is inserted into equation (4.1.5) to obtain:

$$v_x = \frac{k_x}{\omega\rho_0}\left(C_1 e^{+ik_z z} + C_2 e^{-ik_z z}\right)\left(C_3 e^{+ik_x x} - e^{-ik_x x}\right)\left(C_4 e^{+ik_y y} + e^{-ik_y y}\right) e^{-i\omega t} \tag{4.1.6}$$

Then substitute equations (4.1.2) and (4.1.6) into the boundary conditions (4.1.3) to obtain

$$\begin{aligned} \frac{\omega\rho_0}{k_x}\frac{1+C_3}{1-C_3} &= Z_x \\ -\frac{\omega\rho_0}{k_x}\frac{e^{-ik_xD_x}+C_3e^{+ik_xD_x}}{e^{-ik_xD_x}-C_3e^{+ik_xD_x}} &= Z_x \end{aligned} \tag{4.1.7}$$

One can use equations (4.1.7) to eliminate C_3. Thus:

$$\sin(k_xD_x)\left(\frac{Z_xk_x}{\omega\rho_0}\right)^2 + 2i\cos\left(k_xD_x\right)\frac{Z_xk_x}{\omega\rho_0} + \sin(k_xD_x) = 0 \tag{4.1.8}$$

From here one can use quadratic equation to obtain the following transcendental equation:

$$\frac{Z_xk_x}{\omega\rho_0} = \frac{-\cos\left(k_xD_x\right)\pm 1}{i\sin\left(k_xD_x\right)} \tag{4.1.9}$$

with an analogous equation in *y*. Equation (4.1.9) can be broken into two separate equations. After some clever use of trigonometric half-angle formulae, the two equations are:

$$\begin{aligned} \frac{Z_xk_x}{\omega\rho_0} &= \frac{-\cos\left(k_xD_x\right)+1}{i\sin\left(k_xD_x\right)} = i\tan\left(\frac{k_xD_x}{2}\right) \\ \frac{Z_xk_x}{\omega\rho_0} &= \frac{-\cos\left(k_xD_x\right)-1}{i\sin\left(k_xD_x\right)} = -i\cot\left(\frac{k_xD_x}{2}\right) \end{aligned} \tag{4.1.10}$$

To make sense of these two equations set the wall impedances equal to 0:

$$\begin{aligned} \infty &= i\tan\left(\frac{k_xD_x}{2}\right) \\ \infty &= -i\cot\left(\frac{k_xD_x}{2}\right) \end{aligned} \tag{4.1.11}$$

While this doesn't seem so helpful at first glance, split up the cotangent and tangent into signs and cosines via their respective definitions. This means that their denominators, cosine and sine, respectively, go to 0. From this k_x will be:

$$\begin{aligned} k_x &= \frac{(2n+1)\pi}{D_x}, n \in \mathbb{Z} \\ k_x &= \frac{2m\pi}{D_x}, m \in \mathbb{Z} \end{aligned} \tag{4.1.12}$$

Thus, for infinitely rigid walls the second equation returns the symmetric modes and the first equation returns the anti-symmetric modes. Similarly, the roots to equations (4.1.10) alternate, with the latter equation (using (-)) yielding symmetric roots and the former equation (using (+)) yielding anti-symmetric roots.

One can use equations (4.1.10) in combination with the usual dispersion relation, $k_x^2 + k_y^2 + k_z^2 = k_0^2$, given by separation of variables to obtain k_z. However, it is possible to obtain an analytical solution to equations (4.1.10) in the low frequency limit. This will also compare directly to the k_z calculated from the CVA, equation (3.4.2). In order to take the low-frequency approximation it is known that, in general, wave numbers are related to the frequency via:

$$k_\beta = \frac{\omega_\beta}{a_{0,\beta}} \tag{4.1.13}$$

Thus, if the frequency is low, then the wave number is also low. Furthermore, it's divided by the speed of sound in the medium, further reducing its magnitude. Therefore it is a reasonable approximation to use the small angle approximation on trigonometric functions of equations (4.1.10). Thus:

$$\frac{Z_x k_x}{\omega\rho_0} = i\frac{k_x D_x}{2}$$
$$\frac{Z_x k_x}{\omega\rho_0} = -i\frac{2}{k_x D_x} \tag{4.1.14}$$

The next step is to solve for k_x. However, in solving the former equation in (4.1.14) k_x disappears. Therefore, no anti-symmetric modes are valid in the low frequency approximation. Indeed, by using the previous analogy of a slinky, it's straightforward to understand how any valid solution under this approximation is, by definition, symmetric. Solving for k_x one obtains:

$$k_x^2 = -2i\frac{\omega\rho_0}{D_x Z_x}$$
$$k_y^2 = -2i\frac{\omega\rho_0}{D_y Z_y} \tag{4.1.15}$$

The accompanying equation for k_y is given in equation (4.1.15). Utilizing the dispersion relation, one obtains:

$$\begin{aligned} k_z &= \sqrt{\frac{\omega^2}{a_0^2} + 2i\omega\rho_0\left(\frac{1}{D_x Z_x} + \frac{1}{D_y Z_y}\right)} \\ &= \sqrt{k_0^2 + ik_0\rho_0 a_0 \xi_{Mun}} \\ \xi_{Mun} &= 2\left(\frac{1}{D_x Z_x} + \frac{1}{D_y Z_y}\right) \end{aligned} \tag{4.1.16}$$

Now for the comparison. Plug the same conditions into equation (3.4.2) to obtain:

$$\begin{aligned} M_{z,0} &\to 0 \\ \xi_v &\to 0 \\ \xi_Z &\to 2\left(\frac{1}{D_x Z_x} + \frac{1}{D_y Z_y}\right) \\ k_z^{\pm} &\to \sqrt{k_0^2 + ik_0\rho_0 a_0 \xi_Z} \end{aligned} \tag{4.1.17}$$

Thus, the CVA yields the same solution as Munjal's in the plane wave limit under these circumstances.

4.2 - Rectangular Duct with Compliant Walls and Axial Mean-Flow (Munjal)

Munjal begins with the convected 3D wave equation:

$$\left(\frac{D^2}{Dt^2} - a_0^2\nabla^2\right)p = 0 \tag{4.2.1}$$

The convective derivative is given by:

$$\frac{D}{Dt} = \frac{\partial}{\partial t} + v_{z,0}\frac{\partial}{\partial z} \tag{4.2.2}$$

Typically the latter term of the convective derivative is $\vec{v}_0 \cdot \vec{\nabla}$, however Munjal chose $\vec{v}_0 = v_{z,0}\hat{z}$ for simplicity. A possible solution to equation (4.2.1) is very close to the previous solution that has been used, equation (4.1.2). However, there is a slight modification due to the presence of mean flow:

$$p(x,y,z,t) = \left(C_1 e^{+ik_z^+ z} + C_2 e^{-ik_z^- z}\right)\left(C_3 e^{+ik_x x} + e^{-ik_x x}\right)\left(C_4 e^{+ik_y y} + e^{-ik_y y}\right)e^{-i\omega t} \tag{4.2.3}$$

The mean flow changes the wave number in the z direction depending on the direction of propagation. Hence the distinction in wave numbers between the forward and rearward travelling waves. The dispersion relation between the various wave numbers, given by separation of variables, is:

$$k_x^2 + k_y^2 + \left(k_z^\pm\right)^2 = \left(k_0 \mp M_{z,0}k_z^\pm\right)^2 \tag{4.2.4}$$

Normally, impedance boundary conditions are used on the transverse walls. The presence of flow changes that. As a first approximation, one can account for flow with the Myers-Ingard boundary condition, equation (2.3.7). Thus, the boundary conditions are:

$$\begin{aligned} -\frac{Dp(0,y,z,t)/Dt}{\hat{n}_{x=0}\cdot\partial\vec{v}_x(0,y,z,t)/\partial t} &= -\frac{Dp(D_x,y,z,t)/Dt}{\hat{n}_{x=D_x}\cdot\partial\vec{v}_x(D_x,y,z,t)/\partial t} = Z_x \\ -\frac{Dp(x,0,z,t)/Dt}{\hat{n}_{y=0}\cdot\partial\vec{v}_y(x,0,z,t)/\partial t} &= -\frac{Dp(x,D_y,z,t)/Dt}{\hat{n}_{y=D_y}\cdot\partial\vec{v}_y(x,D_y,z,t)/\partial t} = Z_y \end{aligned} \tag{4.2.5}$$

As with the previous example one can obtain expressions for v_x and v_y via the momentum equation. Due to the presence of mean flow, the momentum equation is convected:

$$\rho_0\frac{D\vec{v}}{Dt}+\vec{\nabla}p=0 \tag{4.2.6}$$

For each component of $\vec{v}$ equation (4.2.6) is dotted with the desired direction unit vector and the resulting equation is then utilized to find each component. Thus, one assumes the following form of v_x:

$$v_x(x,y,z,t)=\left(C_5e^{+ik_z^+z}+C_6e^{-ik_z^-z}\right)\left(C_7e^{+ik_xx}+e^{-ik_xx}\right)\left(C_8e^{+ik_yy}+e^{-ik_yy}\right)e^{-i\omega t} \tag{4.2.7}$$

Plugging the assumed form of v_x into the *x* component of equation (4.2.6) one can equate the coefficients of each exponential separately to 0 in order to obtain C_{5-8} in terms of C_{1-4}. The resulting equation is:

$$\begin{aligned} v_x(x,y,z,t)=-\frac{1}{\rho_0a_0}\frac{k_x}{k_0}&\left(\frac{C_1}{1-M_{z,0}k_z^+/k_0}e^{+ik_z^+z}+\frac{C_2}{1+M_{z,0}k_z^-/k_0}e^{-ik_z^-z}\right) \\ &\times\left(-C_3e^{+ik_xx}+e^{-ik_xx}\right)\left(C_4e^{+ik_yy}+e^{-ik_yy}\right)e^{-i\omega t} \end{aligned} \tag{4.2.8}$$

with similar equations for v_y and v_z. Next the boundary conditions (4.2.5) are applied by plugging equations (4.2.3) and (4.2.8) into them. For the boundary condition at $x = 0$ one obtains:

$$-\rho_0 a_0 \frac{k_0}{k_x} \frac{\left(1 - M_{z,0} k_z^+ / k_0\right) C_1 e^{+ik_z^+ z} + \left(1 + M_{z,0} k_z^- / k_0\right) C_2 e^{-ik_z^- z}}{\left(1 - M_{z,0} k_z^+ / k_0\right)^{-1} C_1 e^{+ik_z^+ z} + \left(1 + M_{z,0} k_z^- / k_0\right)^{-1} C_2 e^{-ik_z^- z}} \frac{1 + C_3}{1 - C_3} = Z_x \tag{4.2.9}$$

However, this introduces a few problems. First, k_x and $k_z^\pm$ appear to be coupled together. This would suggest that in the presence of mean flow, k_x and k_y become $k_x^\pm$ and $k_y^\pm$, respectively. Furthermore, the very introduction of the wavenumbers comes from the dispersion relation, which itself comes from separation of variables. Because of their nature as separation constants, they must be constant with respect to *x*, *y*, *z*, and *t*. Thus equation (4.2.3) becomes:

$$\begin{aligned} p &= p^+ + p^- \\ &= C_1 e^{+ik_z^+ z} \left(C_3^+ e^{+ik_x^+ x} + e^{-ik_x^+ x}\right)\left(C_4^+ e^{+ik_y^+ y} + e^{-ik_y^+ y}\right) e^{-i\omega t} \\ &\quad + C_2 e^{-ik_z^- z} \left(C_3^- e^{+ik_x^- x} + e^{-ik_x^- x}\right)\left(C_4^- e^{+ik_y^- y} + e^{-ik_y^- y}\right) e^{-i\omega t} \end{aligned} \tag{4.2.10}$$

And equation (4.2.7) becomes:

$$\begin{aligned} v_x &= v_x^+ + v_x^- \\ &= -\frac{1}{\rho_0 a_0} \frac{k_x}{k_0} \frac{C_1}{1 - M_{z,0} k_z^+ / k_0} e^{+ik_z^+ z} \left(C_3^+ e^{+ik_x^+ x} + e^{-ik_x^+ x}\right)\left(C_4^+ e^{+ik_y^+ y} + e^{-ik_y^+ y}\right) e^{-i\omega t} \\ &\quad - \frac{1}{\rho_0 a_0} \frac{k_x}{k_0} \frac{C_2}{1 + M_{z,0} k_z^- / k_0} e^{-ik_z^- z} \left(C_3^- e^{+ik_x^- x} + e^{-ik_x^- x}\right)\left(C_4^- e^{+ik_y^- y} + e^{-ik_y^- y}\right) e^{-i\omega t} \end{aligned} \tag{4.2.11}$$

again, with similar equations for v_y and v_z. From the boundary conditions, one obtains:

$$C_3^{\pm}=\frac{\dfrac{Z_x k_x^{\pm}}{\rho_0 a_0 k_0}-\left(1\mp\dfrac{M_{z,0}k_z^{\pm}}{k_0}\right)^2}{\dfrac{Z_x k_x^{\pm}}{\rho_0 a_0 k_0}+\left(1\mp\dfrac{M_{z,0}k_z^{\pm}}{k_0}\right)^2},\ C_3^{\pm}=\frac{\dfrac{Z_x k_x^{\pm}}{\rho_0 a_0 k_0}+\left(1\mp\dfrac{M_{z,0}k_z^{\pm}}{k_0}\right)^2}{\dfrac{Z_x k_x^{\pm}}{\rho_0 a_0 k_0}-\left(1\mp\dfrac{M_{z,0}k_z^{\pm}}{k_0}\right)^2}\frac{e^{-ik_x^{\pm}D_x}}{e^{+ik_x^{\pm}D_x}}$$
$$C_4^{\pm}=\frac{\dfrac{Z_y k_y^{\pm}}{\rho_0 a_0 k_0}-\left(1\mp\dfrac{M_{z,0}k_z^{\pm}}{k_0}\right)^2}{\dfrac{Z_y k_y^{\pm}}{\rho_0 a_0 k_0}+\left(1\mp\dfrac{M_{z,0}k_z^{\pm}}{k_0}\right)^2},\ C_4^{\pm}=\frac{\dfrac{Z_y k_y^{\pm}}{\rho_0 a_0 k_0}+\left(1\mp\dfrac{M_{z,0}k_z^{\pm}}{k_0}\right)^2}{\dfrac{Z_y k_y^{\pm}}{\rho_0 a_0 k_0}-\left(1\mp\dfrac{M_{z,0}k_z^{\pm}}{k_0}\right)^2}\frac{e^{-ik_y^{\pm}D_y}}{e^{+ik_y^{\pm}D_y}} \tag{4.2.12}$$

The next step is to eliminate $C_3^{\pm}$ and $C_4^{\pm}$. Each set of boundary conditions are combined to obtain:

$$\left(\frac{Z_x k_x^{\pm}}{\rho_0 a_0 k_0}\right)^2-\frac{2}{i}\cot k_x^{\pm}D_x)\frac{Z_x k_x^{\pm}}{\rho_0 a_0 k_0}\left(1\mp\frac{M_{z,0}k_z^{\pm}}{k_0}\right)^2+\left(1\mp\frac{M_{z,0}k_z^{\pm}}{k_0}\right)^4=0$$
$$\left(\frac{Z_y k_y^{\pm}}{\rho_0 a_0 k_0}\right)^2-\frac{2}{i}\cot(k_y^{\pm}D_y)\frac{Z_y k_y^{\pm}}{\rho_0 a_0 k_0}\left(1\mp\frac{M_{z,0}k_z^{\pm}}{k_0}\right)^2+\left(1\mp\frac{M_{z,0}k_z^{\pm}}{k_0}\right)^4=0 \tag{4.2.13}$$

One then utilizes quadratic equation to solve equation (4.2.13).

$$\frac{Z_x k_x^{\pm}}{\rho_0 a_0 k_0}=i\frac{-\cos(k_x^{\pm}D_x)\pm^{*}1}{\sin(k_x^{\pm}D_x)}\left(1\mp\frac{M_{z,0}k_z^{\pm}}{k_0}\right)^2$$
$$\frac{Z_y k_y^{\pm}}{\rho_0 a_0 k_0}=i\frac{-\cos(k_y^{\pm}D_y)\pm^{*}1}{\sin(k_y^{\pm}D_y)}\left(1\mp\frac{M_{z,0}k_z^{\pm}}{k_0}\right)^2 \tag{4.2.14}$$

Both equations are a set of two equations:

$$\frac{Z_x k_x^{\pm}}{\rho_0 a_0 k_0}=i\tan\left(\frac{k_x^{\pm}D_x}{2}\right)\left(1\mp\frac{M_{z,0}k_z^{\pm}}{k_0}\right)^2,\ \frac{Z_x k_x^{\pm}}{\rho_0 a_0 k_0}=-i\cot\left(\frac{k_x^{\pm}D_x}{2}\right)\left(1\mp\frac{M_{z,0}k_z^{\pm}}{k_0}\right)^2$$
$$\frac{Z_y k_y^{\pm}}{\rho_0 a_0 k_0}=i\tan\left(\frac{k_y^{\pm}D_y}{2}\right)\left(1\mp\frac{M_{z,0}k_z^{\pm}}{k_0}\right)^2,\ \frac{Z_y k_y^{\pm}}{\rho_0 a_0 k_0}=-i\cot\left(\frac{k_y^{\pm}D_y}{2}\right)\left(1\mp\frac{M_{z,0}k_z^{\pm}}{k_0}\right)^2 \tag{4.2.15}$$

As with the previous problem, the solution to each set of equations in (4.2.15) represent symmetric and antisymmetric modes.

Next, take the low-frequency approximation. The previous discussion still holds, so one simply takes the small-angle approximation of equations (4.2.15). Note one only needs to proceed with the equations on the left-hand side, since they correspond to the symmetric modes. If the others were used, there would be no solution for the wavenumbers because since transverse antisymmetric modes can't exist in the low-frequency regime. One obtains the following for the wavenumbers:

$$\begin{aligned}\left(k_x^{\pm}\right)^2 &= -2i\frac{\rho_0 a_0 k_0}{D_x Z_x}\left(1 \mp \frac{M_{z,0}k_z^{\pm}}{k_0}\right)^2 \\ \left(k_y^{\pm}\right)^2 &= -2i\frac{\rho_0 a_0 k_0}{D_y Z_y}\left(1 \mp \frac{M_{z,0}k_z^{\pm}}{k_0}\right)^2\end{aligned} \tag{4.2.16}$$

To obtain the wavenumber in z first insert the transverse wavenumbers, equations (4.2.16), into the dispersion relation, equation (4.2.4):

$$\left(M_{z,0}^2\left(1+i\frac{\rho_0 a_0 \xi_{Mun}}{k_0}\right)-1\right)\left(k_z^{\pm}\right)^2 \mp 2M_{z,0}k_0\left(1+i\frac{\rho_0 a_0 \xi_{Mun}}{k_0}\right)k_z^{\pm} + k_0^2\left(1+i\frac{\rho_0 a_0 \xi_{Mun}}{k_0}\right) = 0$$

$$\xi_{Mun} \equiv 2\left(\frac{1}{D_x Z_x}+\frac{1}{D_y Z_y}\right)$$

(4.2.17)

One then solves equation (4.2.17) for $k_z^{\pm}$:

$$k_z^{\pm} = \frac{k_0\sqrt{\left(1+i\frac{\rho_0 a_0 \xi_{Mun}}{k_0}\right)}}{\left(1\pm M_{z,0}\sqrt{\left(1+i\frac{\rho_0 a_0 \xi_{Mun}}{k_0}\right)}\right)} \tag{4.2.18}$$

Note the (-) solution was chosen. Compare this directly to the CVA result, equation (3.4.2):

$$\begin{aligned} &\xi_v \to 0 \\ &\xi_Z \to 2\left(\frac{1}{D_x Z_x}+\frac{1}{D_y Z_y}\right) \\ &k_z^{\pm} \to \frac{k_0\sqrt{1+i\frac{\rho_0 a_0 \xi_Z}{k_0}}}{1\pm M_{z,0}\sqrt{1+i\frac{\rho_0 a_0 \xi_Z}{k_0}}} \end{aligned} \tag{4.2.19}$$

The CVA solution matches the plane wave version of Munjal's solution. This result begs the question of why to even consider using the CVA when one can just use Munjal's method to obtain the full 3D solution or just the 1D solution in the plane wave limit. Munjal's method does incorporate axial mean-flow and transverse impedances, but it does not include mean-flow impinging through the side walls, even in the plane wave limit. The CVA method does include this effect.

The purpose of this section was to initially assess the results of the CVA analysis. While transverse mean-flows are not considered in this section, the comparison with Munjal's method in the plane wave limit provides some initial confidence in the CVA method. Further comparisons with experiments and numerical methods are needed to assess the accuracy of the CVA method.

Chapter 5

Application Cases

The results section outlines two applications for the CVA. This first application is a closed-closed duct, in which a closed acoustic boundary condition is imposed at both z boundaries. Application two is a zero mass-flow rate oscillation - choked nozzle duct, in which the unsteady mass flow-rate is set to zero at $z = 0$ and a choked nozzle condition is imposed at $z = D_z$. In each case, the duct is subdivided into two sub-ducts, each with different properties. A consequence of splitting the duct into two sub-ducts is that each sub-duct now has its own equations for pressure, velocity, etc. They are given by:

$$\begin{aligned} p_{1-2}'(z_{1-2},t) &= \left(\mathrm{A}_{1-2}e^{+ik^{+}_{z,1-2}z_{1-2}} + \mathrm{B}_{1-2}e^{-ik^{-}_{z,1-2}z_{1-2}}\right)e^{-i\omega t} \\ v_{z,1-2}'(z_{1-2},t) &= \frac{1}{\rho_{0,1-2}a_{0,1-2}}\left(\mathrm{A}_{1-2}\Upsilon^{+}_{1-2}e^{+ik^{+}_{z,1-2}z_{1-2}} + \mathrm{B}_{1-2}\Upsilon^{-}_{1-2}e^{-ik^{-}_{z,1-2}z_{1-2}}\right)e^{-i\omega t} \end{aligned} \tag{5.0.1}$$

with

$$\begin{aligned} z_1 &= z, && z \le D_{z,1} \\ z_2 &= z - D_{z,1}, && z \ge D_{z,2} \end{aligned} \tag{5.0.2}$$

The two sub-ducts are then matched via conservation of mass and momentum. In cases where the properties in each sub-duct are the same, the problem reverts to a single duct problem. The main difference between the closed – closed and m-dot – nozzle cases is the presence of axial mean-flow. Indeed, this becomes apparent in the forthcoming mathematical treatment of each case. In each case the effect of various parameters on the eigen-frequency, the mode shapes, and the

frequency response are examined. The parameters considered are transverse wall impedance, transverse wall mean-flow, and temperature difference between sub-ducts. Axial mean-flow is only considered in the m-dot – nozzle case, as a closed-closed duct cannot support axial mean-flow through it. The temperature is included implicitly through other gas properties in each sub-duct.

In order to better understand the ramifications of each parameter on the system, each parameter is considered individually. This is to elucidate the effect of each parameter. When multiple parameters are considered at once, an understanding of each parameter provides a starting point to understanding multiple effects, particularly if the coupling of parameters causes unique behavior unseen with individual parameters.

There are three primary results: the eigenfrequency, the axial wavenumber, and the mode shape/frequency response. The real part of the eigenfrequency is the frequency of the system that would be measured in the lab. The imaginary part of the eigenfrequency represents the temporal driving/damping of the system. If it is negative, it damps the system in time. If it is positive, it drives the system in time. This is due to the $-i\omega t$ time convention. Next is the axial wavenumber, given by equation (3.4.2). The imaginary part of the axial wavenumber represents the spatial damping or driving. For the $+z$ wave component, a negative sign on the imaginary component of the axial wavenumber is driving, while a positive sign is damping. For the $-z$ wave component, a negative sign on the imaginary component is damping, while a positive sign is driving. Finally, the mode shapes and frequency response help show the locations of the resonant frequencies and display damping and driving in the frequency domain. For a more complete discussion, see chapter 6.

The governing equations are put in the form of a matrix equation $\underline{A}\vec{x} = \vec{b}$. In order to calculate the eigen-frequencies one must solve $|\underline{A}| = 0$. If the system is driven at the exact complex eigen-frequency the determinant of the matrix $\underline{A}$ is zero and therefore non-invertible. This makes the matrix equation unsolvable. In order to evaluate the mode shapes and frequency response, a constant volume velocity term is included in the analysis. This extra term modifies $\vec{b}$ such that it is no longer equal to the zero vector. The time dependence of the volume velocity term is assumed to be the same of the pressure and velocity, i.e. $e^{-i\omega t}$. Note that this volume velocity term is assumed to be added at the junction of the two sub-ducts. The axial wavenumber is given completely by equation (3.4.2). Each sub-duct has its own distinct set of axial wavenumber, regardless of the boundary condition at each end. Therefore the examination of the axial wavenumber is presented primarily in chapter six, rather than here in chapter 5.

5.1 - Closed-Closed Duct

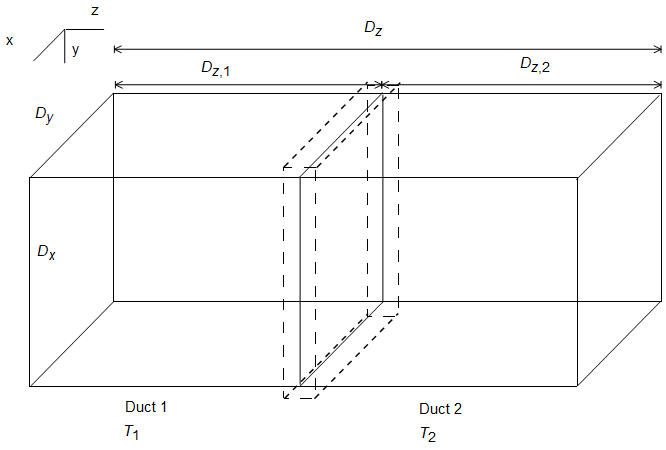

Figure 5.1: Basic Layout of the Closed-Closed Duct Problem

5.1.1 - Problem Setup

Consider the closed-closed duct shown in Fig. 5.1. The dashed box outline indicates the control volume in which conservation of mass and momentum will be carried out. In the closed-closed case, there is no axial mean-flow. Therefore, the relevant quantities from the CVA become:

$$\begin{aligned} M_{z,0} &\to 0 \\ k_z^{\pm} &\to k_z = \sqrt{\left(k_0 + i\xi_M\right)\left(k_0 + i(\xi_M + \xi_{\mathcal{Z}})\right)} \\ \Upsilon^{\pm} &\to \Upsilon = \frac{1}{k_z}\left(k_0 + i(\xi_M + \xi_{\mathcal{Z}})\right) \end{aligned} \tag{5.1.1}$$

The boundary conditions at each end of the duct are given by:

$$\begin{aligned} v_z'(0,t) &= 0 \\ v_z'(D_z,t) &= 0 \end{aligned} \tag{5.1.2}$$

The matching conditions are derived through the conservation of mass and momentum. Consider equation (3.1.1), conservation of mass in its integral form. The first term in equation (3.1.1) goes to zero since only an infinitesimal sliver of the control volume around the interface of the two sub-ducts is considered. The second term is carried out for each control surface. This brings the question of how to include the volume velocity to the forefront. The volume velocity is assumed to be inserted through the transverse surfaces of the control volume in Fig. 3.1. Rather than consider each 4 transverse control surfaces separately, a single aggregate control surface is considered, denoted with the number 3. Carrying out the integrals on each control surface yields:

$$\rho_1\left(\vec{v}_1 \cdot \hat{n}_1\right)S_1 + \rho_2\left(\vec{v}_2 \cdot \hat{n}_2\right)S_2 + \rho_3\left(\vec{v}_3 \cdot \hat{n}_3\right)S_3 = 0 \tag{5.1.3}$$

One then performs a Reynolds decomposition on the density and velocity terms. After neglecting the purely steady and higher order terms one obtains:

$$\begin{aligned}&\rho_{0,1}\left(\vec{v}_1'\cdot\hat{n}_1\right)S_1+\rho_1'\left(\vec{v}_{0,1}\cdot\hat{n}_1\right)S_1+\\&\rho_{0,2}\left(\vec{v}_2'\cdot\hat{n}_2\right)S_2+\rho_2'\left(\vec{v}_{0,2}\cdot\hat{n}_2\right)S_2+\\&\rho_{0,3}\left(\vec{v}_3'\cdot\hat{n}_3\right)S_3+\rho_3'\left(\vec{v}_{0,3}\cdot\hat{n}_3\right)S_3=0\end{aligned}\tag{5.1.4}$$

Carrying out the dot products:

$$-\rho_{0,1}v_1'S_1-\rho_1'v_{0,1}S_1+\rho_{0,2}v_2'S_2+\rho_2'v_{0,2}S_2-\rho_{0,3}v_3'S_3-\rho_3'v_{0,3}S_3=0\tag{5.1.5}$$

Equation (5.1.5) is the general matching condition for conservation of mass. One can then use the isentropic equation of state, equation (3.1.5), the definition of the pressure and velocity, equations (5.0.1), and the CVA parameters (5.1.1) to obtain:

$$-\frac{\Upsilon_1}{a_{0,1}}S_1\mathrm{A}_1e^{+ik_{z,1}D_{z,1}}+\frac{\Upsilon_1}{a_{0,1}}S_1\mathrm{B}_1e^{-ik_{z,1}D_{z,1}}+\frac{\Upsilon_2}{a_{0,2}}S_2\mathrm{A}_2-\frac{\Upsilon_2}{a_{0,2}}S_2\mathrm{B}_2=\rho_{0,3}U_3'\tag{5.1.6}$$

Equation (5.1.6) is the continuity condition that will be used for the closed-closed problem.

Consider conservation of momentum in its integral form, equation (3.2.1). As with conservation of momentum the volume term is assumed to be zero since the control volume is infinitesimally thin. Carrying out the remaining integrals over each control surface yields:

$$\begin{aligned}&\rho_1\vec{v}_1\left(\vec{v}_1\cdot\hat{n}_1\right)S_1+p_1\hat{n}_1S_1+\\&\rho_2\vec{v}_2\left(\vec{v}_2\cdot\hat{n}_2\right)S_2+p_2\hat{n}_2S_2+\\&\rho_3\vec{v}_3\left(\vec{v}_3\cdot\hat{n}_3\right)S_3+p_3\hat{n}_3S_3=0\end{aligned}\tag{5.1.7}$$

Again, a Reynolds decomposition is performed, and the purely steady and higher order terms are neglected.

$$\begin{aligned}&\rho_{0,1}\vec{v}_{0,1}(-v_{z,1}')S_1+\rho_{0,1}\vec{v}_1'(-v_{z,0,1})S_1+\rho_1'\vec{v}_{0,1}(-v_{z,0,1})S_1+p_1\hat{n}_1S_1+\\&\rho_{0,2}\vec{v}_{0,2}(v_{z,2}')S_2+\rho_{0,2}\vec{v}_2'(v_{z,0,2})S_2+\rho_2'\vec{v}_{0,2}(v_{z,0,2})S_2+p_2\hat{n}_2S_2+\\&\rho_{0,3}\vec{v}_{0,3}(-v_3')S_3+\rho_{0,3}\vec{v}_3'(-v_{0,3})S_3+\rho_3'\vec{v}_{0,3}(-v_{0,3})S_3+p_3\hat{n}_3S_3=0\end{aligned}\tag{5.1.8}$$

Equation (5.1.8) is dotted with $+\hat{z}$, the direction of wave propagation, becoming:

$$\begin{aligned} &-2\rho_{0,1}v_{z,0,1}v_{z,1}{}'S_1 - \rho_1{}'v_{z,0,1}^2 S_1 - p_1{}'S_1 + \\ &\quad 2\rho_{0,2}v_{z,0,2}v_{z,2}{}'S_2 + \rho_2{}'v_{z,0,2}^2 S_2 + p_2{}'S_2 = 0 \end{aligned} \tag{5.1.9}$$

Equation (5.1.9) is the general matching condition for conservation of momentum. In the closed-closed problem, axial mean-flows are zero:

$$-p_1{}'S_1 + p_2{}'S_2 = 0 \tag{5.1.10}$$

Inserting equations (5.0.1) into equation (5.1.10) yields:

$$-\mathrm{A}_1 e^{+ik_{z,1}D_{z,1}} - \mathrm{B}_1 e^{-ik_{z,1}D_{z,1}} + \left(\mathrm{A}_2 + \mathrm{B}_2\right)\frac{S_2}{S_1} = 0 \tag{5.1.11}$$

Equation (5.1.11) is the matching momentum continuity condition that will be used for the closed-closed problem. For the remainder of the problem the cross-sectional areas of each sub-duct are assumed to be equal. Next are the two boundary conditions given by equation (5.1.2). Inserting equations (5.0.1) yields:

$$\begin{aligned} \mathrm{A}_1 - \mathrm{B}_1 &= 0 \\ \mathrm{A}_2 e^{+ik_{z,2}D_{z,2}} - \mathrm{B}_2 e^{-ik_{z,2}D_{z,2}} &= 0 \end{aligned} \tag{5.1.12}$$

Equations (5.1.6), (5.1.10), and (5.1.12) constitute the system of equations for the closed-closed case. In matrix form the system is:

$$\begin{bmatrix} 1 & -1 & 0 & 0 \\ 0 & 0 & e^{+ik_{z,2}D_{z,2}} & -e^{-ik_{z,2}D_{z,2}} \\ -\dfrac{\Upsilon_1}{a_{0,1}}e^{+ik_{z,1}D_{z,1}} & \dfrac{\Upsilon_1}{a_{0,1}}e^{-ik_{z,1}D_{z,1}} & \dfrac{\Upsilon_2}{a_{0,2}} & -\dfrac{\Upsilon_2}{a_{0,2}} \\ -e^{+ik_{z,1}D_{z,1}} & -e^{ik_{z,1}D_{z,1}} & 1 & 1 \end{bmatrix} \begin{bmatrix} \mathrm{A}_1 \\ \mathrm{B}_1 \\ \mathrm{A}_2 \\ \mathrm{B}_2 \end{bmatrix} = \begin{bmatrix} 0 \\ 0 \\ \rho_{0,3}U_3{}' \\ 0 \end{bmatrix} \tag{5.1.13}$$

By setting the 4x4 matrix in equation (5.1.13) to zero, one can obtain the eigen-frequency. The resulting equation is not solvable analytically, and therefore is solved numerically. The coefficients, however, have the following analytical solution.

$$
\begin{aligned}
\mathrm{A}_1 &= i\frac{a_{0,1}a_{0,2}\rho_{0,3}U_3'}{2\sin\left(k_{z,1}D_{z,1}\right)\Upsilon_1 a_{0,2}+2\cos\left(k_{z,1}D_{z,1}\right)\Upsilon_2 a_{0,1}\tan\left(k_{z,2}D_{z,2}\right)} \\
\mathrm{B}_1 &= i\frac{a_{0,1}a_{0,2}\rho_{0,3}U_3'}{2\sin\left(k_{z,1}D_{z,1}\right)\Upsilon_1 a_{0,2}+2\cos\left(k_{z,1}D_{z,1}\right)\Upsilon_2 a_{0,1}\tan\left(k_{z,2}D_{z,2}\right)} \\
\mathrm{A}_2 &= i\frac{a_{0,1}a_{0,2}\rho_{0,3}U_3' e^{-ik_{z,2}D_{z,2}}}{2\sin\left(k_{z,2}D_{z,2}\right)\Upsilon_2 a_{0,1}+2\cos\left(k_{z,2}D_{z,2}\right)\Upsilon_1 a_{0,2}\tan\left(k_{z,1}D_{z,1}\right)} \\
\mathrm{B}_2 &= i\frac{a_{0,1}a_{0,2}\rho_{0,3}U_3' e^{+ik_{z,2}D_{z,2}}}{2\sin\left(k_{z,2}D_{z,2}\right)\Upsilon_2 a_{0,1}+2\cos\left(k_{z,2}D_{z,2}\right)\Upsilon_1 a_{0,2}\tan\left(k_{z,1}D_{z,1}\right)}
\end{aligned}
\tag{5.1.14}
$$

Note that despite the *i* in front of each coefficient, the coefficients themselves are not purely imaginary. This is because, of course, many of the variables which make up the coefficients are complex. Writing equations (5.1.14) in terms of the real and imaginary parts would be far too unwieldy to be useful.

5.1.2 - Eigenfrequency Solution

5.1.2a - Baseline Solution

To begin, the eigenfrequency problem is unconcerned with the forcing, as the eigenfrequencies only depend on the 4x4 matrix in equation (5.1.13). A baseline eigenfrequency is established by 'turning off' each variable from the CVA. That is, the eigenfrequency is calculated from a simple closed-closed duct with acoustically rigid walls and no axial mean-flow assuming plane-wave acoustic propagation. For this analysis, the transverse impedances and mean-flows are set to 0, and both sub-ducts at the same temperature. Therefore, all properties in each sub-duct are now equal. The relevant CVA quantities become:

$$
\begin{aligned}
k_{z,1} &= k_{z,2} = k_z = k_0 \\
\Upsilon_1 &= \Upsilon_2 = \Upsilon = \frac{k_0}{k_z} = 1
\end{aligned}
\tag{5.1.15}
$$

The problem is now that of a single duct. Care must be taken when converting from z_1 and z_2 to z:

$$
\begin{aligned}
z_1 = 0 &\rightarrow z = 0 \\
z_1 = D_{z,1} &\rightarrow z = D_{z,1} \\
z_2 = 0 &\rightarrow z = D_{z,1} \\
z_2 = D_{z,2} &\rightarrow z = D_z
\end{aligned}
\tag{5.1.16}
$$

The governing matrix becomes

$$
\begin{bmatrix}
1 & -1 & 0 & 0 \\
0 & 0 & e^{+ik_zD_z} & -e^{-ik_zD_z} \\
-e^{+ik_zD_{z,1}} & e^{-ik_zD_{z,1}} & e^{+ik_zD_{z,1}} & -e^{-ik_zD_{z,1}} \\
-e^{+ik_zD_{z,1}} & -e^{ik_zD_{z,1}} & e^{+ik_zD_{z,1}} & e^{-ik_zD_{z,1}}
\end{bmatrix}
\tag{5.1.17}
$$

Note equations 3 and 4, the matching conditions across the duct junction, do not contribute. They are 0 = 0. Indeed, this forces the volume velocity forcing term to 0. Therefore, the system is:

$$
\begin{bmatrix}
1 & -1 \\
e^{+ik_zD_z} & -e^{-ik_zD_z}
\end{bmatrix}
\tag{5.1.18}
$$

Taking the determinant, setting it equal to 0, and using equation (5.1.18) reduces the resulting equation to:

$$
\sin\left(k_zD_z\right) = 0
\tag{5.1.19}
$$

Thus:

$$k_z = \frac{n\pi}{D_z}, n \in \mathbb{Z} \tag{5.1.20}$$

It is worth noting that equations (5.1.18), (5.1.19), and (5.1.20) apply to all closed-closed cases in which the properties in each sub-duct are equal. Combining the relations $k_0 = \omega / a_0$, $\omega = 2\pi f$, and equation (5.1.15) with equation (5.1.20):

$$f_b = \frac{na_0}{2D_z}, n \in \mathbb{Z} \tag{5.1.21}$$

This is the baseline solution that all other solutions will be compared against. While *n* can validly be 0 or any real integer, all practical values are $n \geq +1$. The baseline eigenfrequencies, equation (5.1.21), are the familiar classical results for a 1D closed – closed duct. The eigenfrequency is purely real and depends solely on the speed of sound of the duct and the length of the duct in the axial direction. The mode, given by the integer *n*, can be 0 or any positive integer.

5.1.2b - Finite Transverse Wall Impedances

Consider transverse walls with a finite impedance. The relevant CVA properties are

$$\begin{aligned} k_z &\to \sqrt{k_0\left(k_0 + i\xi_{\mathcal{Z}}\right)} \\ \Upsilon &\to \frac{k_0 + i\xi_{\mathcal{Z}}}{k_z} = \sqrt{\frac{k_0 + i\xi_{\mathcal{Z}}}{k_0}} \end{aligned} \tag{5.1.22}$$

Inserting equation (5.1.22) into equation (5.1.20) yields:

$$\sqrt{k_0\left(k_0 + i\xi_{\mathcal{Z}}\right)} = \frac{n\pi}{D_z}, n \in \mathbb{Z} \tag{5.1.23}$$

Solving this equation for k_0 and subsequently f one obtains:

$$f = \frac{a_0}{2\pi}\left(\pm\sqrt{\left(\frac{n\pi}{D_z}\right)^2 - \left(\frac{\xi_{\mathcal{Z}}}{2}\right)^2} - i\frac{\xi_{\mathcal{Z}}}{2} \right), n \in \mathbb{Z} \tag{5.1.24}$$

Note the $\pm$ in equation (5.1.24) is merely a holdover from the quadratic equation and is chosen such that the real part of the eigenfrequency is positive. To ensure this, simply set the impedance parameter to 0. In this case the (+) is chosen in order to match with equation (5.1.21). For the rest of this sub-section, the $n \in \mathbb{Z}$ affix shall be dropped for the sake of brevity.

Equation (5.1.24) is complicated by the fact that the transverse wall impedances can be complex, and thus the impedance parameter can also be complex. Re-writing in terms of the real and imaginary component:

$$\xi_{\mathcal{Z}} \to \xi_{\mathcal{Z},r} + i\xi_{\mathcal{Z},i} \tag{5.1.25}$$

Assuming all transverse wall impedances are equal equation (5.1.25) can be written as:

$$\xi_{\mathcal{Z}} = 2\left(\frac{1}{D_x} + \frac{1}{D_y}\right)\left(\frac{\theta - i\chi}{\theta^2 + \chi^2}\right) \tag{5.1.26}$$

where θ is the resistive component of the impedance and χ is the reactive component of the impedance. Thus, if the impedance is purely real the impedance parameter is also purely real. The same applies if the impedance is purely imaginary. Inserting equation (5.1.25) into equation (5.1.24) yields

$$f = \frac{a_0}{2\pi}\left(\frac{\xi_{\mathcal{Z},i}}{2} + \sqrt{\left(\frac{n\pi}{D_z}\right)^2 - \frac{\xi_{\mathcal{Z},r}^2 - \xi_{\mathcal{Z},i}^2}{4} - i\frac{\xi_{\mathcal{Z},r}\xi_{\mathcal{Z},i}}{2}} - i\frac{\xi_{\mathcal{Z},r}}{2} \right) \tag{5.1.27}$$

One could continue to split the radical into real and imaginary parts, but the resulting expression is far too unwieldy to be useful or provide insight. Suffice it to say, both the real and imaginary components of the impedance parameter contribute to both the real and the imaginary part of the eigenfrequency.

First consider purely resistive impedances. Equation (5.1.27) becomes

$$f = \frac{a_0}{2\pi}\left(\sqrt{\left(\frac{n\pi}{D_z}\right)^2 - \frac{\xi_{Z,r}^2}{4}} - i\frac{\xi_{Z,r}}{2}\right) \tag{5.1.28}$$

Equation (5.1.28) mirrors the form of equation (5.1.24). Thus, for all finite resistive impedances, the eigenfrequency is either complex or purely imaginary.

Next consider a completely reactive impedance value. Equation (5.1.27) becomes:

$$f = \frac{a_0}{2\pi}\left(\frac{\xi_{Z,i}}{2} + \sqrt{\left(\frac{n\pi}{D_z}\right)^2 + \frac{\xi_{Z,i}^2}{4}}\right) \tag{5.1.29}$$

In this case the frequency is purely real for all values of the impedance parameter. Because both positive and negative reactance values are valid, it is worth noting that for positive reactance's, the eigenfrequency increases. If the reactance is negative, the frequency decreases. No matter how large the magnitude of the reactance, these trends never change.

Equation (5.1.28) presents interesting behavior. As stated earlier, the eigenfrequency will either be complex or purely imaginary. What determines this is the term in the radical. Thus, 3 regimes for the value of the impedance parameter come to the forefront: $\xi_{Z,r} < 2n\pi / D_z$, $\xi_{Z,r} = 2n\pi / D_z$, and $\xi_{Z,r} > 2n\pi / D_z$. This critical value for the impedance parameter is derived by

setting the term in the radical to zero and solving the resulting equation. When the first inequality is true, the eigenfrequency takes on a complex value. For the other two inequalities, the resulting eigenfrequency is completely imaginary. While such eigenvalues are permitted by the mathematics, these solutions are not physically valid. Therefore, this critical impedance is a like a cut-off impedance. Beyond this cut-off impedance there are no physically valid eigenfrequencies. Assuming all 4 transverse wall impedances are equal, the cut-off impedance is:

$$\mathcal{Z}_{co} = \frac{D_z}{n\pi}\frac{D_x + D_y}{D_x D_y} \tag{5.1.30}$$

If the impedance is below the cut-off impedance, certain modes cannot propagate. Note the dependence on the mode number *n*. For higher order modes, the cut-off impedance decreases. As the area of the duct decreases, so too does the cut-off impedance. For very small ducts, this cut-off impedance can become very high, and could possibly be used to filter low frequency modes. For the fundamental frequency, $D_x = D_y = 0.1\,\mathrm{m}$, and $D_z = 1\,\mathrm{m}$ the cut-off impedance is 20/π, or 6.366. That is to say, the cut-off transverse wall impedances are 6.366 times that of the bulk impedance of air. If the walls are made of an acoustically hard materials like steel, this would never be observed. For complicated acoustic liners with smaller acoustic impedances, this could be within the realm of possibility. However, when other effects are included, there is no hard cut-off impedance value, as equation (5.1.28).

A visual representation of equations (5.1.24), (5.1.28), and (5.1.29) are shown in Figs. 5.6 – 5.10, 5.2 - 5.4, and 5.5, respectively. They, and all subsequent calculations, are obtained for the following duct properties:

Duct Width, D_x	0.1 m
Duct Height, D_y	0.1 m
Duct Length, D_z	1.0 m
Duct Temperature, T	300 K
Duct Pressure, P_0	1 atm

Table 5.1: Duct Properties

In each case the transverse wall impedances are assumed to be equal. For cases in which the main duct is sub-divided into two ducts the following properties are assumed unless otherwise noted:

Length of Sub-Duct 1	0.4 m
Length of Sub-Duct 2	0.6 m

Table 5.2: Sub-Duct Properties

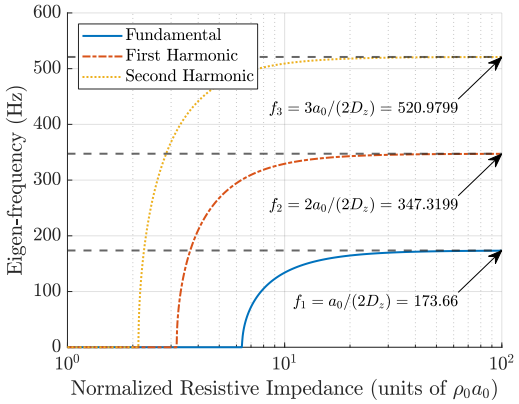

Figure 5.2: Real Part of the Eigenfrequencies as a Function of Purely Resistive Impedance

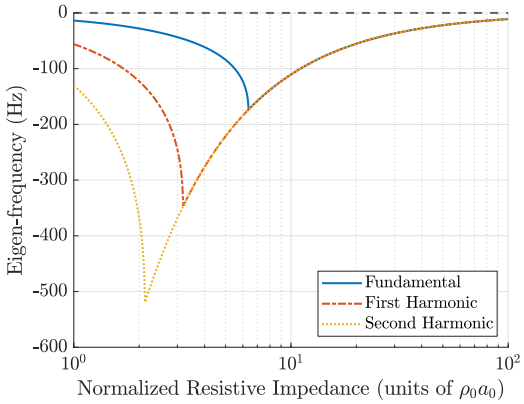

Figure 5.3: Imaginary Part of the Eigenfrequencies as a Function of Purely Resistive Impedance

Fig. 5.2 shows the real part of the eigenfrequency, the frequency, as a function of purely resistive transverse wall impedances (i.e. equation (5.1.28)), for the first 3 modes. The range of transverse wall impedance is $\rho_0 a_0$ to $100\rho_0 a_0$ of air at 300 K and 1 atm. These values were chosen as $\rho_0 a_0$ corresponds to a wall made out of air (i.e. no wall at all), and $100\rho_0 a_0$ is sufficiently large that the transverse walls are essentially rigid. Only positive resistive impedances are considered, as negative acoustic resistance is not possible. Fig. 5.3 shows the imaginary part of the eigenfrequency, the driving/damping, for the same case. In Fig. 5.2 the base eigenfrequency is indicated for each mode. For large resistive impedances, the frequency approaches the baseline

results given by equation (5.1.21). For smaller resistive impedances, the frequency quickly drops to zero. The cut-off impedance is clearly shown as the point the real part becomes zero. As equation (5.1.30) indicates the cut-off impedance decreases for higher modes. Fig. 5.3 shows the imaginary part of the eigenfrequency for the same case. As with the real part, the cut-off impedance is clearly visible as a 'kink.' Before the cut-off impedance for the fundamental, all modes have the same imaginary component of the eigenfrequency. This is because above the cut-off impedance the imaginary part of the eigenfrequency is solely determined by the transverse wall resistance, not the mode number. After the cut-off impedance, the mode number plays a role in determining the imaginary part of the eigenfrequency. With resistive impedances, only damping is possible as the imaginary component of the eigenfrequency is negative for all values of resistive impedance. The greatest amount of damping is at the cut-off impedance for each mode.

Fig. 5.4 shows the damping factor as a function of resistive impedance for the first three modes. Fig. 5.5 shows the real part of the eigenfrequency for the first three modes as a function of resistive transverse wall impedances (i.e. equation (5.1.29)).

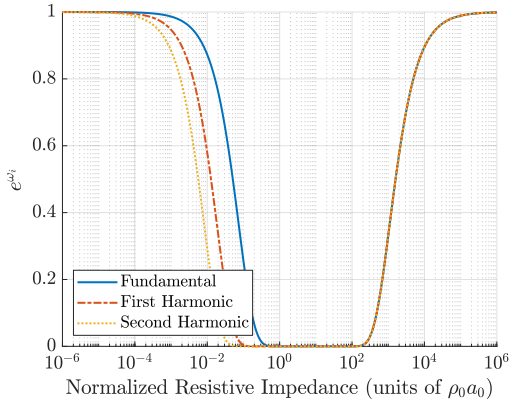

Figure 5.4: Damping Factor as a Function of Purely Resistive Impedance

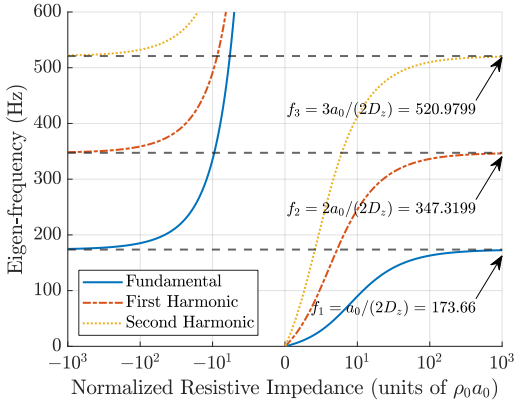

Figure 5.5: Real Part of the Eigenfrequencies as a Function of Purely Reactive Impedance

Fig. 5.4 is an alternative representation of Fig. 5.3. If the damping factor is equal to unity, the mode will propagate in time, since the damping factor is a coefficient of the pressure. Fig. 5.4 shows that the transverse walls must, realistically, be rigid in order for any mode to propagate with purely resistive impedances. The damping factor returns to unity for very small values of normalized impedance. However, to the authors knowledge such small resistive acoustic impedances are not possible. For all intents and purposes, non-rigid resistive impedances will cause a large amount of acoustic damping.

Now consider purely reactive transverse wall impedances, equation (5.1.29). For this case, it is only necessary to look at the real part of the eigenfrequency, since it will always be purely real, i.e. Fig. 5.5. Unlike resistive impedances, negative values are permissible for reactive impedances. In Fig. 5.5 there is an asymptote near zero. When approaching from negative reactive impedances, the eigenfrequency approaches $+\infty$. However, when approaching from positive reactive impedances, the eigenfrequency approaches 0. Clearly, the analysis breaks down for small impedances. This is to be expected and was never an intended regime for this analysis. Nevertheless, for decreasing negative reactive impedances, the eigenfrequency increases, and for decreasing positive reactive impedances, the eigenfrequency decreases. However, in the real-world duct elements are not purely resistive or reactive but are complex.

Next consider fully complex impedances, i.e. equation (5.1.24). Rather than plot the entire parameter space, consider how plots 5.2 – 5.4 might change with a reactive component of the transverse wall impedance, in order to better illustrate its effect. These changes are shown in Figs. 5.6 – 5.9. Figs. 5.6 and 5.7 show how the fundamental frequency (shown in blue in Figs. 5.2 – 5.5) is affected by increasing values of transverse wall reactance. As the reactance increases, the curve slowly transitions to a horizontal line at the base eigenfrequency for the fundamental. This is

because the overall magnitude of the transverse impedance is becoming quite large, and therefore the transverse walls are becoming progressively more acoustically rigid. The same smooth transition is seen in the imaginary part of the eigenfrequency, Fig. 5.7.

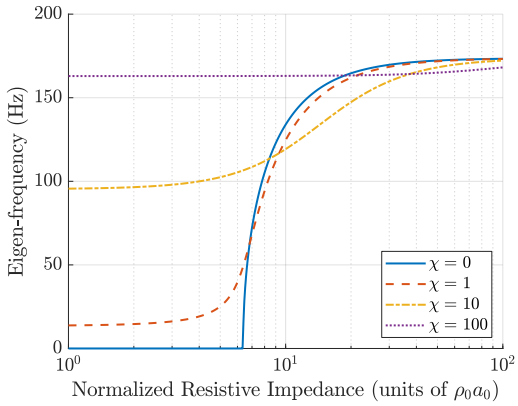

Figure 5.6: Real Part of the Eigenfrequencies as a Function of Purely Resistive Impedance for Increasing χ

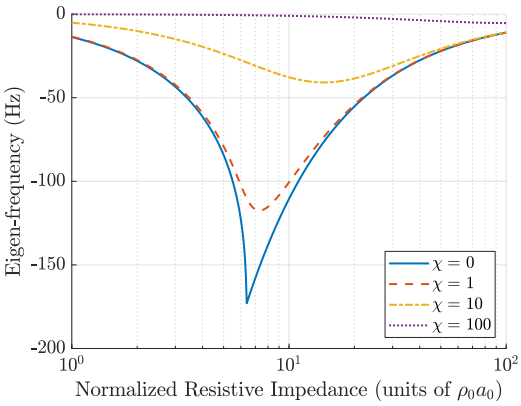

Figure 5.7: Imaginary Part of the Eigenfrequencies as a Function of Purely Resistive Impedance for Increasing χ

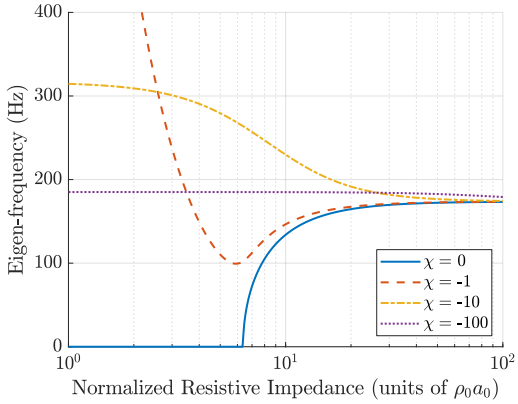

Figure 5.8: Real Part of the Eigenfrequencies as a Function of Purely Resistive Impedance for Decreasing χ

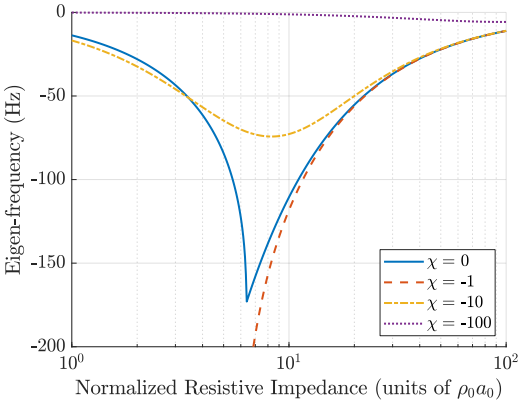

Figure 5.9: Imaginary Part of the Eigenfrequencies as a Function of Purely Resistive Impedance for Decreasing χ

Figs. 5.8 and 5.9 are the counterparts of Figs. 5.6 and 5.7 but with decreasing transverse wall reactance. The behavior seen in these figures is quite different. Rather than smoothly transition from the base eigenfrequency curves seen in Figs. 5.2 and 5.3, non-zero reactances have a dramatic effect when the wall resistances are small. As the reactance continues to decrease, the curves damp down to the base values, as with Figs. 5.6 and 5.7. This discrepancy seems problematic, but it is

the same behavior seen in Fig. 5.5, suggesting that one can simply layer the effects of transverse wall resistance and reactance on top of one another. Furthermore, this behavior is only seen when the total impedance value is quite small. These small values are not realistic values seen in transverse walls of combustors.

Fig. 5.10 shows the damping factor as a function of the resistance and reactance. The damping factor is shown for a very large range of resistance and reactance values. For "small" values of resistance and reactance (i.e. below $1000\rho_0 a_0$), the fundamental does not propagate in time. This is largely the same story as in Fig. 5.4.

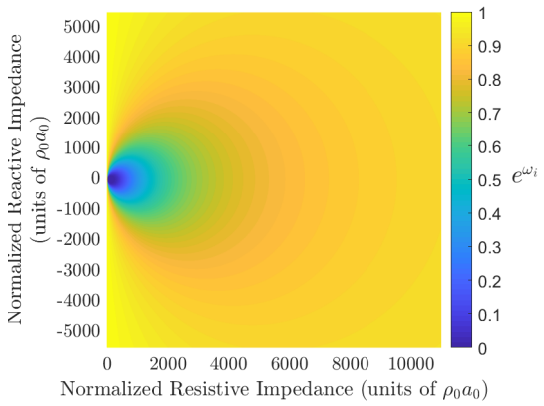

Figure 5.10: Damping Factor as a Function of Complex Impedance

5.1.2c - Non-Zero Transverse Wall Mean-Flows

One must take care that continuity is observed when introducing transverse mean-flows. Intuitively, what comes in must go out. Thus, certain conditions must be imposed on the transverse mean-flow if the restriction of no axial mean-flow is to be preserved. To derive these conditions, consider a plain duct like that in Fig. 5.1, but with no junction or sub-ducts. Applying conservation of mass, equation (3.1.1), to the duct, taking a Reynolds decomposition, and taking only the steady parts of the equation yields:

$$\begin{aligned}&\frac{1}{D_x}\left(\rho_0\vec{v}_0\cdot\hat{n}\right)_{x=0}+\frac{1}{D_x}\left(\rho_0\vec{v}_0\cdot\hat{n}\right)_{x=D_x}\\&+\frac{1}{D_y}\left(\rho_0\vec{v}_0\cdot\hat{n}\right)_{y=0}+\frac{1}{D_y}\left(\rho_0\vec{v}_0\cdot\hat{n}\right)_{y=D_y}\\&+\frac{1}{D_z}\left(\rho_0\vec{v}_0\cdot\hat{n}\right)_{z=0}+\frac{1}{D_z}\left(\rho_0\vec{v}_0\cdot\hat{n}\right)_{z=D_z}=0\end{aligned}\tag{5.1.31}$$

Carrying out the dot products and converting to Mach number yields:

$$\frac{M_{z,0}}{D_z}\left(\left(\hat{n}_v\cdot\hat{n}\right)_{z=0}+\left(\hat{n}_v\cdot\hat{n}\right)_{z=D_z}\right)-\xi_M=0\tag{5.1.32}$$

Here unit vectors subscripted with *v* denote the direction of the axial mean-flow velocity at a given *z*-position. Since the surface unit normals at $z=0$ and $z=D_z$ are always pointing in the opposite direction, the first term in equation (5.1.32) goes to zero leaving:

$$\xi_M=0\tag{5.1.33}$$

Thus, for a single duct with no axial mean-flow, no transverse mean-flow is allowed. However, if one subdivides the duct into two sub-ducts, as in Fig. 5.1, carrying out conservation of mass in the same manner yields:

$$\begin{aligned}\rho_{0,1}a_{0,1}\left(M_0\hat{n}_v\cdot\hat{n}\right)_{z_1=0}+\rho_{0,2}a_{0,2}\left(M_0\hat{n}_v\cdot\hat{n}\right)_{z_2=D_z}\\+D_{z,1}\rho_{0,1}a_{0,1}\xi_{M,1}+D_{z,2}\rho_{0,2}a_{0,2}\xi_{M,2}=0\end{aligned}\tag{5.1.34}$$

Equation (5.1.34) shows the interdependencies of the mean-flows. For this analysis, 3 of the parameters will be considered known *a priori*, and the remaining parameter will be calculated from equation (5.1.34). For the closed-closed problem, the axial mean-flows can be set to zero:

$$D_{z,1}\rho_{0,1}a_{0,1}\xi_{M,1}+D_{z,2}\rho_{0,2}a_{0,2}\xi_{M,2}=0\tag{5.1.35}$$

If the gas properties in each duct are the same, then, essentially, the transverse mean-flows in duct two are the negative of the mean-flows in duct one. In other words, what comes in sub-duct 1 goes out sub-duct 2.

The relevant CVA properties are:

$$\begin{aligned} k_z &\to k_0 + i\xi_M \\ \Upsilon &\to \frac{k_0 + i\xi_M}{k_z} = 1 \end{aligned} \tag{5.1.36}$$

Because some of the parameters are different in each sub-duct, equation (5.1.20) can no longer be used. Simplifying the 4x4 matrix in equation (5.1.13) yields:

$$\begin{bmatrix} 1 & -1 & 0 & 0 \\ 0 & 0 & e^{+ik_{z,2}D_{z,2}} & -e^{-ik_{z,2}D_{z,2}} \\ -e^{+ik_{z,1}D_{z,1}} & e^{-ik_{z,1}D_{z,1}} & 1 & -1 \\ -e^{+ik_{z,1}D_{z,1}} & -e^{ik_{z,1}D_{z,1}} & 1 & 1 \end{bmatrix} \tag{5.1.37}$$

After taking the determinant and setting it equal to 0, one has:

$$\sin\left(k_{z,1}D_{z,1} + k_{z,2}D_{z,2}\right) = 0 \tag{5.1.38}$$

Solving for the eigenfrequency yields:

$$f = \frac{na_0}{2D_z} - i\frac{a_0}{2\pi}\frac{\xi_{M,1}D_{z,1} + \xi_{M,2}D_{z,2}}{D_z} \tag{5.1.39}$$

Substituting equation (5.1.35) into equation (5.1.39) one obtains

$$f = \frac{na_0}{2D_z} - i\frac{a_0}{2\pi}\frac{-\rho_{0,2}a_{0,2} / \rho_{0,1}a_{0,1} + 1}{D_z}\xi_{M,2}D_{z,2} \tag{5.1.40}$$

The properties in each duct are equal for this case. Thus

$$f = \frac{na_0}{2D_z} \tag{5.1.41}$$

Thus, the presence of transverse mean-flow only affects the eigenfrequency if the density, sound speed, or both are different in each duct when no axial mean-flow is present. When considered in conjunction with other effects, this changes.

5.1.2d - Non-Zero Sub-Duct Temperature Difference

Fig. 5.11 shows the real part of the eigenfrequency as a function of sub-duct temperature difference.

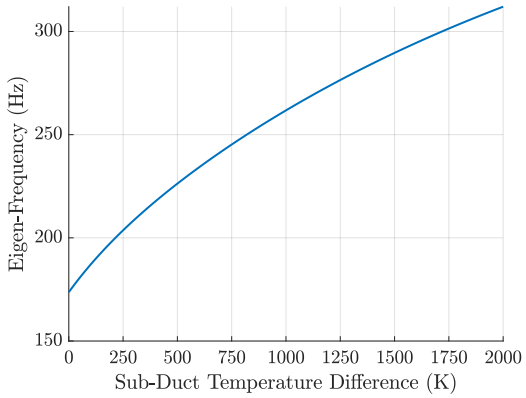

Figure 5.11:Real Part of the Eigenfrequency as a Function of Sub-Duct Temperature Difference

Unlike the previous two cases, a simple temperature difference between the sub-ducts does not simplify to an analytical solution. The numerical solution is straightforward and is shown in Fig. 5.11. As the sub-duct temperature difference increases, so too does the real part of the eigenfrequency. This makes sense intuitively. As the temperature increases the speed of sound increases, thus it is expected that the natural frequencies in the duct will also increase. The imaginary part stays zero for all values of sub-duct temperature difference, i.e. temperature difference alone does not damp or drive the duct.

5.1.2e - Combination of Parameters

Consider the combination of transverse wall impedances with transverse mean-flow. As with section 5.1.2d, there is no analytical solution to this case. Indeed, most subsequent cases do not have analytical expressions for the eigenfrequency. As before, numerical solutions are obtained. Figs. 5.12 – 5.15 show the combined effect of transverse wall impedance and mean-flow. Figs. 5.12 and 5.13 show the eigenfrequency as a function of resistive transverse wall impedance with a transverse wall reactance of $+100\rho_0 a_0$. Figs. 5.14 and 5.15 show the same but with the reactance equal to $-100\rho_0 a_0$. In all four figures, the transverse mean-flow values are $M_{t,1} = \pm 0.1$ and $M_{t,2} = \mp 0.0\overline{6}$.

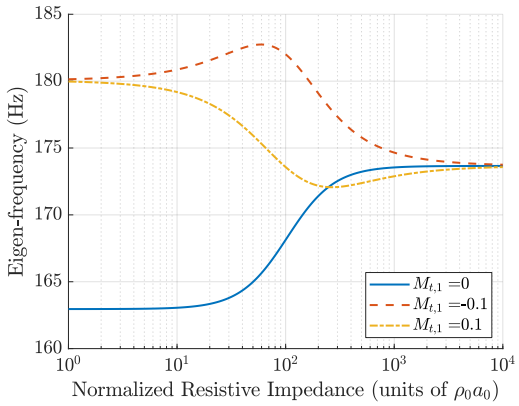

Figure 5.12: Real Part of the Fundamental Eigenfrequency as a Function of Resistive Impedance with Transverse Mean-Flow, χ = +100, and Sub-Duct Junction at z = 0.4 m

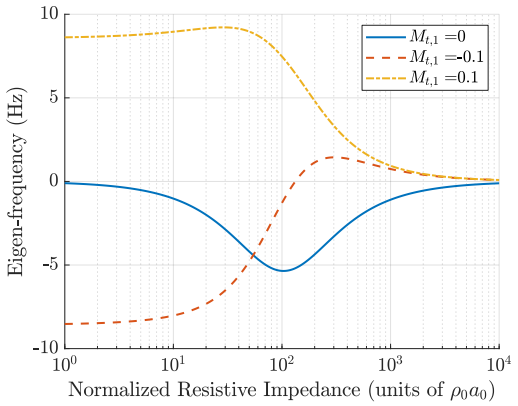

Figure 5.13: Imaginary Part of the Fundamental Eigenfrequency as a Function of Resistive Impedance with Transverse Mean-Flow, χ = +100, and Sub-Duct Junction at z = 0.4 m

Consider Figs. 5.12 – 5.15. Figs. 5.12 and 5.13 have a reactance of +100. The reactance in Figs. 5.14 and 5.15 is -100. Even though the impedances are still quite large compared to air, the sign of the reactive impedance still can matter a great deal. For positive reactive impedance, the frequency is increased for smaller resistances (Fig. 5.12). For negative reactive impedance, the frequency is decreased for smaller resistances (Fig. 5.14). In both cases the sign of the transvers mean-flow influences the frequency, but the overall trend is the same. This is not true for the

damping/driving. For small resistances, the sign of the transverse mean-flow determines if there is damping or driving. With positive reactive impedance, flow into sub-duct 1 leads to damping, while flow out of sub-duct 1 leads to driving. This trend is reversed with negative reactive impedance.

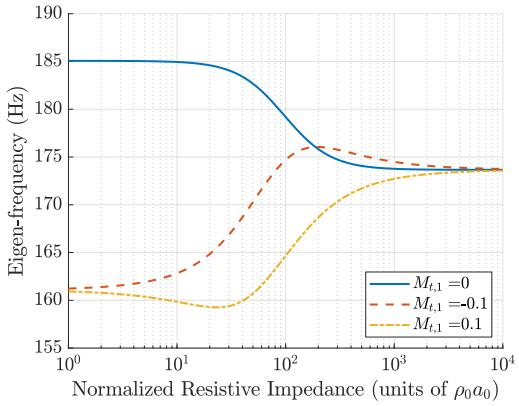

Figure 5.14: Real Part of the Fundamental Eigenfrequency as a Function of Resistive Impedance with Transverse Mean-Flow, χ = -100, and Sub-Duct Junction at z = 0.4 m

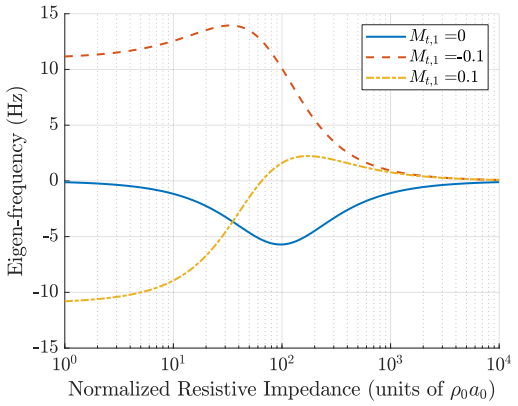

Figure 5.15: Imaginary Part of the Fundamental Eigenfrequency as a Function of Resistive Impedance with Transverse Mean-Flow, χ = -100, and Sub-Duct Junction at z = 0.4 m

It is worth noting the effect of the sub-duct junction itself in this case. Figs. 5.16 – 5.19 are the same as Figs. 5.12 – 5.15, but with the sub-duct junction located at z = 0.5 m.

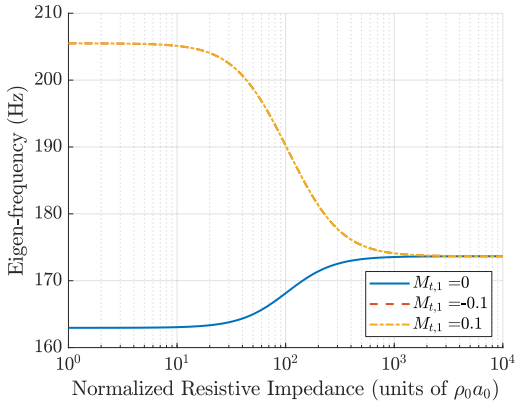

Figure 5.16: Real Part of the Fundamental Eigenfrequency as a Function of Resistive Impedance with Transverse Mean-Flow, χ = +100, and Sub-Duct Junction at z = 0.5 m

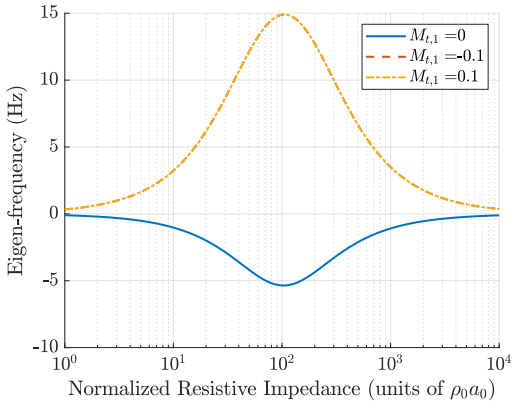

Figure 5.17: Imaginary Part of the Fundamental Eigenfrequency as a Function of Resistive Impedance with Transverse Mean-Flow, χ = +100, and Sub-Duct Junction at z = 0.5 m

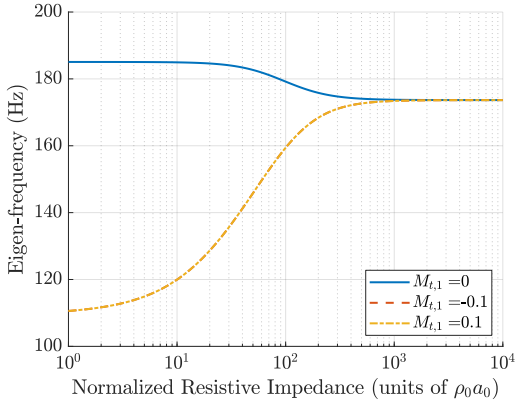

Figure 5.18: Real Part of the Fundamental Eigenfrequency as a Function of Resistive Impedance with Transverse Mean-Flow, χ = -100, and Sub-Duct Junction at z = 0.5 m

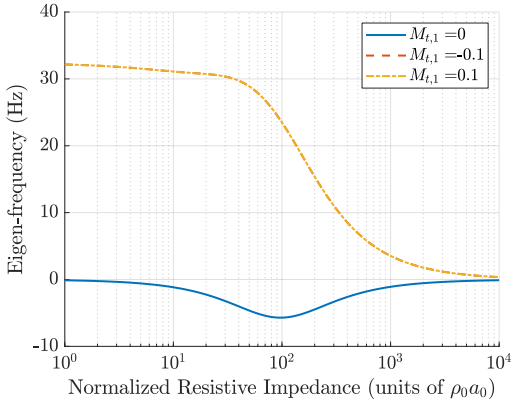

Figure 5.19: Imaginary Part of the Fundamental Eigenfrequency as a Function of Resistive Impedance with Transverse Mean-Flow, χ = -100, and Sub-Duct Junction at z = 0.5 m

Equation (5.1.34) and (5.1.35) both show a dependence upon each sub-duct length. Figs. 5.16 – 5.19 show the effect of the location of the sub-duct junction and are the counterparts to Figs. 5.12 – 5.15. Because the transverse mean-flow is weighted by the respective sub-ducts, by making the length and gas properties equal for both sub-ducts, there is no difference between mean-flow entering and exiting one sub-duct or another. Thus, the role of the sign of the reactive impedance component becomes clear, since the direction of transverse mean-flow in sub-duct 1 ceases to matter. Each case is equivalent.

Figs. 5.20 and 5.21 show the effect of each parameter layered for the real and imaginary parts of the eigenfrequency, respectively. The cases which feature finite transverse wall impedances sets all the transverse wall impedances to $\mathcal{Z} = 100 + 100i$, with the transverse wall impedances in sub-duct 2 scaled appropriately with temperature (due to normalization). In the cases which have transverse mean-flow, the transverse mean-flow Mach numbers in sub-duct 1 are set to -0.1 and

the mean-flow Mach numbers in sub-duct two are set according to equation(5.1.35). Its values range from $0.0\overline{6}$ to 0.192.

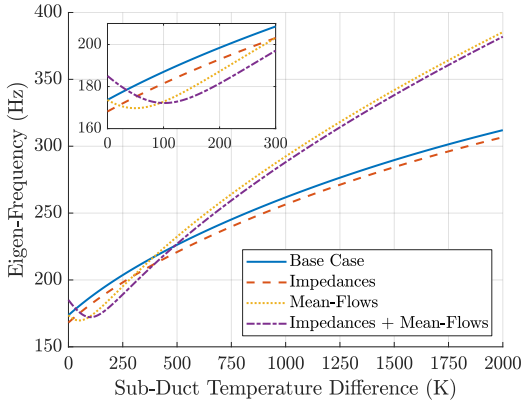

Figure 5.20: Real Part of the Fundamental Eigenfrequency as a Function of Temperature for (a) Baseline, (b) Transverse Impedances, (c) Transverse Mean-Flows, (d) Transverse Impedances + Mean-Flows

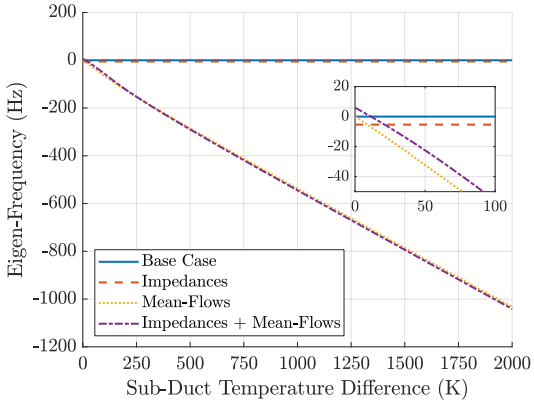

Figure 5.21: Imaginary Part of the Fundamental Eigenfrequency as a Function of Temperature for (a) Baseline, (b) Transverse Impedances, (c) Transverse Mean-Flows, (d) Transverse Impedances + Mean-Flows

The interplay between transverse impedance, transverse mean-flow, and sub-duct temperature difference is complicated. However, if one neglects transverse mean-flow, the differences between a rigid walled duct and a nearly rigid walled duct are quite small. For the real part of the eigenfrequency the differences are hardly worth mentioning. While the differences for the imaginary part of the eigenfrequency are also small, they are quite significant. The duct has gone from having no damping to having some damping. The introduction of transverse mean-flow drastically changes the frequency response for sub-duct temperature difference. First the damping increases drastically with temperature. Second, for the first 100 Kelvins of temperature increase the real part of the eigenfrequency decreases. This is quite counter-intuitive as it is expected that increasing temperatures lead to increasing frequencies.

5.1.3 - Mode Shapes and Frequency Response

To plot the mode shapes, one calculates the A's and B's with equation (5.1.14), and plugs them into equations (5.0.1). The duct properties used are those in tables 5.1 and 5.2. A value of 1 m/s

times the cross-sectional area of the duct is used for the forcing term U_3', and it is assumed that $\rho_{0,3} = \rho_{0,1}$. For the mode shapes the system is driven at 10 Hz below the baseline fundamental eigenfrequency, 163.66 Hz. The mode shapes plotted are the pressure amplitude and phase as a function of the axial coordinate *z*. For the frequency response a 1-500 Hz sweep is performed, and the acoustic pressure is measured at the point $z = D_z$.

5.1.3a - Baseline Solution

Figs. 5.22 and 5.23 show the baseline mode shapes. In Fig. 5.22 there is a small kink visible at $z = 0.4$. This is the location of the sub-duct junction and where the forcing of the system is introduced. The mode shape is as expected for a closed-closed duct, with the derivative of the pressure (which is proportional to the velocity) going to zero at each end. The phase is shown in Fig. 5.23. The phase jumps from -π/2 to π/2 at the point in the pressure amplitude minimum, around 0.47 m. The sub-duct junction does not affect the phase for the baseline case.

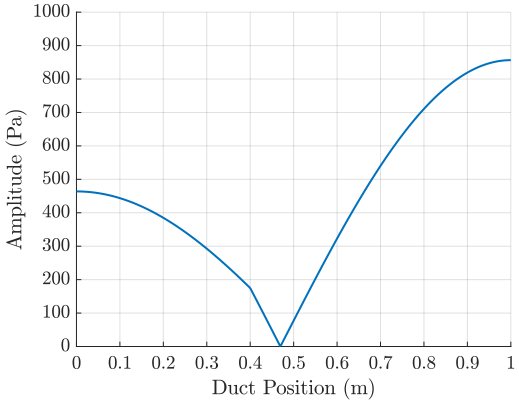

Figure 5.22: Baseline Pressure Amplitude as a Function of Duct Position

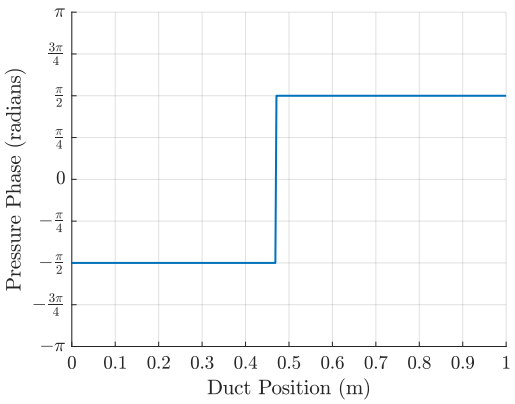

Figure 5.23: Baseline Pressure Phase as a Function of Duct Position

The baseline frequency response of the duct at the outlet is show in Fig. 5.24. The black vertical line indicates the driving frequency. The frequency response looks different than expected. Rather

than have a perfectly symmetric frequency response around each eigenfrequency, there is a dip at ~210 Hz. This is due to inserting a volume velocity forcing term at the sub-duct junction.

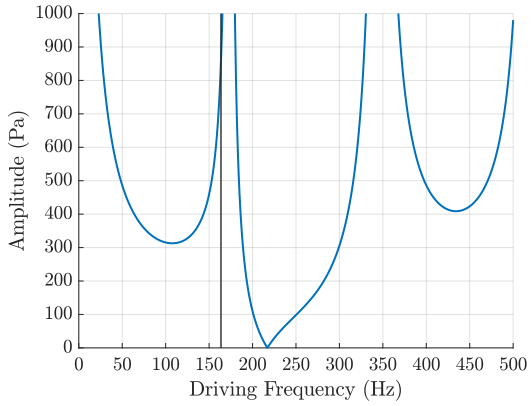

Figure 5.24: Baseline Frequency Response at Outlet with Junction at z = 0.4 m

The effect of the sub-duct junction is examined in Figs. 5.25 and 5.26. Fig. 5.25 shows the base frequency response when the sub-duct junction is ~ 0 m, and Fig. 5.26 show the base frequency response when the sub-duct junction is exactly in the middle, 0.5 m. Fig. 5.25 shows essentially the pure frequency response for a single duct. This is because the forcing has been moved to approximately the left end, i.e. $z \approx 0$. Fig. 5.26 has volume velocity forcing at the middle of the duct. Because of this, certain modes naturally damped due to the location of the sub-duct junction. If the frequency sweep were to extend far enough, any location in the duct will damp any higher order mode which has a pressure node at the sub-duct junction location.

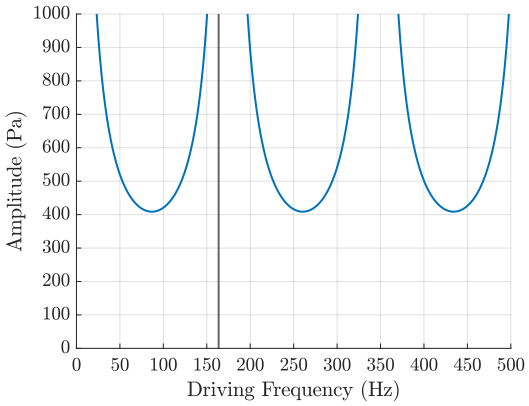

Figure 5.25: Baseline Frequency Response at Outlet with Junction at z ≈ 0 m

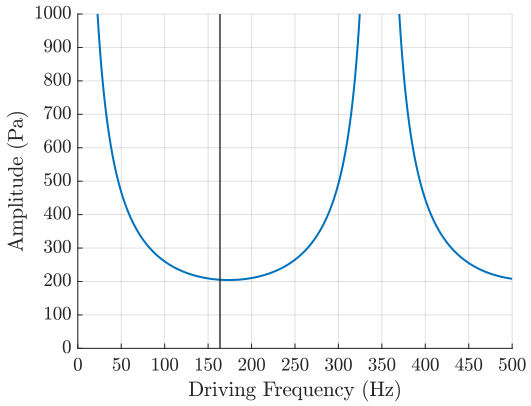

Figure 5.26: Baseline Frequency Response at Outlet with Junction at z = 0.5 m

5.1.3b - Finite Transverse Wall Impedances

Begin by considering only resistive transverse wall impedances. Figs. 5.27 and 5.28 show the effects of resistive transverse impedances upon the mode-shapes. As suggested by equation (5.1.28), a finite resistive impedance causes temporal damping in the system and possibly shifts the resonant frequency. This cannot be seen directly by Fig. 5.27, but they can be inferred. As the transverse walls become decreasingly rigid, the damping increases. For the phase of the pressure, there is a net increase in the phase throughout the duct as the transverse walls become less rigid. Furthermore, the step that is present in the baseline case is smoothed out, and the 'kink' from the sub-duct junction can be seen.

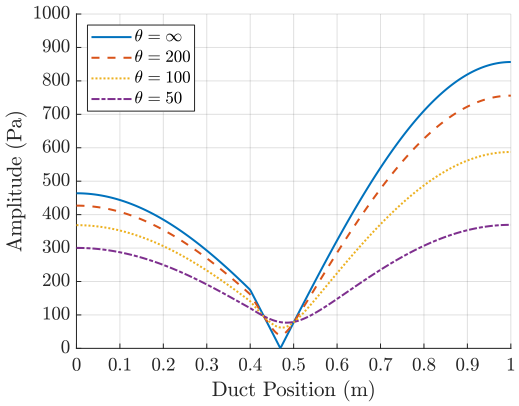

Figure 5.27: Pressure Amplitude as a Function of Duct Position for Various Resistive Impedances

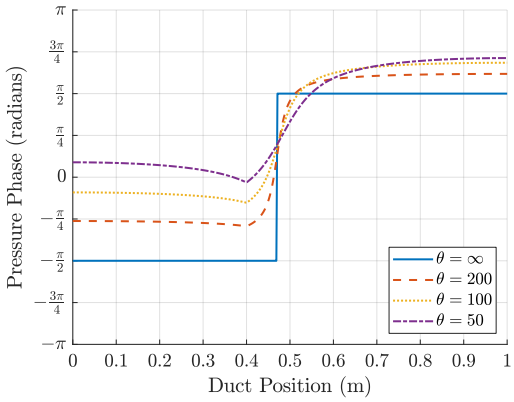

Figure 5.28: Pressure Phase as a Function of Duct Position for Various Resistive Impedances

Figs. 5.29 and 5.30 show the frequency response. Fig. 5.29 shows the frequency response for various resistive impedances as a function of driving frequency. Fig. 5.30 shows the frequency response as a function of driving frequency and resistive impedance. From both figures it is obvious that as the transverse walls become less rigid there is significant damping in the frequency space. The frequency shifting effect from equation (5.1.28) is very subtle in these plots, as the damping dominates. If one looks closely at Fig. 5.29 one can see the resonant frequency shifting

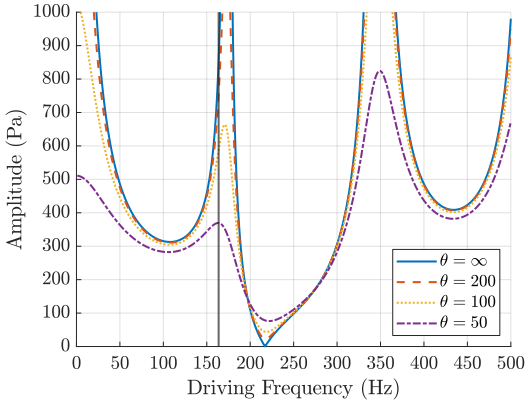

Figure 5.29: Frequency Response for Various Resistive Impedances

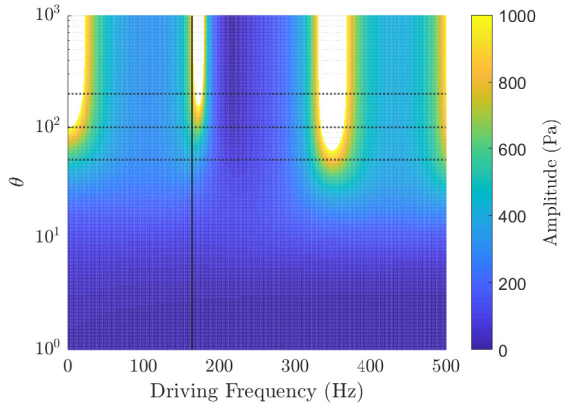

Figure 5.30: Frequency Response as a Function of Driving Frequency and Transverse Resistive Impedance

down very slightly. This effect is quite small for impedances far from the cut-off impedance. This makes sense, taking Fig. 5.2 into account. The resonant frequency does not change significantly until a normalized transverse wall impedance around 10.

Next consider purely reactive wall impedances. Figs. 5.31 and 5.32 show the same plots as 5.27 and 5.28 but with reactive impedances instead.

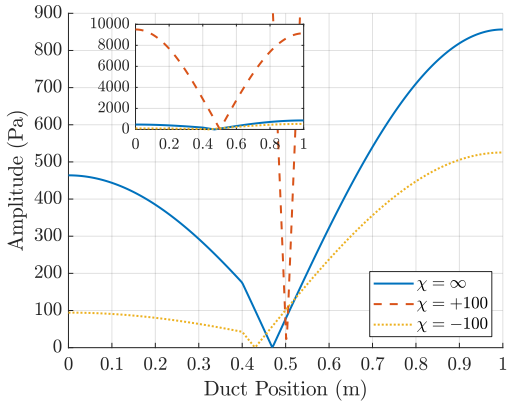

Figure 5.31: Pressure Amplitude as a Function of Duct Position for Various Reactive Impedances

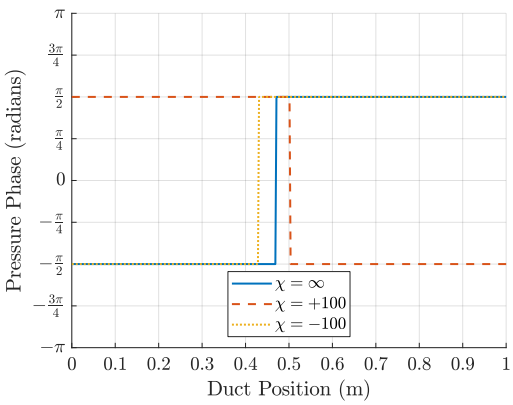

Figure 5.32: Pressure Phase as a Function of Duct Position for Various Reactive Impedances

Unlike resistive impedances, the reactive impedance has had an extremely large effect for a value of +100, but not for a value of -100. To better understand this, consider equation (5.1.29). The fundamental eigenfrequency calculated for each case are 173.66 Hz, 162.96 Hz, and 185.07 Hz, respectively. There is no damping introduced by a purely reactive transverse wall impedance, but the eigenfrequencies have shifted. In the case of -100, the driving frequency is quite close to the fundamental eigenfrequency for that case. Therefore, the frequency response is quite high.

The frequency response for reactive impedances is given by Figs. 5.33 and 5.34. The solid vertical line is the driving frequency. The two dotted horizontal lines indicate the reactive impedance values used in Figs. 5.31 – 5.33.

The frequency shifting effect is easily seen in the frequency response plots. The shape of the frequency response is unchanged for the purely reactive transverse wall impedances, merely shifted to the left or right. Fig. 5.34 also shows this effect, but in a stunning fashion. For small positive values of χ the resonant frequencies become small and closer together, forming a region which is highly unstable. The opposite occurs for small negative values of χ. Because the resonant frequencies shift up, the region is devoid of any frequency response, and is stable.

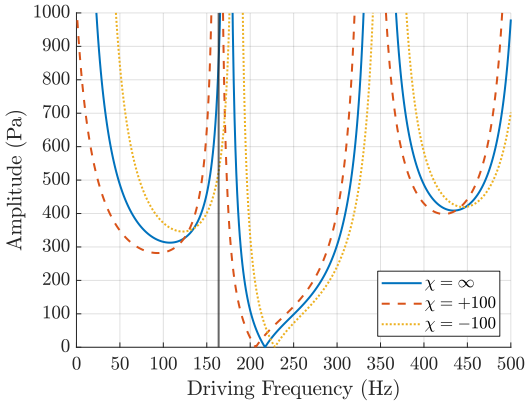

Figure 5.33: Frequency Response for Various Reactive Impedances

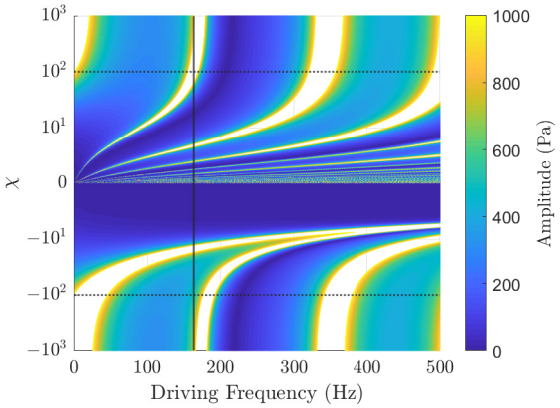

Figure 5.34: Frequency Response as a Function of Driving Frequency and Reactive Impedance

Finally, consider fully complex transverse impedances. Figs. 5.35 and 5.36 give the pressure amplitude and phase, respectively.

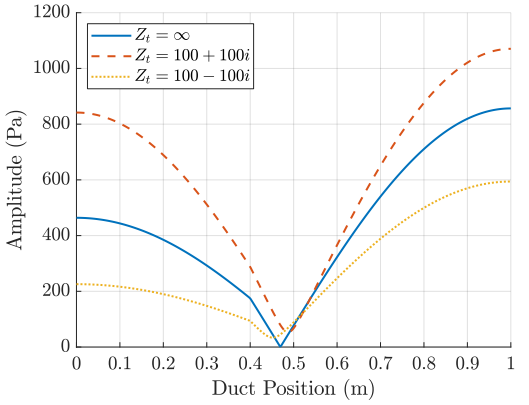

Figure 5.35: Pressure Amplitude as a Function of Duct Position for Various Complex Impedances

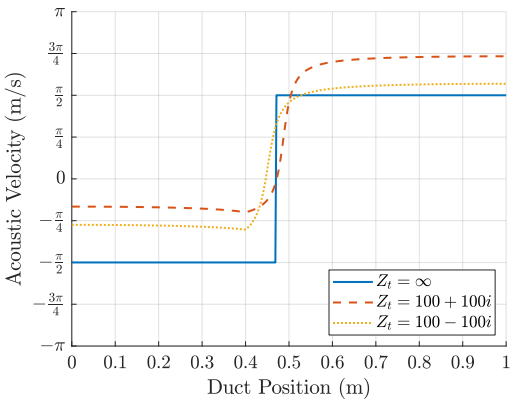

Figure 5.36: Velocity Amplitude as a Function of Duct Position for Various Complex Impedances

The expectation is to see the damping effect and frequency response shifting effect layered on top of one another. This is difficult to see in Figs. 5.35 and 5.36. Consider the frequency response shown in Figs. 5.37 and 5.38.

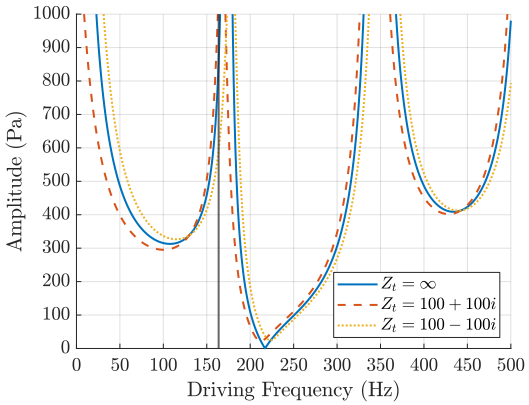

Figure 5.37: Frequency Response for Various Complex Impedances

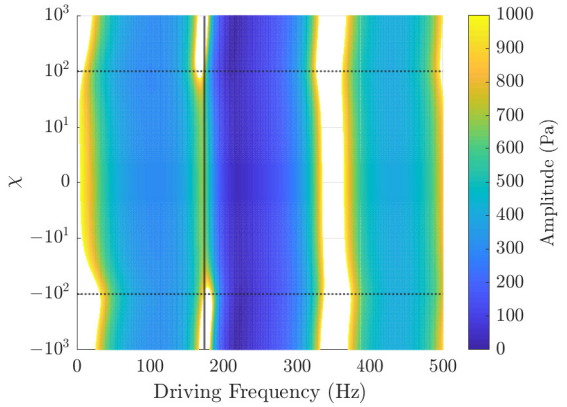

Figure 5.38: Frequency Response as a Function of Driving Frequency and Transverse Reactive Impedance

In Fig. 5.37 the frequency shifting due to the reactive impedance is clear. However, the presence of a resistive impedance component damps this behavior, and the aggregate effect is to simply provide damping proportional to the magnitude of the transverse wall impedance.

5.1.3c - Non-Zero Transverse Wall Mean-Flows

The pressure amplitude and phase are plotted in Figs. 5.39 and 5.40, respectively. The pressure modes are peculiar, as one would expect that swapping the direction of transverse mean-flow in duct 1 would have an appreciable effect on the mode shapes. This is not the case. It appears that if there is only transverse mean-flow the effect is symmetric with respect to the direction of the transverse mean-flow. Nonetheless there is slight driving towards the left end of the duct and slight damping near the right end of the duct. The phase tells another story. The phase of the pressure distinguishes the difference between mean-flow entering sub-duct 1 and mean-flow leaving sub-duct 1. If one looks closely the two phases are symmetric about the phase angle -π/2.

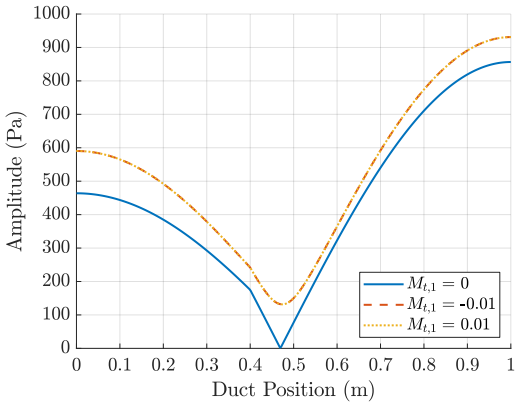

Figure 5.39: Pressure Amplitude as a Function of Duct Position for Various Transverse Mean-Flows

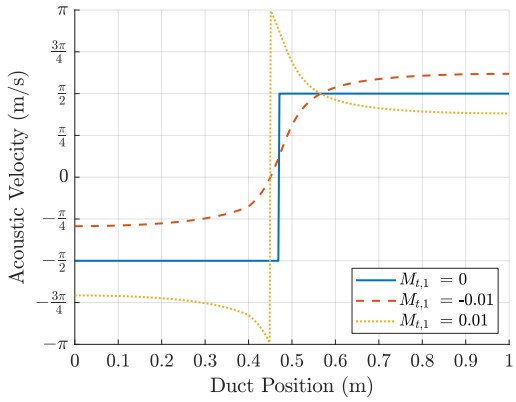

Figure 5.40: Pressure Phase as a Function of Duct Position for Various Transverse Mean-Flows

Figs. 5.41 and 5.42 show the frequency response. In Fig. 5.41 the two curves which feature transverse mean-flow are virtually indistinguishable from the reference, except for the region of around 175 – 275 Hz. Fig. 5.42 further illuminates the frequency response. As noted in the previous paragraph, the frequency response is symmetric with respect to the sign of the transverse mean-flow. Furthermore, for larger values of transverse mean-flow the response is clearly unstable.

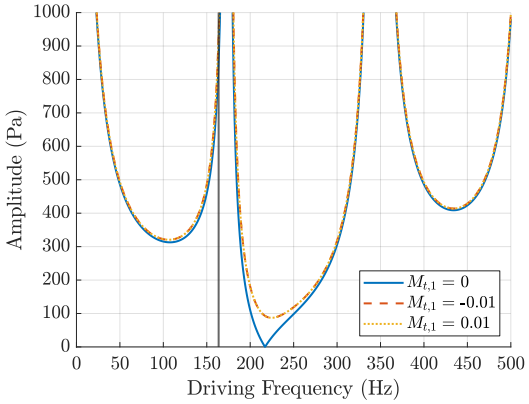

Figure 5.41: Frequency Response for Various Transverse Mean-Flows

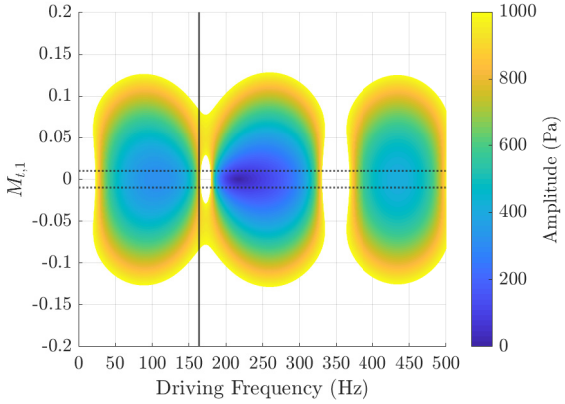

Figure 5.42: Frequency Response as a Function of Driving Frequency and Transverse Mean-Flow Mach Number in Sub-Duct 1

5.1.3d - Non-Zero Sub-Duct Temperature Difference

Figs. 5.43 – 5.46 show the effect of temperature difference on the mode shapes and frequency response. The pressure amplitude, Fig. 5.43, it appears that the temperature has had a damping effect. From the eigenfrequencies, it is known that the resonant frequencies increase with the

temperature. Therefore, the cases with a sub-duct temperature difference are being driven well below the resonant frequency and thus have a reduced response. The phase is also completely uniform in the entire duct with a sub-duct temperature difference.

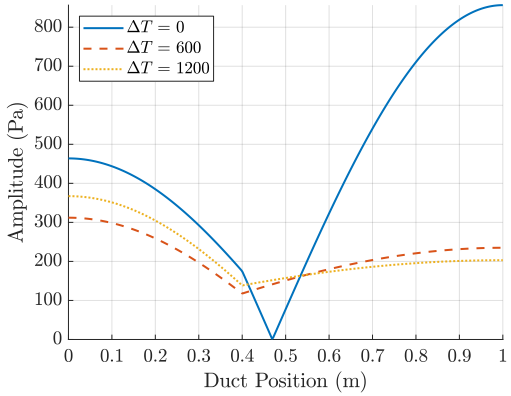

Figure 5.43: Pressure Amplitude as a Function of Duct Position for Various Sub-Duct Temperature Differences

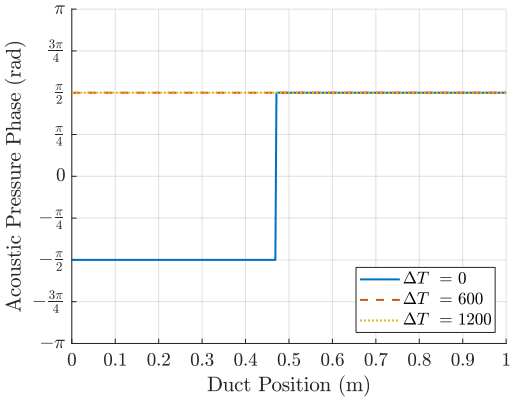

Figure 5.44: Pressure Phase as a Function of Duct Position for Various Sub-Duct Temperature Differences

The frequency response is plotted in Figs. 5.45 and 5.46. The dotted black lines in Fig. 5.46 indicate the temperature difference represented by the dashed red line and dotted yellow line in Figs. 5.43 – 5.45. The solid black line is, again, the location of the driving frequency use in previous plots. The unshaded parts are above the color scale, and therefore unfilled. The maximum of the color scale is the same as the maximum of the frequency response plot 5.45, i.e. 1000 Pa.

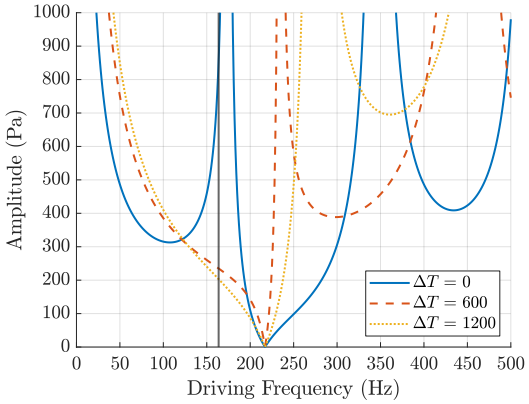

Figure 5.45: Frequency Response for Various Sub-Duct Temperature Differences

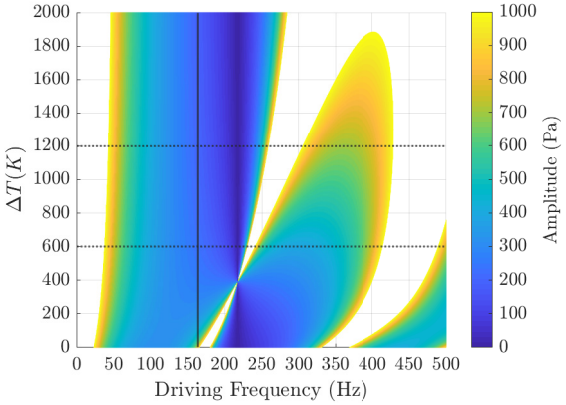

Figure 5.46: Frequency Response as a Function of Sub-Duct Temperature Difference

From the frequency response plot 5.45 an increasing temperature shifts the eigenfrequencies up as well as driving the system overall. Along with shifting the natural frequency of the duct up, increasing the sub-duct temperature difference increases the overall pressure magnitude response of the system. This makes intuitive sense, as the increase in temperature is increasing the energy in the system.

5.1.3e - Combination of Parameters

Now each effect is layered on top of one another. The added parameters are detailed in table 5.3:

Added Transverse Impedances	$\mathcal{Z} = 100 + 100i$ $(176.86+176.86i)$
Added Transverse Mean-Flows	$M_{t,1} = -0.01, M_{t,2} = 0.0067, (M_{t,2} = 0.0012)$
Added Sub-Duct Temperature Difference	$\Delta T = 600K$

Table 5.3: Layering Parameters

The parameters in parenthesis refer to parameters in sub-duct 2 with the sub-duct temperature in place. All transverse wall impedances are assumed to be equal, and the transverse wall mean-flows are equal in each duct. The layering results without temperature are shown in Figs. 5.47, 5.48, and 5.51. The layering results with temperature are shown in Figs. 5.49, 5.50, and 5.52. Figs. 5.47 and 5.49 show the pressure amplitude as a function of axial duct position without and with a sub-duct temperature difference, respectively. Figs. 5.48 and 5.50 show the pressure phase, without and with a sub-duct temperature difference, respectively.

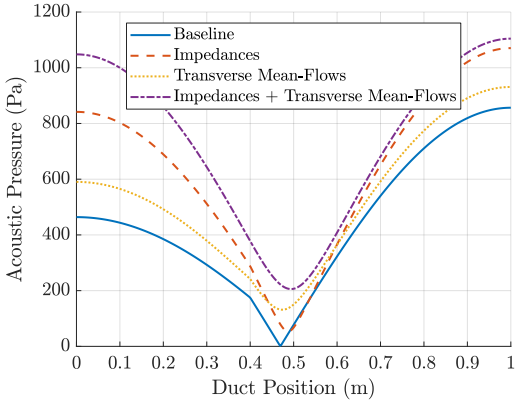

Figure 5.47: Pressure Mode Shapes for (a) Baseline, (b) Transverse Impedances, (c) Transverse Mean-Flows, (d) Transverse Impedances + Mean-Flows

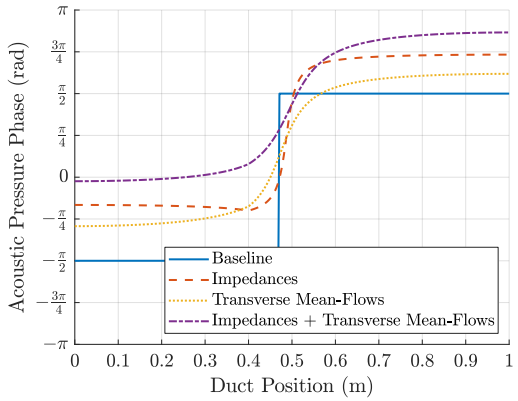

Figure 5.48: Pressure Phase Shapes for (a) Baseline, (b) Transverse Impedances, (c) Transverse Mean-Flows, (d) Transverse Impedances + Mean-Flows

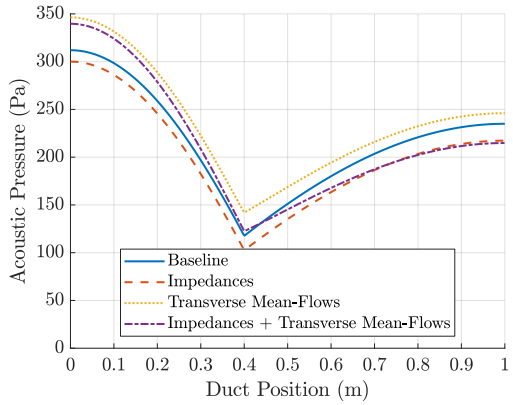

Figure 5.49: Pressure Mode Shapes with a Sub-Duct Temperature Difference of 600K for (a) Baseline, (b) Transverse Impedances, (c) Transverse Mean-Flows, (d) Transverse Impedances + Mean-Flows

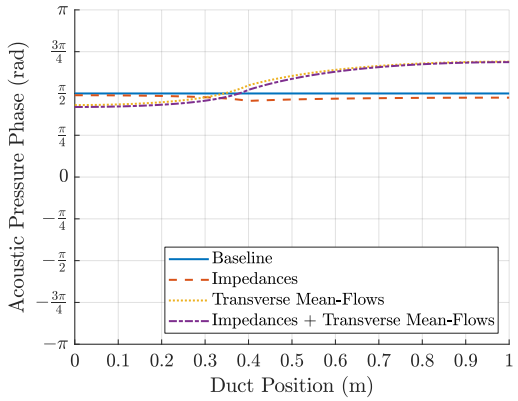

Figure 5.50: Pressure Phase Shapes with a Sub-Duct Temperature Difference of 600K for (a) Baseline, (b) Transverse Impedances, (c) Transverse Mean-Flows, (d) Transverse Impedances + Mean-Flows

Consider Figs. 5.47 and 5.49. The effect of impedance is to damp the system and shift the frequency, as discussed in previous sections. The transverse mean-flow appears to mostly drive the system a certain amount. The main effect of the sub-duct temperature difference appears to be damping from these two figures.

Consider Figs. 5.48 and 5.50. With no temperature difference, there is a large phase shift when the pressure amplitude is at a minimum in the duct. The driving frequency is close to the first resonant mode of all the various cases shown in Fig. 5.48. Temperature has a huge effect on the pressure phase. There is no large phase shift when the pressure is a minimum. This is most likely due to the

system being driven far below the first mode. The addition of temperature increases the resonant frequency by around 100 Hz. The addition of has a more significant effect on the phase than the addition of a finite wall impedance.

Figs. 5.51 and 5.52 show the frequency responses without and with sub-duct temperature differences, respectively.

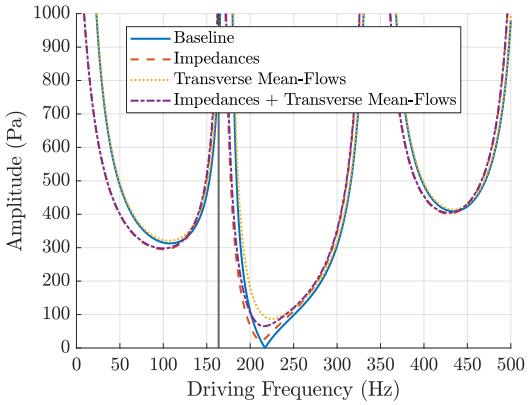

Figure 5.51: Frequency Response for (a) Baseline, (b) Transverse Impedances, (c) Transverse Mean-Flows, (d) Transverse Impedances + Mean-Flows

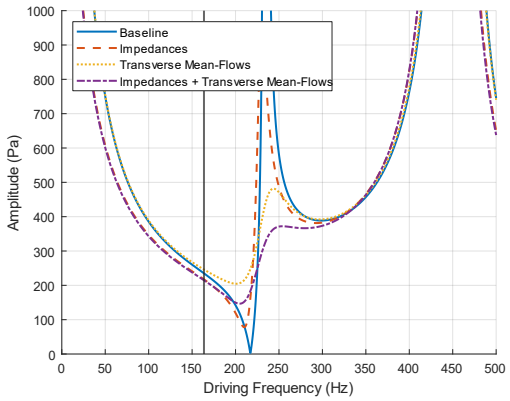

Figure 5.52: Frequency Response with a Sub-Duct Temperature Difference of 600K for (a) Baseline, (b) Transverse Impedances, (c) Transverse Mean-Flows, (d) Transverse Impedances + Mean-Flows

With no temperature, the effects of the parameters are not pronounced. It is difficult to tell each of the curves apart, except for the anti-resonance around 215 Hz. With a sub-duct temperature difference, the curves are much more easily distinguished, particularly around the first resonant frequency. The first resonant frequency is shifted up in frequency and damped by both the transverse impedances and transverse mean-flows. The second harmonic does not appear to be significantly affected by these parameters.

5.2 - Mass Flow Rate – Nozzle Duct

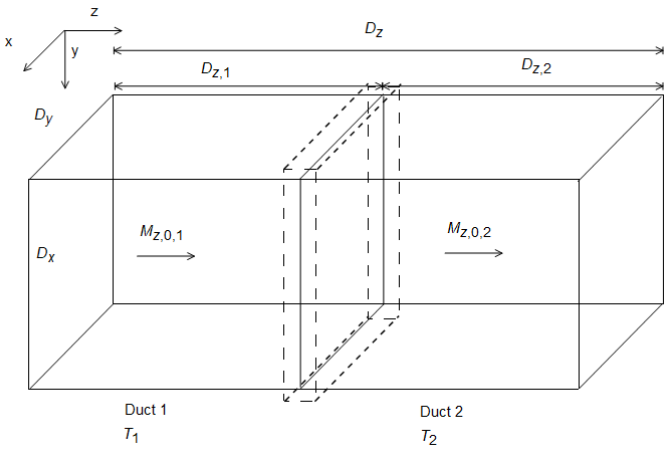

Figure 5.53: Mass Flow Rate - Nozzle Duct Configuration

5.2.1 - Problem Setup

Consider the duct shown in Fig. 5.53. As with the closed-closed problem, the dotted box outline indicates the control volume in which conservation of mass and momentum will be carried out. In the mass flow-rate – nozzle case, axial mean-flow is present and no simplifications of the CVA parameters is necessary. As the name of the problem suggests, the boundary conditions of the duct are that of a constant mass flow rate at $z = 0$ and a choked nozzle boundary condition at $z = D_z$. These two boundary conditions are given by equations (2.3.8) and (2.3.10). As with the closed-closed problem, the matching conditions are derived through the conservation of mass and momentum. For conservation of mass, equation (3.1.1) is used. Again, the first term in equation (3.1.1) goes to zero since an infinitesimal sliver of the control volume around the interface of the two sub-ducts is being considered. The second term is carried out for each control surface. The volume velocity is again assumed to be inserted through the transverse surfaces of the control volume in Fig. 5.53. Rather than consider each 4 transverse control surfaces separately, a single aggregate control surface is considered, denoted with the number 3. The analysis remains the same

until reaching equation (5.1.5). Instead of removing terms with mean-flows present, they are retained. Inserting the definitions of pressure and velocity into equation (5.1.5) one obtains:

$$\begin{aligned}&\left(-\Upsilon_1^+ - M_{z,0,1}\right)\frac{S_1}{a_{0,1}}e^{+ik_{z,1}^+ D_{z,1}}\mathrm{A}_1 + \left(\Upsilon_1^- - M_{z,0,1}\right)\frac{S_1}{a_{0,1}}e^{-ik_{z,1}^- D_{z,1}}\mathrm{B}_1 \\ &+\left(\Upsilon_2^+ + M_{z,0,2}\right)\frac{S_2}{a_{0,2}}\mathrm{A}_2 + \left(-\Upsilon_2^- + M_{z,0,2}\right)\frac{S_2}{a_{0,2}}\mathrm{B}_2 = \rho_{0,3}U_3{}'\end{aligned} \tag{5.2.1}$$

Equation (5.2.1) is the conservation of mass matching condition used in the mass flow rate-nozzle problem. As with conservation of mass, conservation of momentum begins at equation (5.1.9). Inserting the definitions of pressure and velocity and simplifying one obtains:

$$\begin{aligned}&-\left(M_{z,0,1}^2 + 2M_{z,0,1}\Upsilon_1^+ + 1\right)S_1 e^{+ik_{z,1}^+ D_{z,1}}\mathrm{A}_1 - \left(M_{z,0,1}^2 - 2M_{z,0,1}\Upsilon_1^- + 1\right)S_1 e^{-ik_{z,1}^- D_{z,1}}\mathrm{B}_1 \\ &+\left(M_{z,0,2}^2 + 2M_{z,0,2}\Upsilon_2^+ + 1\right)S_2\mathrm{A}_2 + \left(M_{z,0,2}^2 - 2M_{z,0,2}\Upsilon_2^- + 1\right)S_2\mathrm{B}_2 = 0\end{aligned} \tag{5.2.2}$$

Equation (5.2.2) is the conservation of momentum matching condition used in this problem. Moving on to the end boundary conditions, first consider the mass flow rate condition, equation (2.3.8). Combining equations (2.3.8) and (5.0.1) yields

$$\left(\Upsilon_1^+ + M_{z,0,1}\right)\mathrm{A}_1 - \left(\Upsilon_1^- - M_{z,0,1}\right)\mathrm{B}_1 = 0 \tag{5.2.3}$$

For the choked nozzle condition one simply inserts the definitions of pressure and velocity into the boundary condition (2.3.8) to obtain:

$$\left(M_{z,0,2}\gamma_2(\gamma_2 - 1) - 2\Upsilon_2^+\right)e^{+ik_{z,2}^+ D_{z,2}}\mathrm{A}_2 + \left(M_{z,0,2}\gamma_2(\gamma_2 - 1) + 2\Upsilon_2^-\right)e^{-ik_{z,2}^- D_{z,2}}\mathrm{B}_2 = 0 \tag{5.2.4}$$

Combining equations (5.2.1), (5.2.2), (5.2.3), and (5.2.4) into one matrix equation produces:

$$\begin{bmatrix} \left(\Upsilon_1^+ + M_{z,0,1}\right) & -\left(\Upsilon_1^- - M_{z,0,1}\right) \\ 0 & 0 \\ \left(-\Upsilon_1^+ - M_{z,0,1}\right)\dfrac{S_1}{a_{0,1}} e^{+ik_{z,1}^+ D_{z,1}} & \left(\Upsilon_1^- - M_{z,0,1}\right)\dfrac{S_1}{a_{0,1}} e^{-ik_{z,1}^- D_{z,1}} \quad \cdots \\ -\left(M_{z,0,1}^2 + 2M_{z,0,1}\Upsilon_1^+ + 1\right) S_1 e^{+ik_{z,1}^+ D_{z,1}} & -\left(M_{z,0,1}^2 - 2M_{z,0,1}\Upsilon_1^- + 1\right) S_1 e^{-ik_{z,1}^- D_{z,1}} \\ 0 & 0 \\ \left(M_{z,0,2}\gamma_2(\gamma_2 - 1) - 2\Upsilon_2^+\right) e^{+ik_{z,2}^+ D_{z,2}} & \left(M_{z,0,2}\gamma_2(\gamma_2 - 1) + 2\Upsilon_2^-\right) e^{-ik_{z,2}^- D_{z,2}} \\ \left(\Upsilon_2^+ + M_{z,0,2}\right)\dfrac{S_2}{a_{0,2}} & \left(-\Upsilon_2^- + M_{z,0,2}\right)\dfrac{S_2}{a_{0,2}} \\ \left(M_{z,0,2}^2 + 2M_{z,0,2}\Upsilon_2^+ + 1\right) S_2 & \left(M_{z,0,2}^2 - 2M_{z,0,2}\Upsilon_2^- + 1\right) S_2 \end{bmatrix} \begin{bmatrix} \mathrm{A}_1 \\ \mathrm{B}_1 \\ \mathrm{A}_2 \\ \mathrm{B}_2 \end{bmatrix} = \begin{bmatrix} 0 \\ 0 \\ \rho_{0,3} U_3' \\ 0 \end{bmatrix} \tag{5.2.5}$$

To calculate the eigenfrequencies the determinant of the 4x4 matrix in equation (5.2.5) is taken and the resulting non-linear equation is set equal to zero. To calculate the coefficients, one simply solves the matrix equation (5.2.5). The solution to the coefficients is analytical and too large to be included here. The solutions in their full form are not included in this work due to their extreme length.

5.2.2 - Eigenfrequencies

5.2.2a - Baseline Solution

A baseline eigenfrequency is established by 'turning off' each variable from the CVA. ξ_Z, ξ_M, and ΔT are set to zero. The relevant CVA quantities become:

$$\begin{aligned} k_{z,1}^{\pm} &= k_{z,2}^{\pm} = \frac{k_0}{1 \pm M_{z,0}} \\ \Upsilon_1^{\pm} &= \Upsilon_2^{\pm} = \Upsilon^{\pm} = 1 \end{aligned} \tag{5.2.6}$$

The problem is now that of a single duct. Care must be taken when converting from z_1 and z_2 to z (see equation (5.1.16)). If the sub-duct temperatures are the same the governing matrix reduces to:

$$\begin{bmatrix} \left(\Upsilon^{+}+M_{z,0}\right) & -\left(\Upsilon^{-}-M_{z,0}\right) \\ \left(M_{z,0}\gamma(\gamma-1)-2\Upsilon^{+}\right)e^{+ik_z^{+}D_z} & \left(M_{z,0}\gamma(\gamma-1)+2\Upsilon^{-}\right)e^{-ik_z^{-}D_z} \end{bmatrix} \tag{5.2.7}$$

Unlike the closed-closed problem, the presence of mean-flow prevents further simplification for all cases in which the sub-duct temperature difference is 0. However, substituting equations (5.2.6) into (5.2.7) yields:

$$\begin{bmatrix} \left(1+M_{z,0}\right) & -\left(1-M_{z,0}\right) \\ \left(M_{z,0}\gamma(\gamma-1)-2\right)e^{+ik_0D_z/(1+M_{z,0})} & \left(M_{z,0}\gamma(\gamma-1)+2\right)e^{-ik_0D_z/(1-M_{z,0})} \end{bmatrix} \tag{5.2.8}$$

Taking the determinant of (5.2.8) and setting the resulting expression equal to zero yields:

$$e^{+\frac{2ik_0D_z}{1-M_{z,0}^2}} = -\frac{\left(1+M_{z,0}\right)\left(M_{z,0}\gamma(\gamma-1)+2\right)}{\left(1-M_{z,0}\right)\left(M_{z,0}\gamma(\gamma-1)-2\right)} \tag{5.2.9}$$

An analytical solution to equation (5.2.9) is possible by splitting the wave-number into imaginary and real parts.

$$e^{+\frac{2ik_{0,r}D_z}{1-M_{z,0}^2}}e^{-\frac{2k_{0,i}D_z}{1-M_{z,0}^2}} = -\frac{\left(1+M_{z,0}\right)\left(M_{z,0}\gamma(\gamma-1)+2\right)}{\left(1-M_{z,0}\right)\left(M_{z,0}\gamma(\gamma-1)-2\right)} \tag{5.2.10}$$

One can then use Euler's formula to split the first term on the LHS into real and imaginary parts:

$$\left(\cos\left(\frac{2k_{0,r}D_z}{1-M_{z,0}^2}\right)+i\sin\left(\frac{2k_{0,r}D_z}{1-M_{z,0}^2}\right)\right)e^{-\frac{2k_{0,i}D_z}{1-M_{z,0}^2}} = -\frac{\left(1+M_{z,0}\right)\left(M_{z,0}\gamma(\gamma-1)+2\right)}{\left(1-M_{z,0}\right)\left(M_{z,0}\gamma(\gamma-1)-2\right)} \tag{5.2.11}$$

Equation (5.2.11) can be separated into real and imaginary parts to form the two equations

$$\begin{aligned}\cos\left(\frac{2k_{0,r}D_z}{1-M_{z,0}^2}\right)e^{-\frac{2k_{0,i}D_z}{1-M_{z,0}^2}} &= -\frac{\left(1+M_{z,0}\right)\left(M_{z,0}\gamma(\gamma-1)+2\right)}{\left(1-M_{z,0}\right)\left(M_{z,0}\gamma(\gamma-1)-2\right)}\\ \sin\left(\frac{2k_{0,r}D_z}{1-M_{z,0}^2}\right)e^{-\frac{2k_{0,i}D_z}{1-M_{z,0}^2}} &= 0\end{aligned} \tag{5.2.12}$$

Beginning with the latter equation two solutions are possible.

$$\begin{aligned}k_{0,i} &= \infty\\ k_{0,r} &= \frac{\left(1-M_{z,0}^2\right)n\pi}{2D_z},\ n\in\mathbb{Z}\end{aligned} \tag{5.2.13}$$

The latter solution is, of course, preferable and useful. Plugging that solution back into equation (5.2.12) yields

$$k_{0,i} = -\frac{\left(1-M_{z,0}^2\right)}{2D_z}\left(\log\left((-1)^n\right)+\log\left(\frac{(1+M_{z,0})(2+M_{z,0}\gamma(\gamma-1))}{(1-M_{z,0})(2-M_{z,0}\gamma(\gamma-1))}\right)\right) \tag{5.2.14}$$

where n is the same as in equation (5.2.13). This presents a problem. $\log\left((-1)^n\right)$ can talk on two values: 0 or $i\pi$, for even and odd values, respectively. Thus, n is restricted to even values only, since $k_{0,i}$ is defined such that it is real. Thus, the wavenumber is:

$$k_0 = \frac{1-M_{z,0}^2}{2D_z}\left(2n\pi - i\log\left(\frac{(1+M_{z,0})(2+M_{z,0}\gamma(\gamma-1))}{(1-M_{z,0})(2-M_{z,0}\gamma(\gamma-1))}\right)\right),\ n\in\mathbb{Z} \tag{5.2.15}$$

The full solution for the frequency is

$$f = \frac{a_0\left(1-M_{z,0}^2\right)}{4\pi D_z}\left(2n\pi - i\log\left(\frac{(M_{z,0}+1)(M_{z,0}\gamma(\gamma-1)+2)}{(M_{z,0}-1)(M_{z,0}\gamma(\gamma-1)-2)}\right)\right) \tag{5.2.16}$$

Equation (5.2.16) is the analytical solution for the baseline case for the m-dot-nozzle problem. A solution analogous to (5.2.16) is possible as long as $\Upsilon \neq \Upsilon(f)$. For such cases, the analytical solution for the eigenfrequency will be shown. As a sanity check, setting the axial mean-flow Mach number to zero yields equation (5.1.21), as expected. Negative axial flow is not allowed as the nozzle boundary condition is not valid reverse direction axial mean-flow. Such a mean-flow would result in a negative acoustic resistance being imposed at the duct outlet, which is not possible.

The baseline fundamental eigenfrequency is plotted as a function of $M_{z,0}$ in Figs. 5.54 and 5.55. Fig 5.54 shows that as the axial mean-flow is increased, the natural frequency of the system decreases to zero for when the mean-flow is sonic. Fig. 5.55 shows that the temporal damping of the system increases as the axial mean-flow increases. This continues until a Mach number of around 0.63. Further increases to the axial mean-flow reduces the acoustic temporal damping until it becomes 0 when the mean-flow is sonic.

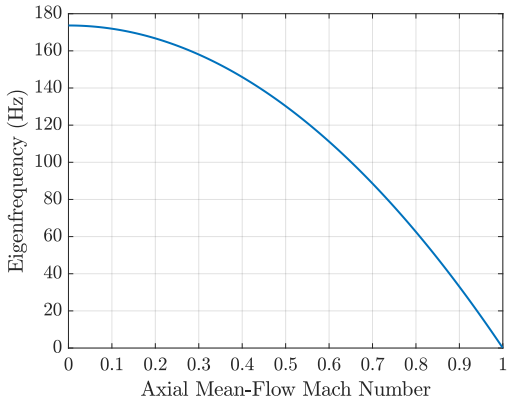

Figure 5.54: Real Part of the Eigenfrequency as a Function of Axial Mean-Flow

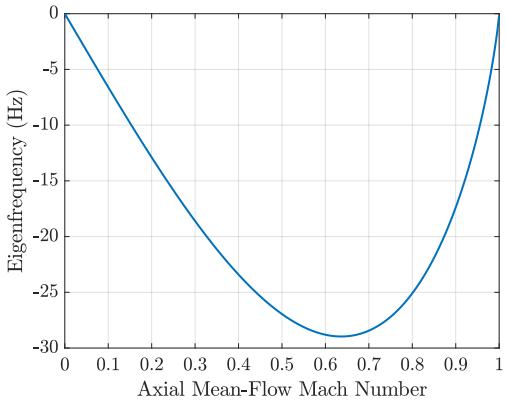

Figure 5.55: Imaginary Part of the Eigenfrequency as a Function of Axial Mean-Flow

5.2.2b - Finite Transverse Wall Impedances

Consider transverse walls with a finite impedance. The relevant CVA properties are

$$k_z^{\pm} \to \frac{k_0\sqrt{1+i\xi_Z/k_0}}{1\pm M_{z,0}\sqrt{1+i\xi_Z/k_0}}$$
$$\Upsilon^{\pm} \to \Upsilon = \sqrt{1+i\frac{\xi_Z}{k_0}} \tag{5.2.17}$$

From equation (5.2.17) it is obvious that Υ is still a function of the eigenfrequency, therefore the equation resulting from the matrix (5.2.8) is non-linear, and does not permit an analytical solution. The solution is obtained numerically.

First consider purely resistive wall impedances. Figs. 5.56 and 5.57 show the fundamental frequency for increasing axial mean-flows. The same information is also shown in Figs. 5.58 and 5.59. Figs 5.58 and 5.59 are in the style of Figs. 5.54 and 5.55. This style of plot will be used for the remainder of the section.

In Fig. 5.56, the frequency doesn't change appreciably until the transverse impedances are less than 100. For values greater than this, the frequencies approach the values predicted in equation (5.2.16), as expected. Only at high Mach numbers does the curve alter shape significantly. The frequency increases slightly, then decreases to zero at about the same impedance value as the baseline. Indeed, the cut-off impedance is largely unaffected by axial mean-flow. Next consider the imaginary part of the eigenfrequency, Fig. 5.57. The addition of axial mean-flow serves to increase the damping in the system.

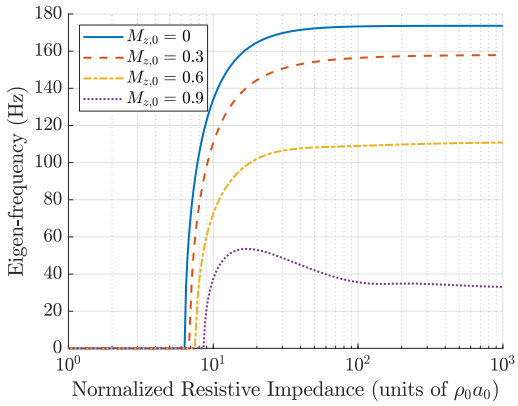

Figure 5.56: Real Part of the Eigenfrequency as a Function of Purely Resistive Impedance for Positive Axial Mach Numbers

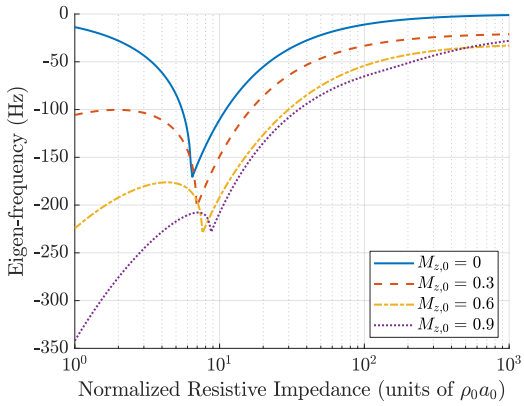

Figure 5.57: Imaginary Part of the Eigenfrequency as a Function of Purely Resistive Impedance for Positive Axial Mach Numbers

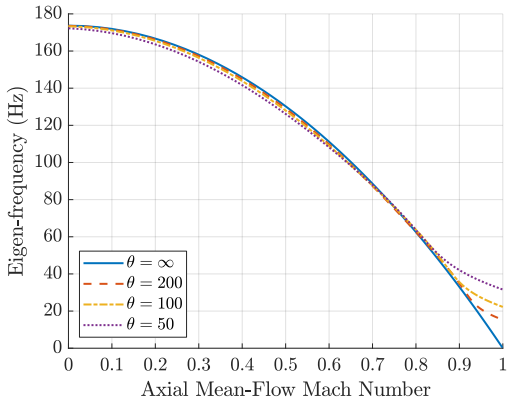

Figure 5.58: Real Part of the Fundamental Eigenfrequency as a Function of Axial Mean-Flow for Various Complex Impedances

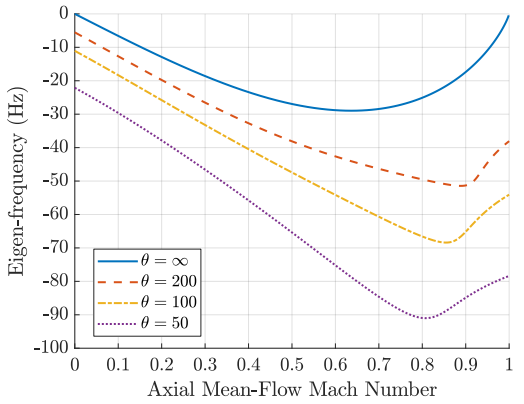

Figure 5.59: Imaginary Part of the Fundamental Eigenfrequency as a Function of Axial Mean-Flow for Various Complex Impedances

Figs. 5.58 and 5.59 show the real and imaginary components of the fundamental eigenfrequency as a function of axial mean-flow Mach number for various resistive impedances. The frequency, Fig. 5.58, remains largely unaffected by the resistive transverse impedances for axial mean-flow Mach numbers of 0 to 0.8. Beyond this region the frequency is significantly affected by the axial mean-flow. The damping/driving, Fig. 5.59, shows a much greater dependence on the transverse impedances. Indeed, the system experiences more and more temporal damping as the transverse walls become less rigid. For small transverse wall impedances, the system is temporally damped for all values of the axial mean-flow.

Now consider purely reactive transverse wall impedances. Figs. 5.60 and 5.61 show the real and imaginary parts of the eigenfrequency as a function of axial mean-flow Mach number.

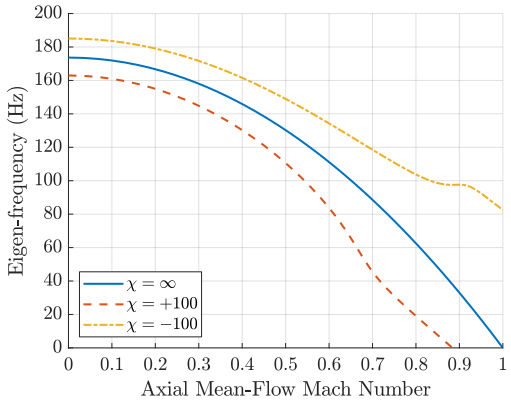

Figure 5.60: Real Part of the Fundamental Eigenfrequency as a Function of Axial Mean-Flow for Various Reactive Impedances

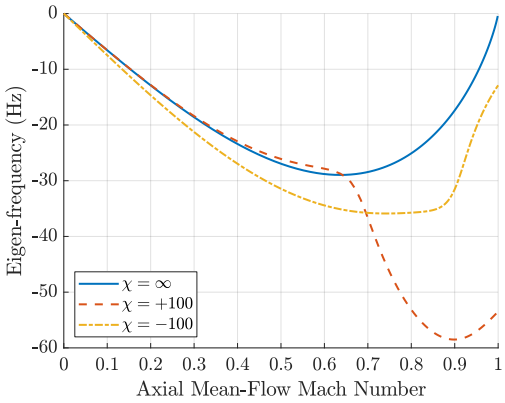

Figure 5.61: Imaginary Part of the Fundamental Eigenfrequency as a Function of Axial Mean-Flow for Various Reactive Impedances

From Fig. 5.60, the frequency is shifted by the presence of reactive transverse impedances. This behavior is largely unaffected by the axial mean-flow until mean-flow Mach numbers greater than 0.5. Similarly, reactive wall impedances do not significantly affect the temporal damping in the system until larger values of axial mean-flow. This is a significant deviation from the case with no axial mean-flow, as reactive impedances did not affect the temporal damping/driving at all. For large axial mean-flow Mach numbers, reactive wall impedances make a huge difference. Furthermore, the effect of the sign of the reactive impedance not only determines the direction of the frequency shifting but also the overall shape of the damping curve in Fig. 5.61. For realistic values of axial mean-flow Mach number (i.e. below 0.4), reactive impedances do not make a significant contribution to the temporal damping/driving of the system. Furthermore, the coupling between the axial mean-flow and reactive impedance can be neglected.

Finally, consider fully complex transverse impedances. Figs. 5.62 and 5.63 are the same as Figs. 5.60 and 5.61, but with complex impedance values.

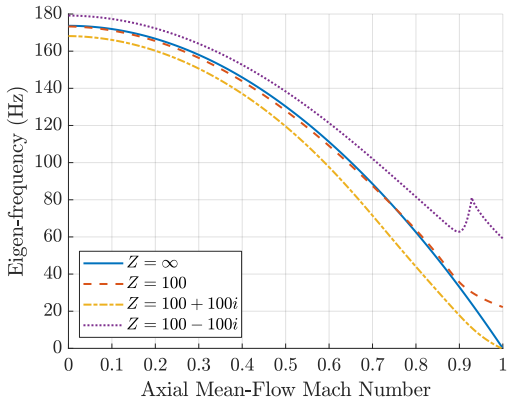

Figure 5.62: Real Part of the Fundamental Eigenfrequency as a Function of Axial Mean-Flow for Various Complex Impedances

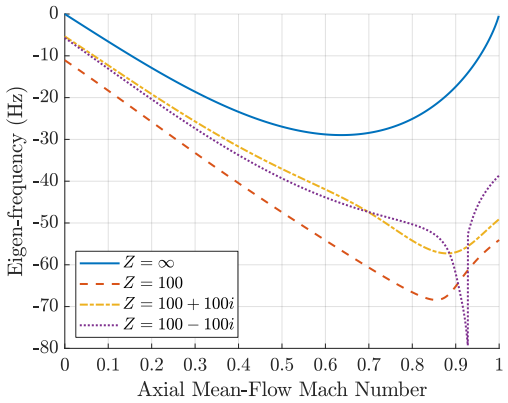

Figure 5.63: Imaginary Part of the Fundamental Eigenfrequency as a Function of Axial Mean-Flow for Various Complex Impedances

The combination of resistive impedance, reactive impedance, and axial mean-flow are encapsulated in Figs. 5.62 and 5.63. For realistic mean-flow Mach numbers, the coupling between axial mean-flow and transverse impedances can largely be neglected. That is, merely considering the effects of axial mean-flow and transverse impedances separately and summing the two effects is sufficient. For higher mean-flow Mach numbers, the coupling comes into play. For this regime, the case must be considered alone, as general trends are hard to come by.

5.2.2c - Non-Zero Transverse Wall Mean-Flows

As with the closed-closed duct problem, continuity must be observed in the duct. Equation (5.1.33) applies to the m-dot-nozzle problem just the same, forcing the duct to be bisected into sub-ducts. The relevant CVA parameters are

$$k_z^{\pm} \to \frac{k_0 + i\xi_M}{1 \pm M_{z,0}} \qquad (5.2.18)$$
$$\Upsilon^{\pm} \to \Upsilon = 1$$

If it wasn't necessary to subdivide the duct, this case would have an analytical solution, since $\Upsilon = 1$. When considering transverse mean-flow with two sub-ducts, there are now 3 distinct scenarios: balanced transverse mean-flow, constant transverse mean-flow, or a general case. In

each case the mean-flow entering sub-duct 1 through the $z = 0$ boundary is considered fixed. This leaves 3 unknowns in equation (5.1.33): the two transverse mean-flow parameters ($\xi_{M,1}$ and $\xi_{M,2}$) and the axial mean-flow in sub-duct 2. In this section, the transverse mean-flow parameters are being investigated and therefore will be treated as known. Therefore it is a simple matter to solve equation (5.1.33) for $M_{z,0,2}$, i.e.

$$M_{z,0,2}\left(\hat{n}_v \cdot \hat{n}\right)_{z_2=D_z} = -\frac{\rho_{0,1}a_{0,1}}{\rho_{0,2}a_{0,2}}\left(-M_{z,0,1} + D_{z,1}\xi_{M,1}\right) - D_{z,2}\xi_{M,2} \tag{5.2.19}$$

Note the dot-product for the axial mean-flow in sub-duct 1 has been carried out. It is assumed that the mean-flow is travelling in the $+z$ direction, therefore the dot-product amounts to a minus sign. Thus, the sign on the RHS determines the value of the remaining dot product. In this section the gas properties in each sub-duct are equal, thus

$$M_{z,0,2}\left(\hat{n}_v \cdot \hat{n}\right)_{z_2=D_z} = -\left(-M_{z,0,1} + D_{z,1}\xi_{M,1}\right) - D_{z,2}\xi_{M,2} \tag{5.2.20}$$

One must take care when using Mach numbers due to the dependence on sound speed and therefore temperature. Thus, the following analysis applies only to situations in which all sub-ducts have the same temperature. If the sub-ducts have different temperatures then one can simply re-derive these expressions in terms of the transverse velocities, rather than the impedance parameters.

The first scenario balanced transverse mean-flows. In other words, the transverse mean flows are chosen such that they have no effect on the axial mean-flow. In this case the dot product is evaluated to +1 and equation (5.2.20) leads to

$$D_{z,1}\xi_{M,1} = -D_{z,2}\xi_{M,2} \tag{5.2.21}$$

Thus, all the mean-flow coming in through the side walls in a sub-duct will leave through the sidewalls in the second sub-duct. This was the only case with transverse mean-flow allowed in the closed – closed problem.

Scenario two is where the transverse mean-flows are constant throughout the entire duct. If the mean-flow is entering the duct through the side walls, $M_{z,0,2}$ will increase. This analysis is valid for Mach numbers below 1, which gives a hard limit to the amount of transverse mean-flow allowed to enter, i.e. $M_{z,0,2} = \pm 1$. Assuming the mean-flow entering each sub-duct is equal, the axial mean-flow at the outlet is ± 1 equation (5.2.20) becomes

$$\xi_M = \frac{M_{z,0,1} \mp 1}{D_z} \tag{5.2.22}$$

If the mean-flow is leaving the duct through the side walls, $M_{z,0,2}$ will decrease. Once $M_{z,0,2}$ becomes equal to zero the usefulness of this scenario ends, since material entering through the exhaust of a combustor is hardly a desirable feature. Nevertheless, the analysis is valid until the axial mean-flow in sub-duct 2 is equal to -1, as indicated in equation (5.2.22). If the axial mean-flow is zero one has

$$\xi_M = \frac{M_{z,0,1}}{D_z} \tag{5.2.23}$$

The third and final scenario is un-balanced transverse mean-flow, i.e. the transverse mean-flow in each sub-duct is different. This scenario is truly general and offers the most flexibility for application to a given problem.

First consider balanced transverse mean-flow. An analytical solution is possible. It is

$$f = \frac{a_0\left(1-M_{z,0}^2\right)}{2\pi D_z}\left(n\pi - \frac{i}{2}\log\left(\frac{(M_{z,0}+1)(M_{z,0}(\gamma-1)+2)}{(M_{z,0}-1)(M_{z,0}(\gamma-1)-2)}\right)\right) - i\frac{a_0(D_{z,1}\xi_{M,1}+D_{z,2}\xi_{M,2})}{2\pi D_z} \tag{5.2.24}$$

If one inserts equation (5.2.21) into equation (5.2.24) one obtains equation (5.2.16). Thus, if the transverse mean-flow is balanced then the transverse mean-flows *cannot* affect the eigenfrequency under the current assumptions.

Next consider scenario two, in which the transverse mean-flows are equal in both ducts. From equations (5.2.22) and (5.2.23) the limits on the transverse mean-flow change with the inlet mean-flow Mach number $M_{z,0,1}$. Assuming that the transverse mean-flows are equal in each sub-duct wall, equations (5.2.22) and (5.2.23) can be re-arranged to:

$$\begin{aligned} M_{z,0,1} &= 2M_t D_z \frac{D_x + D_y}{D_x D_y} \pm 1 \\ M_{z,0,1} &= 2M_t D_z \frac{D_x + D_y}{D_x D_y} \end{aligned} \tag{5.2.25}$$

Equations (5.2.25) facilitates the creation of figures in which the limits on $M_{z,0,1}$ vary.

If the axial mean-flow is fixed and the transverse mean-flows are variable, equations (5.2.25) can be rearranged to

$$\begin{aligned} M_t &= \frac{M_{z,0,1} \mp 1}{2D_z}\frac{D_x D_y}{D_x + D_y} \\ M_t &= \frac{M_{z,0,1}}{2D_z}\frac{D_x D_y}{D_x + D_y} \end{aligned} \tag{5.2.26}$$

Thus, the limits on the transverse mean-flow are the inlet mean-flow, assumed to be known *a priori*, and the duct dimensions. The form of equations (5.2.26) is that of a line, with the inlet axial mean-flow varying from -1 to 1. Using the duct dimensions laid out in table 5.1, the extremum of equations (5.2.26) are (-0.05, 0), (-0.025, 0.025), (0, 0.05). Thus, the available values of the transverse mean-flow Mach numbers are from -0.05 to 0.05.

Figs. 5.64 and 5.65 show the real and imaginary parts of the eigenfrequency as a function of the axial mean-flow in sub-duct 1 for various constant transverse mean-flows. Consider the vertical lines. The dashed lines correspond to the $M_t = -0.01$ case and the dashed-dotted lines correspond to the $M_t = +0.01$. They are also color coded to those same cases. The positions of these lines are given by equations (5.2.25). For the $M_t = -0.01$ case, the dashed vertical line corresponds to the value of $M_{z,0,1}$ for which $M_{z,0,2} = 1$. Thus, the region to the left of this vertical line is not valid for this analysis, as the axial mean-flow in sub-duct 2 is supersonic. Therefore, the nozzle boundary condition is invalid. For the $M_t = +0.01$ case, the dashed-dotted vertical line corresponds to the value of $M_{z,0,1}$ for which $M_{z,0,2} = 0$. Thus, the region to the left of this vertical line is not valid for this analysis as the axial mean-flow in sub-duct 2 is negative. Therefore, the nozzle boundary condition is invalid.

Consider the case with no transverse mean-flow, i.e. the blue curve, as a starting point. At this point, the vertical dashed line is on the right edge of the graphs, at $M_{z,0,1} = 1$. Then the transverse mean-flow is slowly increased *into* the control volume. The dashed line moves to the left, and the curve is squished in the region between the dashed line and $M_{z,0,1} = 0$. If the transverse mean-flow is instead increased *out of* the control volume, the opposite occurs. In this case, the dashed-

dotted line starts at $M_{z,0,1}=0$ and moves to the right with increasing transverse mean-flow. In either case the domain, i.e. the acceptable values of $M_{z,0,1}$, is restricted. For the $M_t=-0.01$ case, the general trend is a decrease in the natural frequency, i.e. the blue curve in Fig. 5.64 is essentially shifted to the left. The opposite behavior is seen in the $M_t=+0.01$ case, where the transverse mean-flow is leaving the duct. Essentially the same curve-shifting is seen in Fig. 5.65. An important difference is for the $M_t=-0.01$ case, for large axial mean-flows in sub-duct 1, the system comes temporally driven rather than temporally damped.

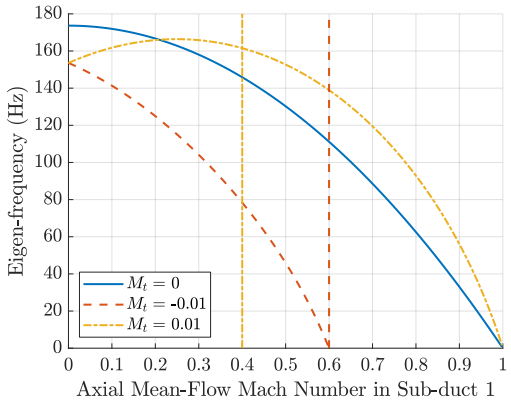

Figure 5.64: Real Part of the Fundamental Eigenfrequency as a Function of Axial Mean-Flow for Various Constant Transverse Mean-Flows

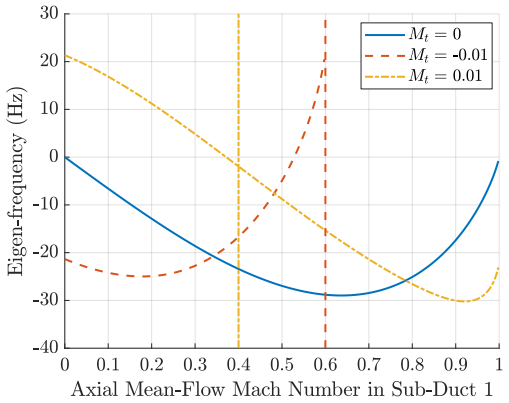

Figure 5.65: Imaginary Part of the Fundamental Eigenfrequency as a Function of Axial Mean-Flow for Various Constant Transverse Mean-Flows

Finally, consider a more general case. In combustors, there is often a secondary combustion zone in which bypass air can enter the combustor after the primary combustion zone. As a first pass at this situation, the transverse mean-flow in sub-duct 1 is set to 0, and the transverse mean-flow Mach number entering sub-duct two is set to a value of -0.01. The axial mean-flow Mach number in sub-duct 1 is set to be 0.01, and the axial mean-flow Mach number in sub-duct two is calculated to be 0.25 from equation (5.2.20). The calculated eigenfrequency for this case is (167.02 - 13.85i) Hz. Compared to the baseline value for this case, (173.64 – 0.64i) Hz, the eigenfrequency has changed significantly. The damping factor for these cases is $9.65\cdot10^{-7}$ and 0.515, respectively. The

introduction of transverse mean-flow likely contributed to the slight change in the frequency, but the increase in damping is mostly due to the increase in axial mean-flow. In order to dissect this idea, consider another case in which there is no transverse mean-flow, but the axial mean-flow is equal to the average axial mean-flow in the general case. The average axial mean-flow Mach number is +0.154, and the eigenfrequency for this case is (169.54 - 10.05i) Hz. If one considers transverse mean-flow alone, there is no effect on the eigenfrequencies. Thus, the axial mean-flow is indeed the main contributor to the temporal damping, but the transverse mean-flow also provides damping and shifts the frequency.

5.2.2d - Non-Zero Sub-Duct Temperature Difference

When considering sub-duct temperature differences, there no analytical solution. One must take care when calculating the axial mean-flow in sub-duct two, such that the Mach number never exceeds 1. Examining equation (5.2.19) reveals that if $\rho_{0,1}a_{0,1} \leq \rho_{0,2}a_{0,2}$, the axial Mach number in

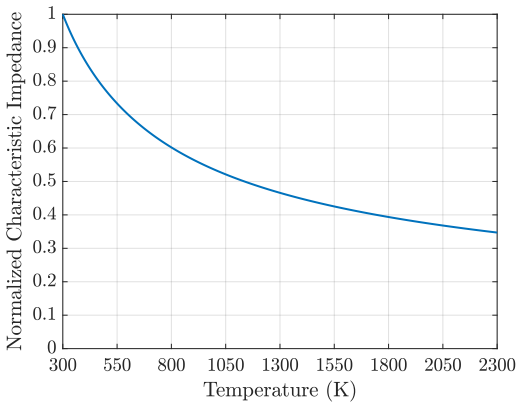

Figure 5.66: Characteristic Impedance of Air as a Function of Temperature at 1 atm

sub-duct two will never exceed the axial Mach-number in duct 1, and therefore will be less than 1.

Fig. 5.66 plots $\rho_0 a_0$, the characteristic impedance of air, as a function of temperature. The impedance is normalized to the characteristic impedance at 300 K. The sub-duct temperature

difference is, in this analysis, always such that the temperature in sub-duct two is greater than the temperature in sub-duct 1. Therefore, any temperature differences presented in this thesis could potentially cause the axial mean-flow Mach number in sub-duct two to become greater than 1. Re-arranging equation (5.2.19) by setting the transverse mean-flows to zero and setting the axial mean-flow in sub-duct two equal to one yields the limit for $M_{z,0,1}$

$$M_{z,0,1} = \frac{\rho_{0,2} a_{0,2}}{\rho_{0,1} a_{0,1}} \tag{5.2.27}$$

Astute readers may notice out that equation (5.2.27) is depicted in Fig. 5.66. Taking this limit into account, the fundamental eigenfrequency is plotted as a function of $M_{z,0,1}$ for sub-duct temperature differences of 0, 300, 600, and 900 Kelvins in Figs. 5.67 and 5.68. The limits on $M_{z,0,1}$ for these cases are 1, 0.70, 0.57, and 0.49, respectively.

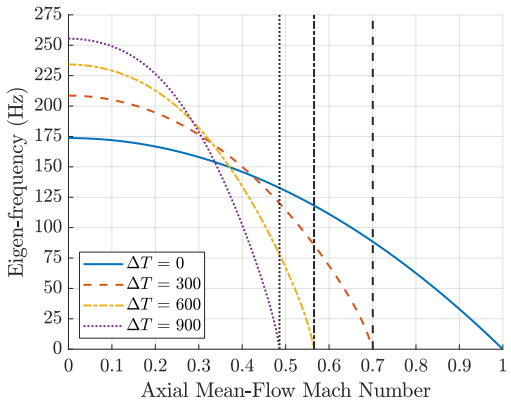

Figure 5.67: Real Part of the Fundamental Eigenfrequency as a Function of Axial Mean-Flow for Various Sub-Duct Temperature Differences

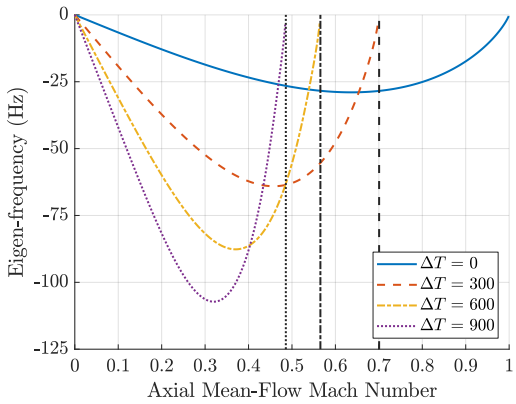

Figure 5.68: Imaginary Part of the Fundamental Eigenfrequency as a Function of Axial Mean-Flow for Various Sub-Duct Temperature Differences

Both Figs. 5.67 and 5.68 show the same behavior with increasing sub-duct temperature difference. The curve in each case is "squished" horizontally. The maxima in each figure is increased with the temperature difference. Thus, a sub-duct temperature difference only serves to enhance the effects of axial mean-flow in this case.

5.2.2e - Combination of Parameters

In section 5.2.2e each effect is layered on top of one another. The fundamental case is that depicted in Fig. 5.47. Next finite transverse mean-flows are added. These impedances are equal in both sub-duct 1 and sub-duct 2. Furthermore, the impedance value is chosen to be 100 + 100*i*, normalized to $\rho_0 a_0$ for air at the temperature in the duct.

One must carefully consider the effects of temperature when many parameters are in play. Previous sections discuss this but leave out 1 key effect: the effect of temperature on the transverse wall impedances. The transverse impedances presented are normalized in terms of the characteristic impedance of air, which is the density of air multiplied by the sound speed of air. Thus the normalized impedances are only locally normalized in each sub-duct. Thus, a normalized impedance of 100 in both sub-ducts can represent a different actual impedance in each sub-duct if the sub-ducts are at different temperatures. In order to account for this, the impedances must be scaled. Since the impedance in sub-duct 1 never changes temperature in this work (i.e. it's always 300 K), only the impedances in sub-duct two are scaled according to the following equation:

$$\mathcal{Z}_2 = \mathcal{Z}_1 \frac{\rho_1 a_{0,1}}{\rho_2 a_{0,2}} \tag{5.2.28}$$

Note that this is the inverse of the relation shown in Fig. 5.66. This means that if the temperature is higher in subduct 2 the normalized impedance in sub-duct 2 increases compared to the normalized impedance in sub-duct 1. For instance, a normalized impedance of 100 in sub-duct two would mean a normalized impedance of 176.86 if sub-duct 2 is at 900 K.

The parameters are added in the same order and manner as with the case with no sub-duct temperature difference. The added parameters are detailed in table 5.4:

Added Transverse Impedances	$\mathcal{Z} = 100 + 100i$ (176.86+176.86i)
Added Transverse Mean-Flows	$M_{t,1} = 0,\ M_{t,2} = -0.01$
Added Sub-Duct Temperature Difference	$\Delta T = 600K$

Table 5.4: Layering Parameters

Figs. 5.69 and 5.70 show the real and imaginary components of the fundamental eigenfrequency for each layering case with no sub-duct temperature difference. The vertical dashed line shows the point at which the axial mean-flow in sub-duct 2 becomes supersonic.

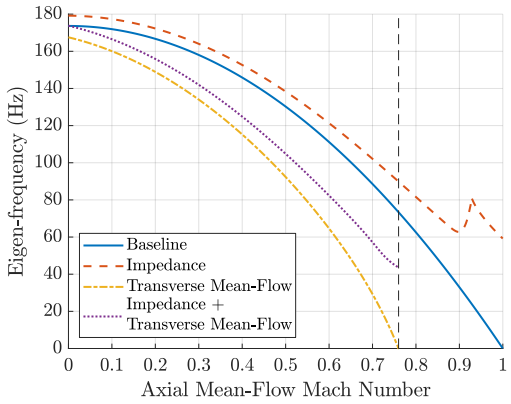

Figure 5.69: Real Part of the Fundamental Eigenfrequency as a Function of Axial Mean-Flow for (a) Baseline, (b) Transverse Impedances, (c) Transverse Mean-Flows, (d) Transverse Impedances + Mean-Flows

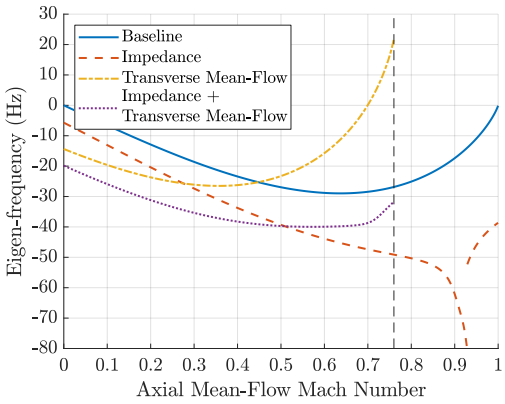

Figure 5.70: Imaginary Part of the Fundamental Eigenfrequency as a Function of Axial Mean-Flow for (a) Baseline, (b) Transverse Impedances, (c) Transverse Mean-Flows, (d) Transverse Impedances + Mean-Flows

Figs. 5.69 and 5.70 show essentially the same qualitative behavior as Figs. 5.54 and 5.55 with increasing axial mean-flow. That is, the natural frequency decreases and the temporal damping increases to a point, then decreases. If only transverse mean-flows are considered, for high axial mean-flow Mach numbers temporal driving is seen. Indeed, the coupling between all 3 effects is largely negligible for small axial mean-flow Mach numbers. That is, each effect can be considered individually and layered upon one another. For higher axial mean-flow Mach numbers, a-typical in combustors, is where the coupling between effects primarily comes into play.

Figs. 5.71 and 5.72 are the same as Figs. 5.69 and 5.70, but with a sub-duct temperature difference of 600 K. All vertical bars again show where the axial mean-flow in sub-duct 2 becomes

supersonic. The solid vertical line is for cases without transverse mean-flow and the dashed vertical line is for cases with transverse mean-flow.

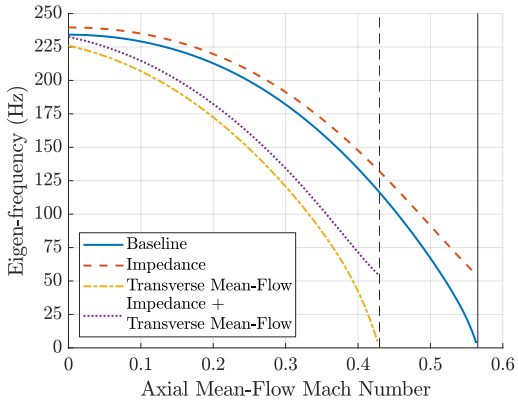

Figure 5.71: Real Part of the Fundamental Eigenfrequency as a Function of Axial Mean-Flow with a Sub-Duct Temperature Difference of 600 K for (a) Baseline, (b) Transverse Impedances, (c) Transverse Mean-Flows, (d) Transverse Impedances + Mean-Flows

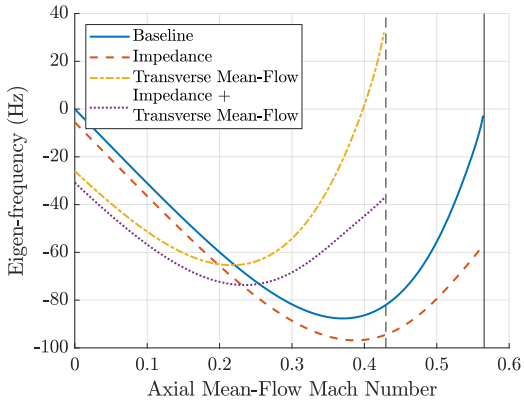

Figure 5.72: Imaginary Part of the Fundamental Eigenfrequency as a Function of Axial Mean-Flow with a Sub-Duct Temperature Difference of 600 K for (a) Baseline, (b) Transverse Impedances, (c) Transverse Mean-Flows, (d) Transverse Impedances + Mean-Flows

The main effect of the sub-duct temperature difference is to squish the available domain through an increase in Mach numbers and to increase the absolute value of the eigenfrequency. The frequency increases by around 40 Hz for each for low axial mean-flow Mach numbers. The slope of the curves in Fig. 5.72 near the origin has become more negative. Thus, if there is axial mean-flow in sub-duct 1, there is more damping than without the temperature difference.

As with Figs. 5.69 and 5.70, the qualitative behavior with the axial mean-flow is the same throughout all cases.

For the eigenfrequency, the qualitative effect of the axial mean-flow is the same for all cases considered. That is, qualitative behavior seen in Figs. 5.54 and 5.55 is essentially preserved no matter what additional effects are considered.

5.2.3 - Mode Shapes and Frequency Response

To plot the mode shapes, one calculates the A's and B's with equation from the solution of equation (5.2.5) and plugs them into plane wave pressure solution. The duct properties used are those in tables 5.1 and 5.2. A value of 1 m/s times the cross-sectional area of the duct is used for the forcing term U_3', and it is assumed that $\rho_{0,3} = \rho_{0,1}$. For the mode shapes the system is driven at 10 Hz below the baseline fundamental eigenfrequency, 163.66 Hz. For the frequency response a 1-500 Hz sweep is performed, and the acoustic pressure is measured at the point $z = D_z$.

The figures that will be presented fall into two categories. As the subsection title suggests, those two categories are mode shapes and frequency response. The mode shapes that will be shown are those of the pressure amplitude and phase as a function of sub-duct axial position, *z*. The pressure magnitude is calculated to be the absolute value of the pressure and the pressure from each sub-duct is stitched together as a piecewise function. The phase of the pressure is calculated by taking the argument of the pressure and stitched together in the same manner as the pressure. The frequency response is calculated by calculating the pressure at a single location, usually at either end of the duct. The frequency is swept from 1 to 500 Hz by simply plugging in said frequencies into the calculation of $k_z^{\pm}$. In all plots, the time dependence is dropped.

5.2.3a - Baseline Solution

The pressure amplitude and phase are given by Figs. 5.73 and 5.74, respectively. Looking first to Fig. 5.73 the pressure amplitude is increased in sub-duct 1, and slightly decreased in sub-duct 2. The pressure node no longer reaches zero. From Fig. 5.74, the effect of axial mean-flow on the pressure phase is pronounced. Essentially two effects are seen. First the overall phase is shifted up for. Second, the axial mean-flow smooths out the discontinuous jump seen in the baseline results.

Note the discontinuous jump due to the sub-duct junction is pronounced when axial mean-flow is considered.

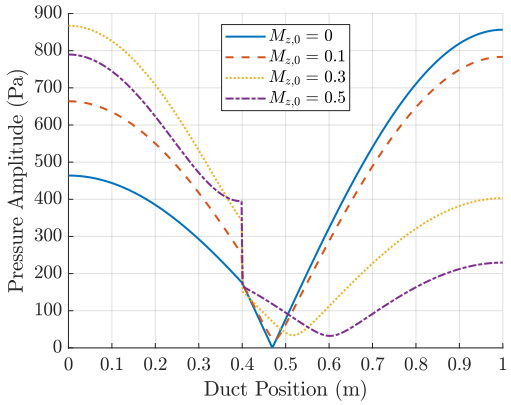

Figure 5.73: Pressure Amplitude for Various Axial Mean-Flow Mach Numbers

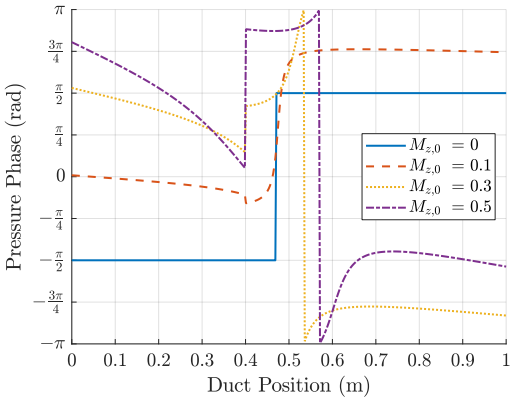

Figure 5.74: Pressure Phase for Various Axial Mean-Flow Mach Numbers

Figs. 5.75 – 5.77 show the frequency response. Fig. 5.75 is the frequency response as a function of the driving frequency for the same axial mean-flows as Figs. 5.73 and 5.74. Figs. 5.76 and 5.77 show the frequency response as a function of driving frequency and axial mean-flow Mach number. They show the frequency response at $z = 1$ m and $z = 0$ m, respectively. The unshaded portions of Figs. 5.76 and 5.77 indicate the eigenfrequency is higher than the maximum scale value of 1000 Pa. The vertical solid line is, again, the driving frequency for the other cases. The dashed horizontal lines represent the axial mean-flow Mach numbers present in Figs. 5.73-5.75.

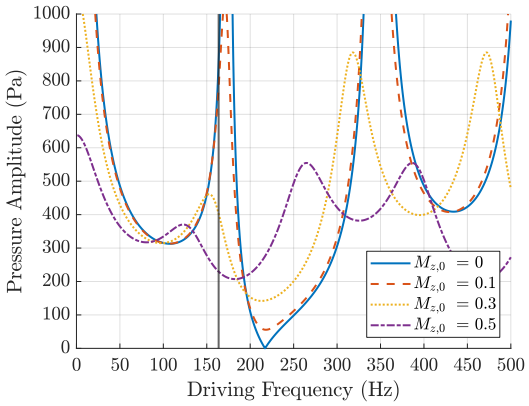

Figure 5.75: Frequency Response as a Function of Driving Frequency for Various Mean-Flow Mach Numbers at z = 1 m

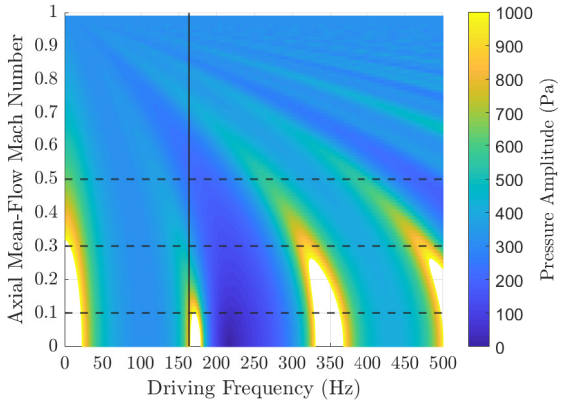

Figure 5.76: Frequency Response as a Function of Axial Mean-Flow Mach Number at z = 1 m

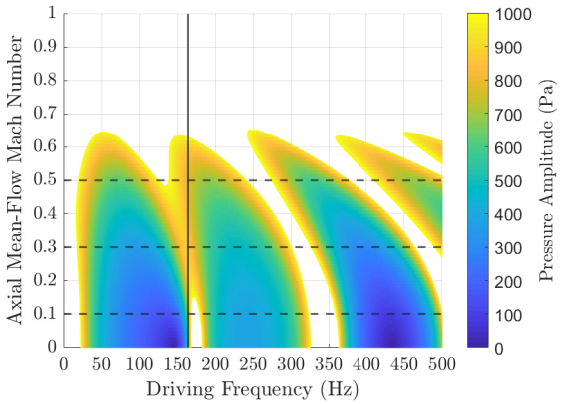

Figure 5.77: Frequency Response as a Function of Axial Mean-Flow Mach Number at z = 0 m

Fig. 5.75 shows the frequency response as a function of driving frequency for two values of axial mean-flow. Overall, the influence of the mean-flow is to damp and shift the natural frequency lower. Furthermore, the natural frequencies get closer together. Figs. 5.76 and 5.77 show the frequency response as a function of driving frequency and axial mean-flow at the outlet and inlet, respectively. The inclusion of two positions is to note how the frequency response can vary drastically based on the chosen location (effectively the sensor location). The two main features from Fig. 5.76 are the increased damping with increasing axial mean-flow and the decrease in natural frequencies with a corresponding decrease with the spacing between these frequencies. At

the inlet, Fig. 5.77, the behavior is starkly different. Rather than being damped by increasing axial mean-flow, the pressure amplitude is driven to extremes. The axial mean-flow at the inlet of a combustor is usually quite small. Therefore, for the rest of this section, only the frequency response at the outlet will be shown.

5.2.3b - Finite Transverse Wall Impedances

For the finite transverse wall impedances, an axial mean-flow Mach number of 0.1 is assumed. The velocity is assumed to be in the $+z$ direction. For the frequency response, a frequency sweep of 1 – 500 Hz is performed, and the pressure amplitude is taken at the outlet of the nozzle, i.e. z = 1 m.

First purely resistive transverse wall impedances are considered. The normalized resistive impedance values considered are 200, 100, and 50 times the characteristic impedance of air at 300 K. Figs. 5.78 and 5.79 show the pressure amplitude and phase, respectively.

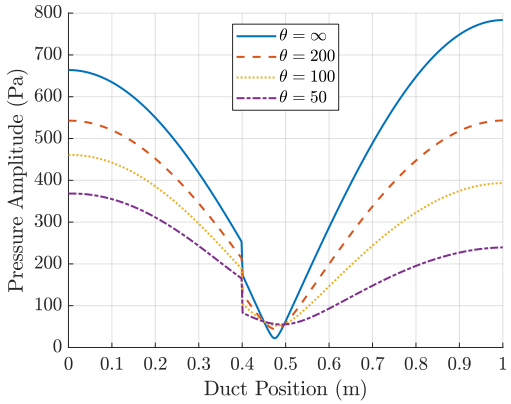

Figure 5.78: Pressure Amplitude for Various Transverse Resistive Impedances

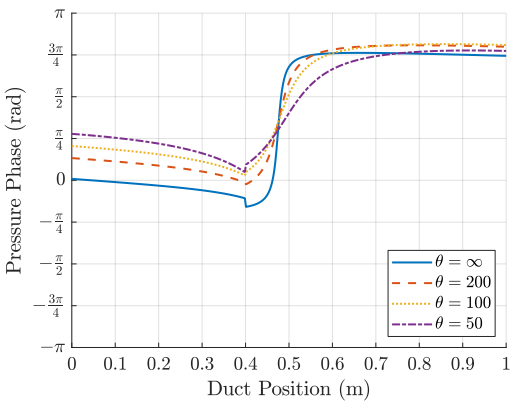

Figure 5.79: Velocity Amplitude for Various Transverse Resistive Impedances

Figs. 5.78 and 5.79 show essentially the same effects seen in Figs. 5.27 and 5.28, respectively. As established for the eigenfrequency, for small values axial mean-flow, the coupling between transverse impedances and axial mean-flow is negligible. Thus, the effects of resistive transverse

impedances are essentially added directly on top of the baseline axial mean-flow case (shown as the solid blue curves).

Figs. 5.80 and 5.81 show the frequency response. Fig. 5.80 shows the frequency response as a function of driving frequency for various transverse resistive impedances. Fig. 5.81 shows the frequency response as a function of driving frequency and transverse resistive impedance.

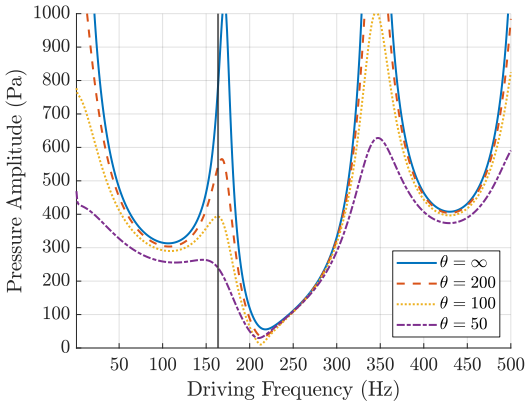

Figure 5.80: Frequency Response for Various Transverse Resistive Impedances

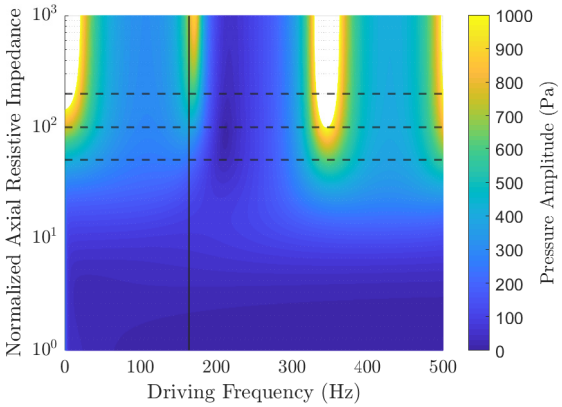

Figure 5.81: Frequency Response as a Function of Transverse Resistive Impedance

The damping effect from the transverse impedances is clearly seen in Fig. 5.80. The frequency shifting effect can be seen very slightly. Fig. 5.81 depicts the same frequency response, but as a function of the transverse resistive impedance. The dotted horizontal lines again indicate the chosen values of the transverse impedance, and the vertical solid line is the chosen driving frequency for Figs. 5.78 and 5.79. As with Fig. 5.80, the damping effect of the transverse impedance is obvious. The frequency shifting effect can just be seen in the figure. Consider the area just to the right of the driving frequency. A slight curve can be seen. This effect is washed out almost completely by the damping effect of the transverse impedance. As with Figs. 5.78 and 5.79, the effect of resistive transverse impedances can essentially be considered separately from the axial mean-flow.

Next consider purely reactive transverse wall impedances. The normalized reactive impedance values considered are +100, and -100 times the characteristic impedance of air at 300 K. Figs. 5.82 and 5.83 are the pressure and velocity amplitudes, respectively.

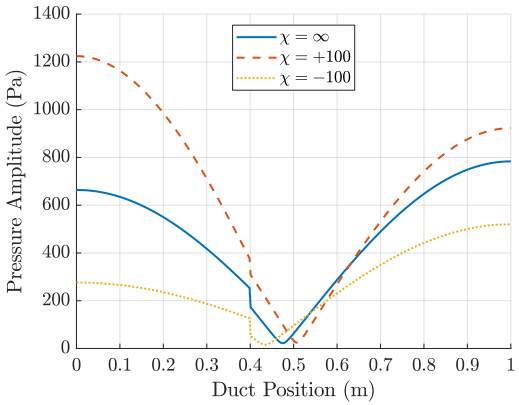

Figure 5.82: Pressure Amplitude for Various Transverse Reactive Impedances

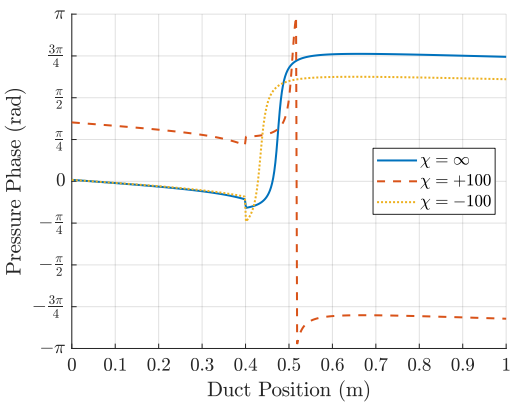

Figure 5.83: Pressure Phase for Various Transverse Reactive Impedances

It is expected that the mode shapes in Fig. 5.82 are like those in Fig. 5.31. That is, it is expected that the change in the mode shapes is mostly because the eigenfrequencies are shifted, rather than the frequency response being damped. As such, it is expected that the mode shape corresponding to $\chi = +100$ is now be driven above its eigenfrequency, and the mode shape corresponding to $\chi = -100$ is now driven below its eigenfrequency. Thus, for the former it is expected that the nodes and anti-nodes move to the right, while for the latter the nodes and anti-nodes shift to the left. For both cases it is expected to have a lower amplitude due to being further away from resonance. This is what is seen in Fig. 5.82. As with the mode shapes, it should be expected that the phase in Fig. 5.83 resembles the phase in Fig. 5.32 with the addition of axial mean-flow. For the phase with $\chi = -100$ that is exactly what is seen. It's approximately the same phase as shown in Fig. 5.32 but with the effect of axial mean-flow layered on top. For $\chi = +100$, the same behavior as in Fig. 5.32 is not seen. Rather, it appears that the $\chi = -100$ curve is shifted up by around $3\pi/8$ radians, but the rising edge is moved to the other side of the $\chi = 0$ curve.

The frequency response is plotted in Figs. 5.84 and 5.85. The vertical solid line in each figure indicates the driving frequency and the horizontal dashed lines in Fig. 5.85 show the values of the reactive impedance.

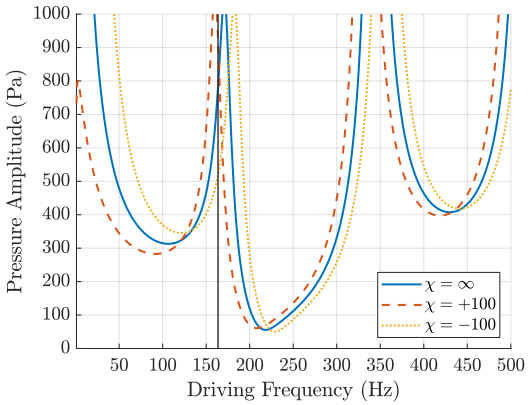

Figure 5.84: Frequency Response for Various Transverse Reactive Impedances

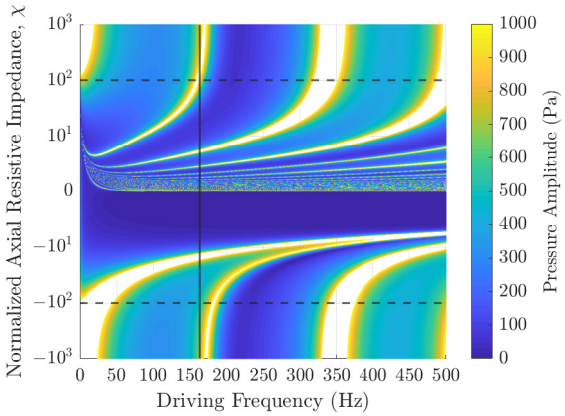

Figure 5.85: Frequency Response as a Function of Transverse Reactive Impedance

Fig. 5.84 confirms the behavior that is expected in the previous discussion. Fig. 5.85 shows the frequency response as a function of the transverse reactive impedance. The horizontal lines show the two chosen values of transverse reactive impedance in Figs. 5.82 – 5.84. The frequency shifting behavior can be clearly seen. For positive values of χ the real part of the eigenfrequencies decrease with decreasing reactive impedance. The eigenfrequencies also move closer and closer together until they are indistinguishable below around $10\rho_0 a_0$. For negative values of χ the real part of the eigenfrequencies increases with decreasing reactive impedance. As with positive values of χ, the resonant frequencies get closer and closer together for small reactive impedances. Because the eigenfrequencies get larger for decreasing reactive impedance, the messy region seen for positive χ's is not seen. Thus, for negative χ's, the frequencies are effectively cut-off for that region. The same behavior is seen without axial mean-flow, i.e. Fig. 5.34. The main difference between the two is the low frequency response. For low driving frequencies the resonant bands are shifted up. This is pronounced for small values of reactive impedance.

Next consider fully complex transverse impedances, or impedances with resistive and reactive parts. The normalized complex impedance values considered are $100 + 100i$ and $100 - 100i$ times the characteristic impedance of air at 300 K. Figs. 5.86 and 5.87 pressure amplitude and phase, respectively.

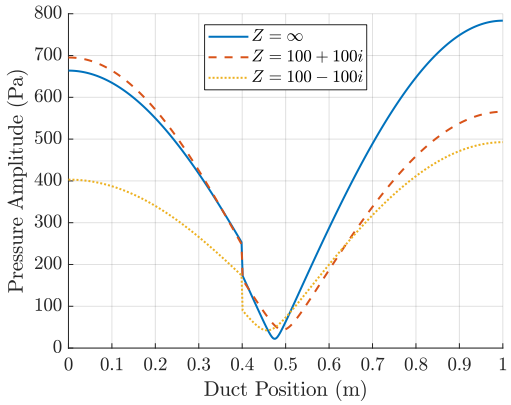

Figure 5.86: Pressure Amplitude for Various Transverse Complex Impedances

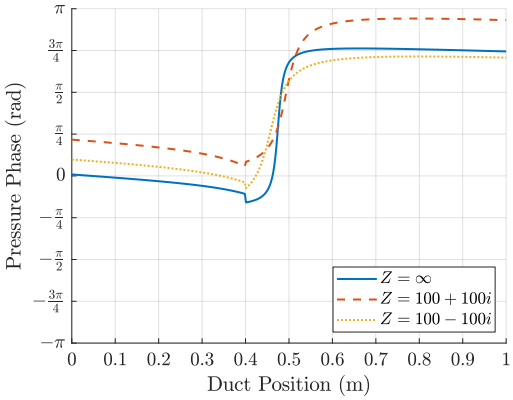

Figure 5.87: Pressure Phase for Various Transverse Complex Impedances

Compare Figs. 5.86 and 5.87 to Figs. 5.35 and 5.36. For the pressure amplitude the results are quite similar. The main difference between the two is an increase in driving for the baseline and $Z = 100 - 100i$ cases. The $Z = 100 + 100i$ case is damped when compared to the case without axial mean-flow, particularly in sub-duct 2. The pressure phase is largely the same but shifted up by $\pi/4$ radians and the obvious smoothing introduced by the axial mean-flow. There appear to be no additional effects introduced with the interplay of axial mean-flow and finite transverse wall impedances. This is due to the fact that the axial mean-flow is quite small, and therefore the coupling is essentially negligible as discussed previously.

Figs. 5.88 and 5.89 show the frequency response. The black vertical line shows the driving frequency. The two dotted horizontal lines indicate the reactance value used for Figs. 5.86 – 5.88. Compare these figures to their no axial mean-flow counterparts, Figs. 5.37 and 5.38. Figs. 5.88 and 5.37 are quite similar. The main difference is the axial mean-flow slightly enhances the effects

of the complex transvers impedances. That is there is slightly more damping, and the frequencies are shifted more with axial mean-flow present. Figs. 5.89 and 5.38 have the same relationship. It is easy to see the increased damping, but the frequency shifting is not readily apparent from Fig. 5.89. Thus, one relies on figures of the form of Fig. 5.88 for frequency shifting estimations.

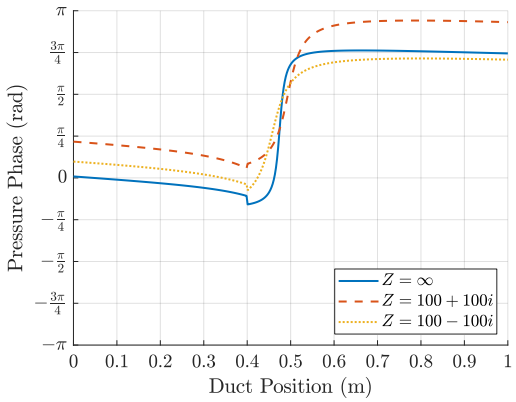

Figure 5.88: Frequency Response for Various Complex Transverse Impedances

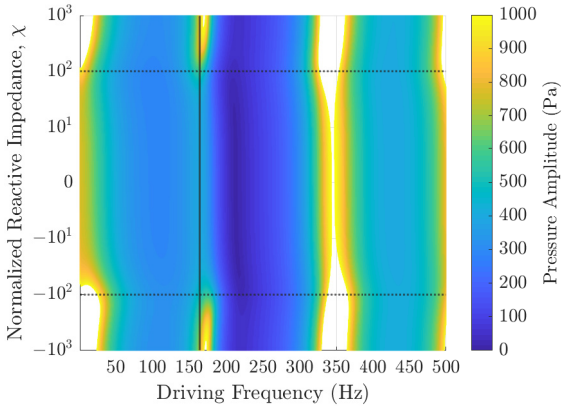

Figure 5.89: Frequency Response as a Function of Driving Frequency and Reactive Impedance with $\theta = 100$

5.2.3c - Non-Zero Transverse Wall Mean-Flows

The introduction of transverse mean-flow complicates the problem significantly, due to the continuity of mean-flows, equation (5.2.20). Therefore, the entire parameter space is not investigated, and is limited to such that only an axial mean-flow of +0.1 in sub-duct 1 is considered. Following in the footsteps of section 5.2.2c, there are three cases to consider: balanced transverse mean-flow, constant transverse mean-flow, and a general case. By constant is meant in the sense of both sub-ducts, i.e. for constant transverse mean-flow the transverse mean-flow is a constant value, equal in both sub-ducts.

First consider the balanced transverse mean-flow case. In this case any transverse mean-flow that enters the duct will leave in the other sub-duct through the transverse walls, according to equation (5.2.20). The axial mean-flow in the entire duct is set to +0.1. Beyond sonic considerations, there are no limits on the transverse axial mean-flow. The chosen values of the axial mean-flow in sub-

duct 1 are +0.1 and -0.1, with the former referring to mean-flow out of the duct, and the latter referring to mean-flow into the duct.

Figs. 5.90 and 5.91 show the acoustic pressure amplitude and phase, respectively for this case. The interaction between the transverse mean-flows and the axial mean-flow separates out the two directions of transverse mean-flow when compared to Fig. 5.39. The pressure phase in Fig. 5.91 is similar to Fig. 5.40, but with the presence of mean-flow shifting the phase up. As with transverse impedances, the axial mean-flow is too low for the coupling between axial and transverse mean-flow to come into play.

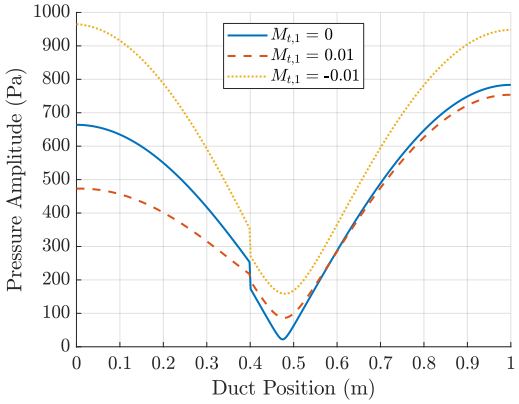

Figure 5.90: Pressure Amplitude for Various Transverse Mean-Flows with Balanced Transverse Mean-Flow

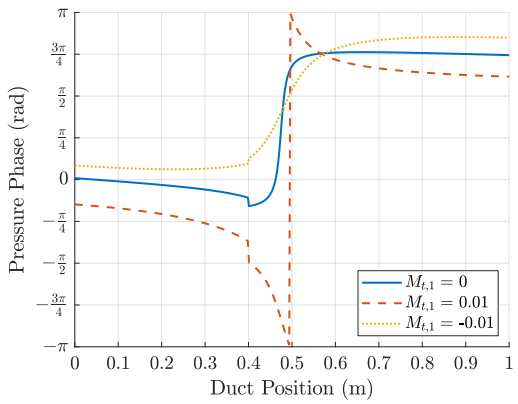

Figure 5.91: Pressure Phase for Various Transverse Mean-Flows with Balanced Transverse Mean-Flow

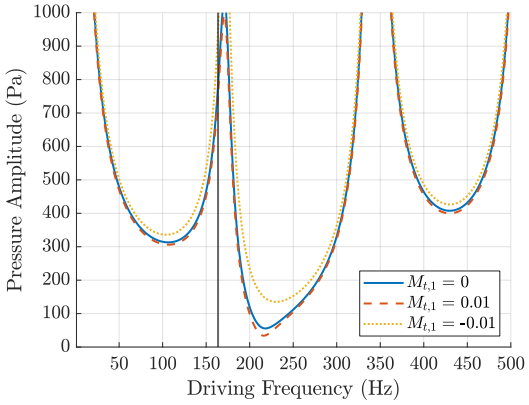

Figure 5.92: Frequency Response for Various Transverse Mean-Flows with Balanced Transverse Mean-Flow

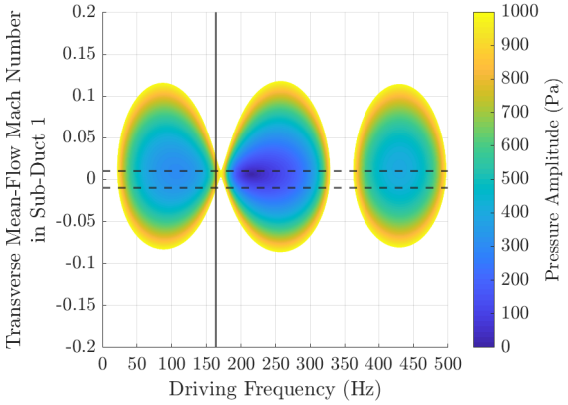

Figure 5.93: Frequency Response as a Function of Transverse Mean-Flow Mach Number in Sub-Duct 1 with Balanced Transverse Mean-Flow

Figs. 5.92 and 5.93 show the frequency response for balanced transverse mean-flow case. Much like the pressure amplitudes, the frequency response in Fig. 5.92 separates out the two directions. Fig. 5.93 shows why. The envelopes seen in Fig. 5.42 have shifted up, due to the presence of axial mean-flow.

Next consider constant transverse mean-flow case. Depending on the amount of momentum entering the duct through the transverse walls, it is possible for the axial mean-flow in sub-duct two to become greater than or equal to one. These limits are encapsulated in equations (5.2.22) and (5.2.23). With the axial mean-flow set to +0.1, these limits are -0.0225, 0.0025, and 0.0275, respectively. Figs. 5.94 and 5.95 show the acoustic pressure amplitude and phase for this case.

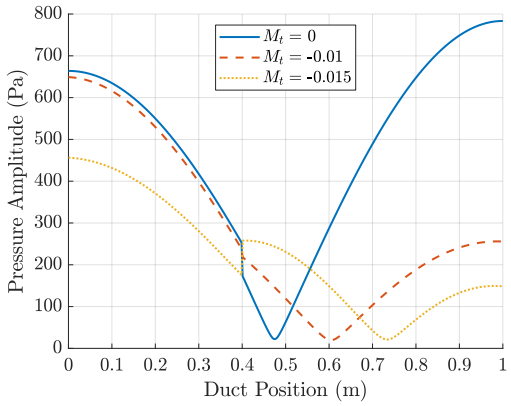

Figure 5.94: Pressure Amplitude for Various Transverse Mean-Flows with Constant Transverse Mean-Flow

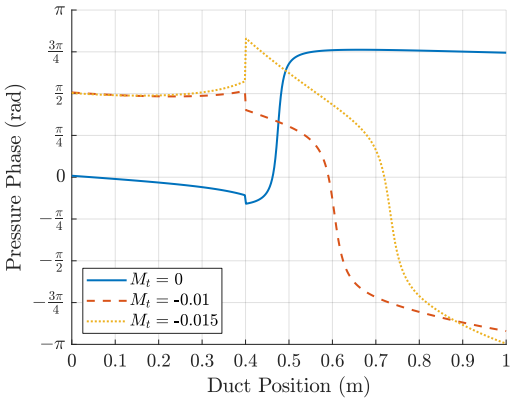

Figure 5.95: Pressure Phase for Various Transverse Mean-Flows with Constant Transverse Mean-Flow

Both plots are substantially different from their counterparts for the constant axial mean-flow case, Figs. 5.90 and 5.91. There is significant frequency shifting evident in the pressure amplitude, and there appears to be damping. The pressure phases are roughly inverted for opposite directions in sub-duct 2, like in the constant axial mean-flow scenario. However, there is a significant phase shift at the sub-duct junction, while the phase shift at the junction in Fig. 5.91 is minimal.

Figs. 5.96 and 5.97 show the frequency response. The horizontal dashed black lines in Fig. 5.97 indicate the chose values for the constant transverse mean-flow Mach number. The vertical range

in Fig. 5.97 is chosen such that the axial mean-flow in sub-duct 2 is between 0 and 1. It is 0 at the top of Fig. 5.97 and 1 at the bottom. It is clearly seen that for both transverse mean-flow Mach numbers are driven above their fundamental frequency, i.e. the real part of the fundamental eigenfrequency has been shifted down. Furthermore, there is a significant amount of damping present from the transverse mean-flow, as expected. Fig. 5.97 contains many interesting features. First note the damping effect is not constant with transverse mean-flow. Specifically, high frequency response re-appears near the edges of the plot. Next, the resonant frequencies are shifted down in frequency as the magnitude of the transverse mean-flow increases. This continues until the axial mean-flow Mach number in sub-duct two approaches +1, at which point all frequency response is damped out. Finally, as the transverse mean-flow increases the modes get closer and closer together.

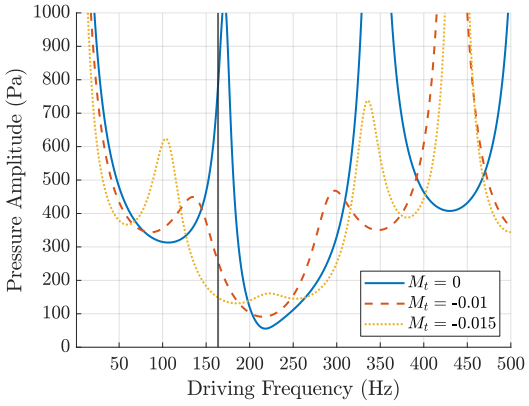

Figure 5.96: Frequency Response for Various Transverse Mean-Flows with Constant Transverse Mean-Flow

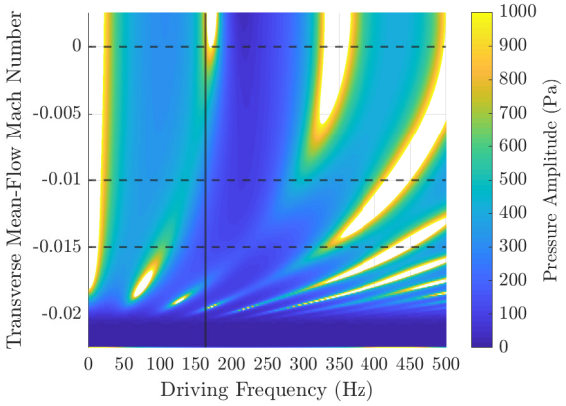

Figure 5.97: Frequency Response as a Function of Transverse Mean-Flow Mach Number in Sub-Duct 1 with Constant Transverse Mean-Flow

Finally, consider the general case. For this case the transverse mean-flows are set to 0 in sub-duct 1 and set to -0.01 in sub-duct 2. As in the previous case, the transverse mean-flow is limited by equations (5.2.22) and (5.2.23), with slight modifications. Because $\xi_{M,1} = 0$, one replaces ξ_M

with $\xi_{M,2}$ and D_z with $D_{z,2}$. Therefore, the relevant limits for this general case are -0.045, 0.005, and 0.055, respectively.

Figs. 5.98 and 5.99 show the acoustic pressure amplitude and phase for this case, respectively.

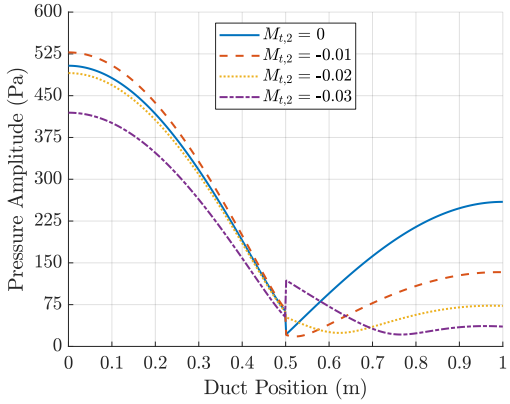

Figure 5.98: Pressure Amplitude for Various Transverse Mean-Flows with Transverse Mean-Flow only in Sub-Duct 2

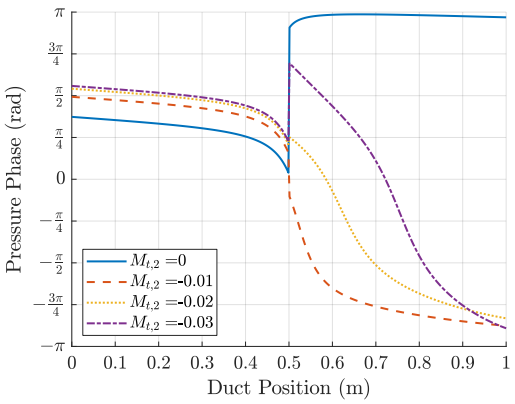

Figure 5.99: Pressure Phase for Various Transverse Mean-Flows with Transverse Mean-Flow only in Sub-Duct 2

The pressure amplitude and phase are shown in Figs. 5.98 and 5.99. The pressure amplitude is noticeably damped at the outlet. The phase with transverse mean-flow resembles the case shown in Fig. 5.95 with $M_t = -0.01$. Indeed, this general case is really a sub-set of the constant transverse mean-flow case, thus similar results are obtained.

Figs. 5.100 and 5.101 show the frequency response as a function of driving frequency and transverse mean-flow Mach number in sub-duct 2.

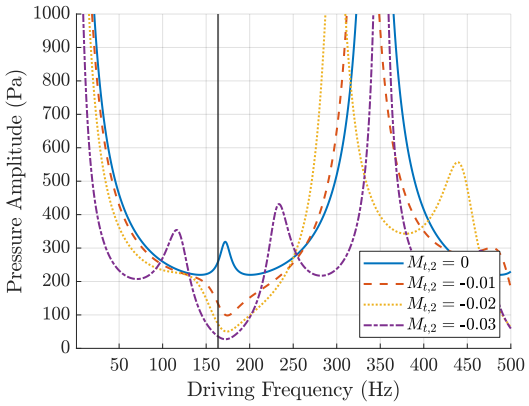

Figure 5.100: Frequency Response for Various Transverse Mean-Flows with Transverse Mean-Flow only in Sub-Duct 2

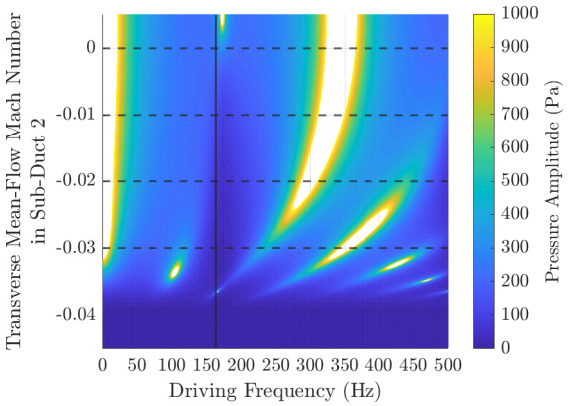

Figure 5.101: Frequency Response as a Function of Transverse Mean-Flow Mach Number in Sub-Duct 2 with Transverse Mean-Flow only in Sub-Duct 2

As expected, Figs. 5.100 and 5.101 show essentially the same behavior as Figs. 5.96 and 5.97.

5.2.3d - Non-Zero Sub-Duct Temperature Difference

As with section 5.2.2d, the main consideration introduced by a sub-duct temperature difference is the limitation on the axial mean-flow in sub-duct 2. These limitations are shown in Fig. 5.66 (equation (5.2.27)). For the sake of simplicity, only consider an axial mean-flow Mach number of +0.1 in sub-duct 1, as this value is below the possible limit for all temperatures considered. The sub-duct temperature differences considered are 0, 300, 600, and 900 Kelvins. Figs. 5.102 and 5.103 are the pressure amplitude and phase for this case.

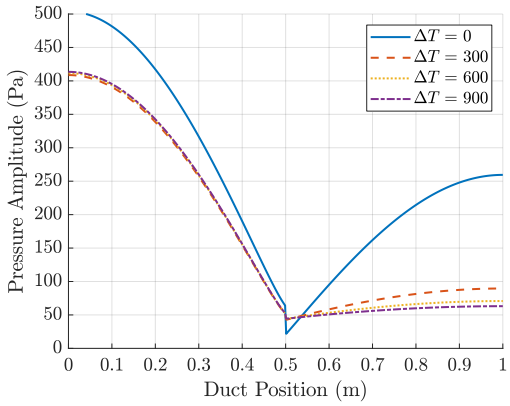

Figure 5.102: Pressure Amplitude for Various Sub-Duct Temperature Differences

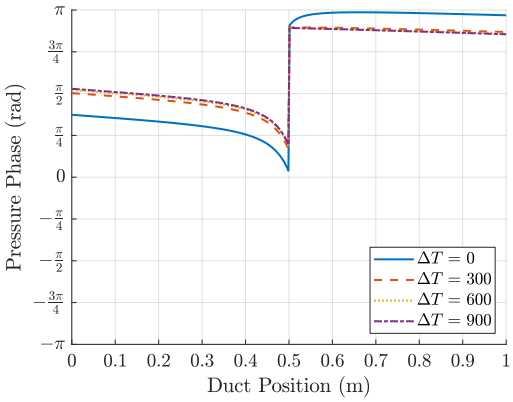

Figure 5.103: Velocity Amplitude for Various Sub-Duct Temperature Differences

Figs. 5.102 and 5.103 are the pressure amplitude and phase for this case. All the lines with sub-duct temperature differences show the same behavior. Based on the pressure distribution in sub-duct 1, there is some amount of damping provided by the temperature difference. In sub-duct two, it appears that the resonant frequency has shifted, due to each line being at a different value near $z = 1$ *m*. While there is undoubtably damping, one would expect each line to be very close to one another as with the portion inside sub-duct 1. As is known from section 5.1.3d, the increasing sub-duct temperature difference causes the natural frequencies of the system to rise. Thus, for all cases with a non-zero sub-duct temperature difference, the system is being driven far below resonance. This effect is easily seen in the frequency response plots, Figs. 5.104 and 5.105.

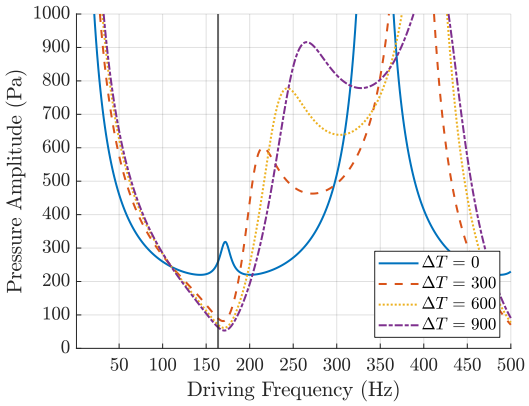

Figure 5.104: Frequency Response for Various Sub-Duct Temperature Differences

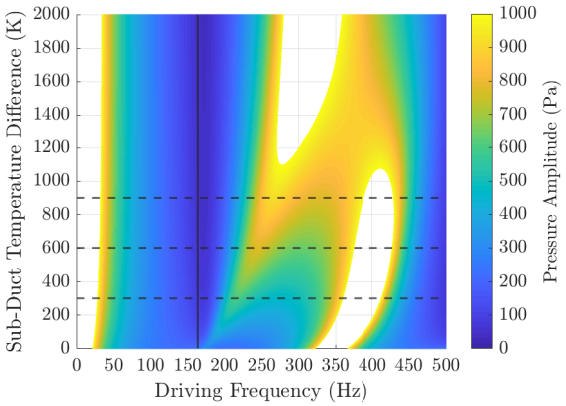

Figure 5.105: Frequency Response as a Sub-Duct Temperature Difference

Fig. 5.104 shows the frequency response as a function of driving frequency for the three sub-duct temperature differences in question. Fig. 5.104 shows that the damping and resonant frequency shifting roughly scales with the sub-duct temperature difference. Furthermore, the chosen driving frequency is highly damped for all 3 non-zero sub-duct temperature difference values chosen. Fig. 5.105 expands on this further. Fig. 5.105 shows that this entire band is damped simply by having a temperature difference in the ducts at the classical driving frequency. This is most likely due to the location of the sub-duct junction. As noted in section 5.1.3a, the mere presence of a sub-duct junction causes certain modes to be damped.

5.2.3e - Combination of Parameters

In this section each effect is layered on top of one another. The fundamental case is that depicted in Figs. 5.73 and 5.74. First finite transverse impedances are added. These impedances are equal in both sub-duct 1 and sub-duct 2. Furthermore, the impedance value is chosen to be $100 + 100i$, normalized to $\rho_0 a_0$ for air at the temperature in the duct.

In the case of different temperatures in each sub-duct, the transverse impedance in each sub-duct is normalized to the local characteristic impedance of air at the temperature in the sub-duct.

Therefore, the transverse wall impedance in sub-duct 2 is scaled to 176.86 + 176.86*i* such that the actual impedances in sub-duct 1 and 2 are equal. For the cases with transverse mean-flows the transverse mean-flow Mach numbers for each transverse wall are assumed to be equal within each sub-duct. For sub-duct 1, the transverse mean-flow Mach number is chosen to be 0. For sub-duct 2, the transverse mean-flow Mach number is chosen to be -0.01. The negative sign refers to mean-flow flowing into the duct. Finally, a sub-duct temperature difference is introduced, with a value of 600 Kelvins. The added parameters are the same as those detailed in table 5.3.

The results of layering upon the pressure amplitude and phase are shown in Figs. 5.106, 5.107, 5.113, and 5.114. All mode shapes are at a driving frequency of 163.66 Hz and an axial mean-flow Mach number in sub-duct 1 of 0.1.

The Frequency response is shown in Figs. 5.108 and 5.115. The black solid vertical line denotes the driving frequency used for all the pressure amplitude and phase plots. Figs. 5.109 – 5.112 and 5.116 – 5.119 show the frequency response plots as a function of driving frequency and axial mean-flow in sub-duct 1. As with Figs. 5.108 and 5.115 the black solid vertical line denotes the driving frequency for previous plots. The horizontal black dashed line denotes the axial mean-flow Mach number in sub-duct 1 used for the other figures in this section.

Figs. 5.106 and 5.107 show the pressure amplitude and phase for the layer cases with axial mean-flow and no sub-duct temperature difference. Compare these figures to Figs. 5.47 and 5.48. The axial mean-flow damps the system. The axial mean-flow has a large effect of the phase of the pressure.

Figs. 5.113 and 5.114 show the pressure amplitude and phase with axial mean-flow and a sub-duct temperature difference off 600 K. Compare these two figures to Figs. 5.49 and 5.50. Unlike when

there was no temperature difference, the damping overall is lower. However, as the parameters are added on top, the damping increases. If both transverse impedances and mean-flows are included, the damping is significant. The phase in Fig. 5.114 is significantly different from the phase in Fig. 5.50. There is an obvious phase shift at the sub-duct junction. However, both the transverse impedances and mean-flows have essentially the same effect as in Fig. 5.50. The transverse impedance doesn't have a negligible effect on the phase, while the transverse mean-flow causes the phase to gently slope.

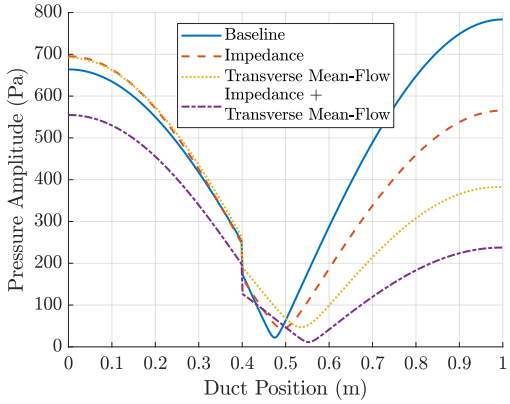

Figure 5.106: Pressure Amplitude for (a) Baseline, (b) Transverse Impedances, (c) Transverse Mean-Flows, (d) Transverse Impedances + Mean-Flows

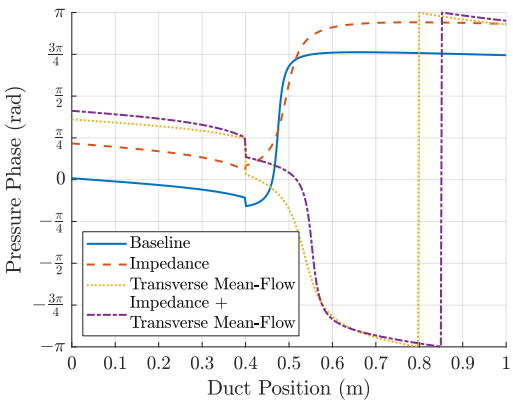

Figure 5.107: Velocity Amplitude for (a) Baseline, (b) Transverse Impedances, (c) Transverse Mean-Flows, (d) Transverse Impedances + Mean-Flows

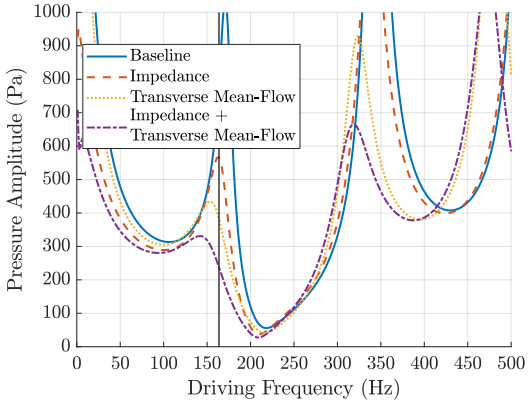

Figure 5.108: Frequency Response for (a) Baseline, (b) Transverse Impedances, (c) Transverse Mean-Flows, (d) Transverse Impedances + Mean-Flows

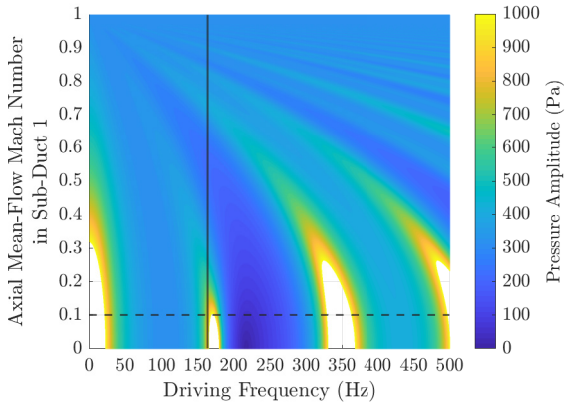

Figure 5.109: Frequency Response as a Function of Axial Mean-Flow in Sub-Duct 1 with no added Properties (Baseline)

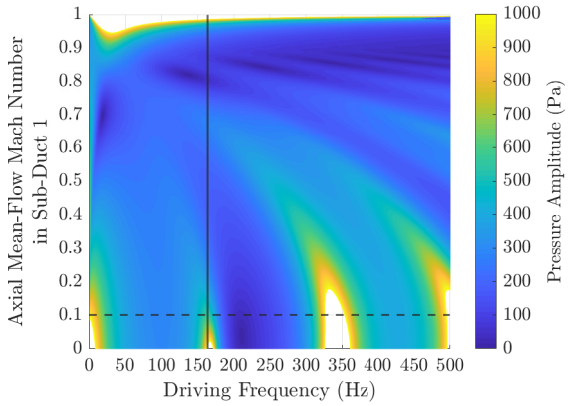

Figure 5.110: Frequency Response as a Function of Axial Mean-Flow in Sub-Duct 1 with Added Transverse Impedances

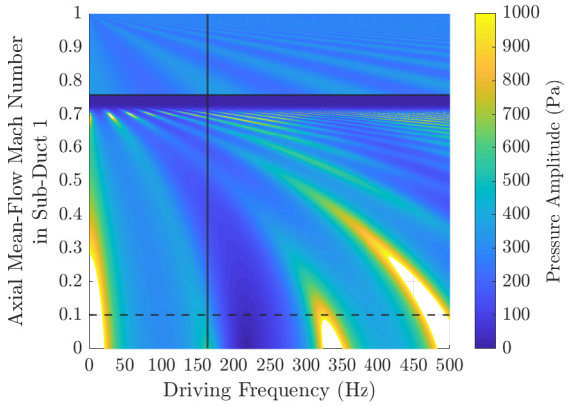

Figure 5.111: Frequency Response as a Function of Axial Mean-Flow in Sub-Duct 1 with Added Transverse Mean-Flow

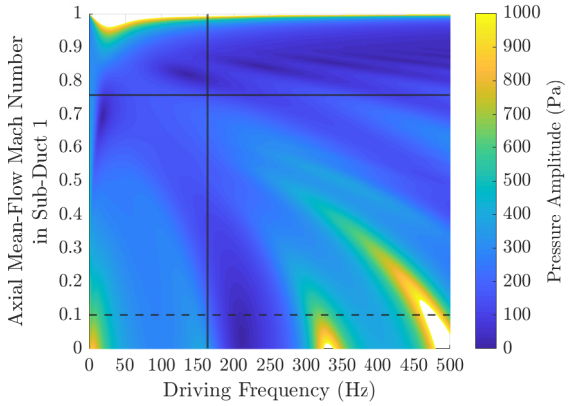

Figure 5.112: Frequency Response as a Function of Axial Mean-Flow in Sub-Duct 1 with Added Transverse Impedances and Mean-Flow

Figs. 5.108 and 5.115 show the frequency response as a function of driving frequency with axial mean-flow with and without a sub-duct temperature frequency, respectively. Compare Fig. 5.108 with 5.51. With axial mean-flow each effect adds significant damping. One can draw the same conclusions for Figs. 5.115 and 5.52. Again, there is significant damping from each effect. With non-zero transverse mean-flow the first resonant frequency completely damped out in the frequency space. However, the second resonant frequency still has a high response with axial mean-flow. The transverse mean-flow also noticeably shifts the position of the second resonant frequency down.

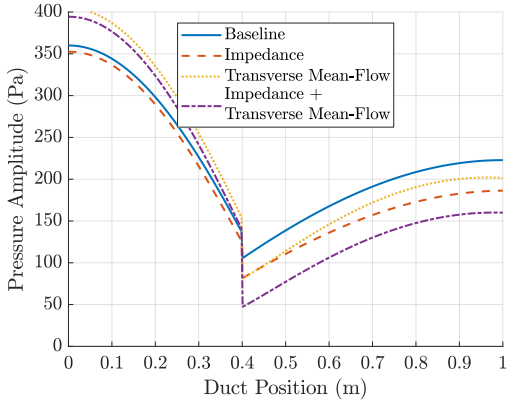

Figure 5.113: Pressure Amplitude for (a) Baseline, (b) Transverse Impedances, (c) Transverse Mean-Flows, (d) Transverse Impedances + Mean-Flows

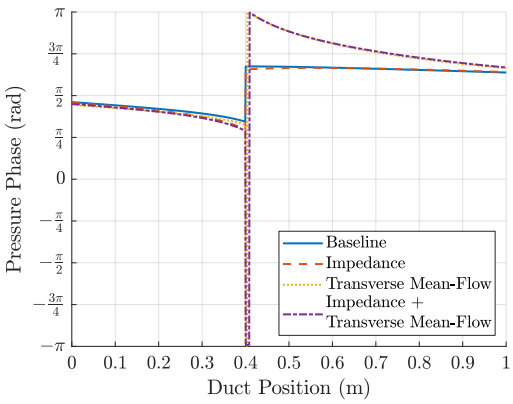

Figure 5.114: Velocity Amplitude for (a) Baseline, (b) Transverse Impedances, (c) Transverse Mean-Flows, (d) Transverse Impedances + Mean-Flows

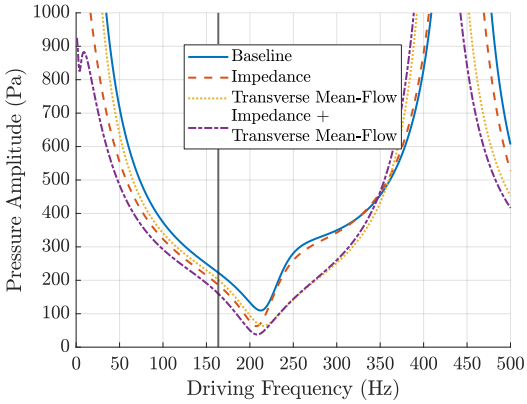

Figure 5.115: Frequency Response for (a) Baseline, (b) Transverse Impedances, (c) Transverse Mean-Flows, (d) Transverse Impedances + Mean-Flows

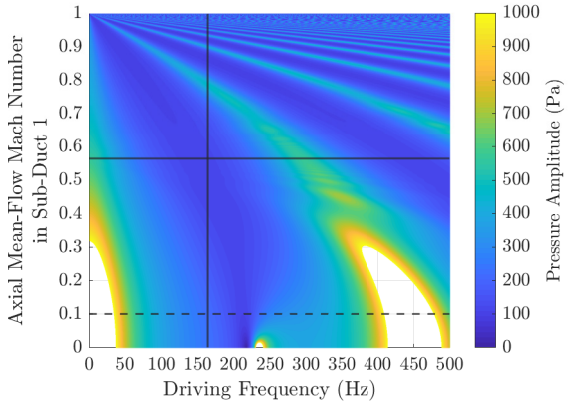

Figure 5.116: Frequency Response as a Function of Axial Mean-Flow in Sub-Duct 1 with no added Properties (baseline)

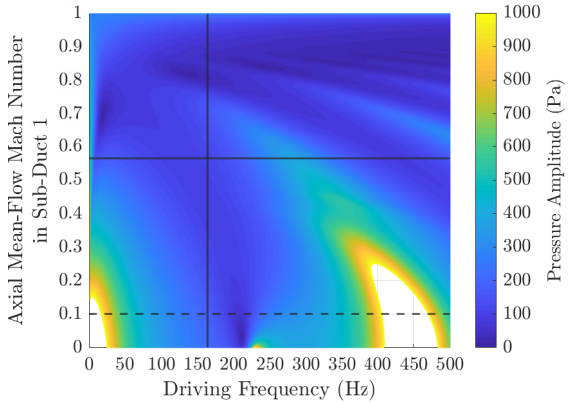

Figure 5.117: Frequency Response as a Function of Axial Mean-Flow in Sub-Duct 1 with Added Impedances

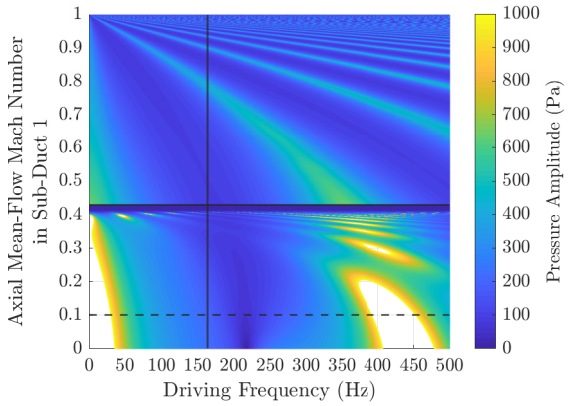

Figure 5.118: Frequency Response as a Function of Axial Mean-Flow in Sub-Duct 1 with Added Transverse Mean-Flow

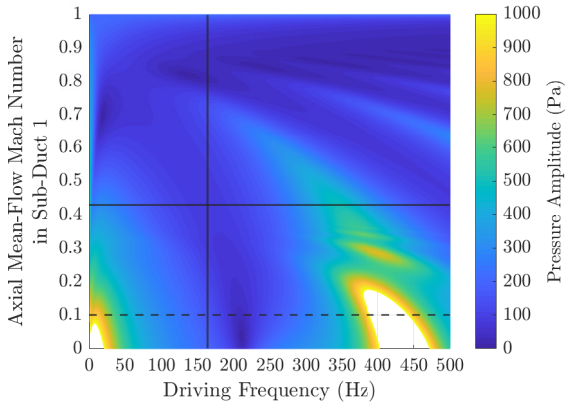

Figure 5.119 : Frequency Response as a Function of Axial Mean-Flow in Sub-Duct 1 with Added Sub-Duct Temperature Difference

Figs. 5.109 – 5.112 show the frequency response as a function of driving frequency and axial mean-flow. Fig. 5.109 is the baseline case, Fig. 5.110 is with added transverse impedances, Fig. 5.111 is with added transverse mean-flow, and Fig. 5.112 is with added transverse impedances and mean-flows. The baseline frequency response is symmetric about 0 axial mean-flow in sub-duct 2 and is reminiscent of Fig. 5.54. When finite transverse impedances are included, the frequency response damped for positive axial mean-flows in sub-duct 1 and driven for negative axial mean-flows in sub-duct 1. When transverse mean-flows are considered, the response is "squished" into a smaller domain. The dark black line shows where the axial mean-flow in sub-duct 2 becomes supersonic. This is reminiscent of Fig. 5.64. Fig. 5.112 is the combination of transverse impedances and mean-flow. Qualitatively Fig. 5.112 is the response of Figs. 5.110 and 5.111 overlaid on top of one another. However, there are notable differences. First, the sharp band which denoted supersonic axial in sub-duct 2 is missing in Fig. 5.112. The axial mean-flow in sub-duct 2 still becomes supersonic, but there is no sharp feature of that. The other notable difference is the large frequency response for large negative axial mean-flows in sub-duct 1. This would never happen in a combustor because the mean-flow will never be in the reverse direction, especially at

such a high Mach number. Nevertheless, it is a significant feature that is resulting from the combination of axial mean-flow, transverse mean-flow, and transverse impedance effects.

Figs. 5.116 – 5.119 are the counterparts of Figs. 5.109 – 5.112, but with a sub-duct temperature difference of 600 K. Comparing Fig 5.116 with 5.109 reveals that increasing the temperature in sub-duct 2 reduces the frequency response. From section 5.2.2d, it is known that a sub-duct temperature difference will cause the available values of $M_{z,0,1}$ to be restricted. However, there is no strict boundary shown in Fig. 5.116. With Fig. 5.117, this boundary is easier to visualize due to the depressed band first seen in Fig. 5.110. This band is shifted up in Fig. 5.117. The addition of transverse impedances also further reduces the frequency response. Fig. 5.118 show the frequency response when transverse mean-flow is included. In this, the places where $M_{z,0,2}$ becomes supersonic are apparent as sharp depressions in the frequency response for all frequencies. Compared to Fig. 5.111, the domain is "squished" as in section 5.2.2d. Finally, when both transverse mean-flow and transverse impedances are included, the effects are layered on top of one another. The large depressive band re-appears, and the sharp delineation of supersonic axial mean-flow in sub-duct 2 is somewhat visible near $M_{z,0,1} = 0.4$. Overall the frequency response for positive values of $M_{z,0,1}$ is reduced when all effects (i.e. axial mean-flow, transverse mean-flow, transverse wall impedances, and a sub-duct temperature difference) are included.

Chapter 6

Discussion of Application Cases

Chapter 6 discusses the results presented in chapter 5. The chapter is divided as follows. Section 6.1 discusses the axial wavenumber and section 6.2 discusses general trends.

First, a brief discussion on the form of the results. Consider the form of the solution, i.e. a plane wave:

$$p'(z,t) = \left(Ae^{+ik_z^+ z} + Be^{-ik_z^- z} \right) e^{-i\omega t} \tag{6.0.1}$$

Both $k_z^{\pm}$ and ω are complex and can be represented as:

$$\begin{aligned} k_z^{\pm} &= k_{z,r}^{\pm} + ik_{z,i}^{\pm} \\ \omega &= \omega_r + i\omega_i \end{aligned} \tag{6.0.2}$$

Inserting equations (6.0.2) into equation (6.0.1) one obtains:

$$p'(z,t) = \left(Ae^{+ik_{z,r}^+ z} e^{-k_{z,i}^+ z} + Be^{-ik_{z,r}^- z} e^{+k_{z,i}^- z} \right) e^{-i\omega_r t} e^{+\omega_i t} \tag{6.0.3}$$

The effects of the eigen-frequency and axial wavenumbers are plainly seen in equation (6.0.3). If the imaginary component of the eigen-frequency is positive the solution exhibits temporal driving, while if the imaginary component of the eigen-frequency is negative the plane wave exhibits temporal damping. The term $e^{+\omega_i}$ is referred to as the damping factor. Therefore, the sign of the imaginary component of the eigenfrequency governs the linear temporal stability of the system.

The effects of the axial wave-numbers can also be seen in equation (6.0.3). Again, the driving/damping is governed by the imaginary component of each axial wave number. Note the sign difference between the forward and rearward travelling wave components. The forward traveling component exhibits spatial damping when it's imaginary component it's eigenfrequency is positive and driving for the reverse. It is the opposite for the rearward travelling wave, which exhibits similar behavior as the eigen-frequency.

There are three important components to remember

1. The real part of the eigenfrequency is the frequency
2. The imaginary part of the eigenfrequency is the temporal driving or damping
3. The imaginary parts of the axial wavenumbers are the spatial damping for each respective wave component (i.e. forward and rearward travelling waves)

For the mode shapes and frequency responses, three things are plotted: the pressure mode shape, the phase of the pressure, and a 500 Hz frequency response sweep. The pressure amplitude and phase are plotted as a function of the axial position of the duct. It is difficult to tell the effect of each parameter directly on the mode shapes, since the chosen driving frequency plays a large role in the frequency response. Because of this, the mode shapes are supplemented with the frequency response, which provides clarity and context to the mode shapes. These figures show the resonant frequencies and damping/driving in the frequency domain.

6.1 - Axial Wavenumber

The axial wavenumber is determined completely by equation (3.4.2), for each individual sub-duct. Therefore, it is independent of the boundary conditions imposed on the z boundaries. As such, it has been moved to the discussion section, since its calculation does not rely on the particular

application case per-say. Nevertheless, this section is broken down in a similar manner to Chapter 5.

6.1.1 - Closed – Closed Duct

6.1.1a - Baseline Solution

Consider the baseline axial wavenumber, given by equation (5.1.15). The axial wavenumber is equal to the full duct wavenumber, k_0.

6.1.1b - Finite Transverse Wall Impedances

Consider the effect of finite wall impedances on the axial wavenumber. Note that at the eigenfrequencies the axial wavenumber is calculated using equation (5.1.20). For all other frequencies, equation (5.1.22) is used. Splitting the impedance parameter into real and imaginary parts yields

$$\sqrt{k_0\left(k_0 - \xi_{Z,i} + i\xi_{Z,r}\right)} \tag{6.1.1}$$

Because it is impossible to drive the system at a complex frequency, the total wavenumber is assumed to be purely real. If the transverse impedances are resistive only, the axial wavenumber will always be complex. As the wall impedances increase the axial wavenumber approaches the value of the total wavenumber. For purely reactive transverse impedances another critical impedance value appears.

$$\chi = -\frac{a_0}{f\pi}\left(\frac{1}{D_x} + \frac{1}{D_y}\right) \tag{6.1.2}$$

Because the transverse wall impedances are typically fixed or much harder to change than the driving frequency, equation (6.1.2) can be re-arranged to form a cut-off frequency.

$$f = -\frac{a_0}{\chi\pi}\left(\frac{1}{D_x}+\frac{1}{D_y}\right) \tag{6.1.3}$$

Note the minus sign in equations (6.1.2) and (6.1.3). If the reactances of the transverse walls are positive, there is no cut-off frequency, as such a frequency would be negative.

For fully complex impedances the general trends of equation (6.1.1) are not obvious or intuitive. In order to understand, observe the complex expansion of the following radical

$$\sqrt{x+iy} = \cos\left(\frac{1}{2}\arg(x+iy)\right)\sqrt[4]{x^2+y^2} + i\sin\left(\frac{1}{2}\arg(x+iy)\right)\sqrt[4]{x^2+y^2} \tag{6.1.4}$$

The signs of the real and imaginary components are completely determined by the sign and cosine of half the argument of the original complex number in the square root. The output of the argument function is limited to $[-\pi,\pi]$, and thus half of that is $[-\pi/2,\pi/2]$. Therefore, the real part must be positive or zero, but never negative. The possible values available can be further restricted by noting that the imaginary part of the square root, i.e. equation (6.1.1), will always be positive. Thus, the output of the argument is further restricted to $[0,\pi]$. Therefore, the imaginary component will also always be positive, for all driving frequencies and transverse impedances. Thus, there will always be spatial driving in such systems.

6.1.1c - Non-Zero Transverse Wall Mean-Flows

Equation (5.1.36) governs the axial wavenumber for this case. The effect of the transverse mean-flows converts directly to damping or driving. As per equation (6.0.3), if the transverse mean-flow parameter is positive (i.e. net flow out of the sub-duct) there will be spatial damping for the $+z$ wave component and spatial driving for the $-z$ wave component. For flow into the duct the

impedance parameter is negative and the $+z$ component is spatially driven and the $-z$ wave component is spatially damped.

6.1.1d - Non-Zero Sub-Duct Temperature Difference

The effect of temperature on the axial wavenumber is straightforward. This is because each sub-duct has its own set of axial wavenumbers. There are no additional effects besides temperature considered here, so the axial wavenumber is equal to the total wavenumber in each sub-duct, i.e. the frequency of the system divided by the speed of sound in the duct. Thus, for sub-duct two, which will have a greater temperature will therefore have a greater speed of sound. This means that the axial wavenumber is smaller in sub-duct two. This trend should generally hold even when transverse impedances and mean-flow are considered, due to the form of equation (5.1.1).

6.1.2 - M-dot – Nozzle Duct

6.1.2a - Baseline Solution

The baseline axial wavenumber is given by equation (5.2.6). The axial wavenumbers are now different for the $+z$ and $-z$ wave components. Henceforth they will be denoted as the *forward* axial wavenumber and *rearward* axial wavenumber. Consider axial mean-flow in the $+z$ direction. As the axial mean-flow increases the forward axial wavenumber will decrease in value, while the rearward axial wavenumber will increase. The opposite is true if the axial mean-flow is in the $-z$ direction. From equation (5.2.6) any damping or driving is directly proportional to the temporal damping or driving, being scaled by the axial mean-flow. When the axial mean-flow Mach number is equal to ± 1 the forward and rearward axial wavenumbers each blow up. Such mean-flow Mach numbers are not typical for combustors and one must include other effects to ensure accuracy in those high flow regions. This is beyond the scope of this work.

Axial mean-flows in the -*z* direction are considered here simply because the axial wavenumber is agnostic to the boundary conditions on the *z* boundaries.

6.1.2b - Finite Transverse Wall Impedances

The axial wavenumber is described by equation (5.2.17). If the impedance parameter is set to 0, equation (5.2.6) is obtained, which is what is expected. The introduction of finite impedances also indirectly proportional to the frequency. Thus, for high frequencies equation (5.2.17) again becomes equation (5.2.6). One must be careful with this claim. In the real world, the transverse impedances will depend on the eigenfrequency itself. Therefore, while it appears that the effect of impedance is solely limited to low frequencies, this is not true in real systems. The application of an impedance model is not considered in the present work. However, this analysis can include impedance models and is a possible extension of this work. Due to this limitation more attention is paid to the effect of the transverse mean-flows, rather than their frequency dependence. Compare equation (5.2.17) to equation (5.2.22). First, if the axial mean-flow is set to 0, equation (5.2.17) reduces to equation (5.2.22) as expected. The most straightforward way to understand this equation is to plot it. Only the imaginary component will be considered since the spatial damping/driving is determined solely by the imaginary component.

Fig. 6.1 shows the imaginary component of the forward axial wavenumber. The rearward axial wavenumber is not shown, since one simply reflects Fig. 6.1 across the x-axis to obtain it.

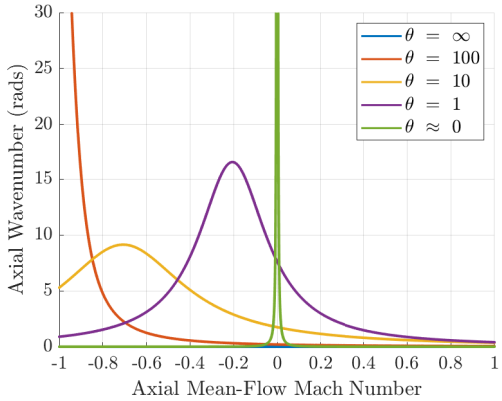

Figure 6.1: Imaginary Part of Forward Axial Wavenumber as a Function of Axial Mean-Flow Mach Number for Various Resistive Impedances

For rigid walls, i.e. $\theta = \infty$, the imaginary component of the axial wavenumbers is zero, as indicated in equation (5.2.6). For finite but large impedance values, the forward axial wavenumber remains unchanged except around $M_{z,0} = -1$. Here the wavenumber spikes, but it does not go to infinity. This behavior is peculiar. Consider the red curve as the transverse wall impedance becomes rigid. The value at $M_{z,0} = -1$ approaches +∞, and the value everywhere else vanishes. This seems strange, since equation (5.2.6) suggests that the imaginary component should be zero. However, one must remember that +∞ is undefined, and extends into the complex plane. As the transverse walls become less rigid this spike decreases and shifts to the right. For further decreases, the spike begins to increase and move further to the right. This continues until the transverse impedance approaches zero, at which point one obtains something reminiscent of the Dirac delta function, where the function vanishes everywhere except for at 0, where its value is infinite. This behavior, like the behavior at $M_{z,0} = -1$ is largely inaccessible to real systems, since the *normalized* transverse impedances must be less than 1 (i.e. less than the characteristic impedance of air). Such a system would not have any boundaries and the system itself becomes undefined.

Thus, for realistic values of axial mean-flow and transverse resistive impedances the axial wavenumbers will introduce spatial driving.

Next consider purely imaginary impedances. In this case one can write equation (5.2.17) in terms of the transverse reactance

$$k_z^{\pm} = \frac{k_0\sqrt{1+2\left(\frac{1}{D_x}+\frac{1}{D_y}\right)\frac{1}{\chi k_0}}}{1\pm M_{z,0}\sqrt{1+2\left(\frac{1}{D_x}+\frac{1}{D_y}\right)\frac{1}{\chi k_0}}} \tag{6.2.1}$$

For positive values of the transverse reactance the axial wavenumbers will be purely real. If the transverse reactance is negative, the critical value of the reactance is given by equation (6.1.2). If the absolute value of the transverse reactance is smaller than the critical value (i.e. less negative), the imaginary part of the axial wavenumbers is non-zero. If the absolute value of the transverse reactance is greater than the critical value (i.e. more negative) or if the transverse reactance is positive, the imaginary component of the axial wavenumbers is 0. The region of interest is

$$-\frac{a_0}{f\pi}\left(\frac{1}{D_x}+\frac{1}{D_y}\right) \le \chi < 0 \tag{6.2.2}$$

This region increases in size as the driving frequency decreases. Furthermore, the bigger the duct, the smaller the region. No matter what the driving frequency, sound speed, and duct dimensions are the imaginary part of the axial wavenumber will always be positive when it is non-zero. This is because the term in the radical will always be purely real. In the region described by equation (6.2.2) this term is negative. When one takes the square root of this number the result is always a positive number times the imaginary unit. Mathematically it comes out to:

$$\frac{k_0(\pm M_{z,0}\psi^2 + i\psi)}{1 + M_{z,0}^2\psi^2}, \psi > 0 \tag{6.2.3}$$

where ψ is the result of the square root described in the previous paragraph. Thus, if the impedances are purely reactive the system will always be spatially driven.

For fully complex transverse wall impedances, consider Figs. 6.2 and 6.3. These two figures are the counterparts of Fig. 6.1, but with a non-zero value for the transverse reactance. Fig. 6.2 has a transverse reactance equal to the characteristic impedance of air. The effect of the reactance is to shift the 'spike' to the left. Fig. 6.3 has a transverse equal to the negative characteristic impedance of air. Rather than move the spike, the negative reactance smoothed out the peaks considerably. For larger values of reactance these two effects are magnified. For large reactances the sign ceases to matter, as the overall result is the imaginary component of the axial wavenumbers are 0 for any value of the axial mean-flow Mach number.

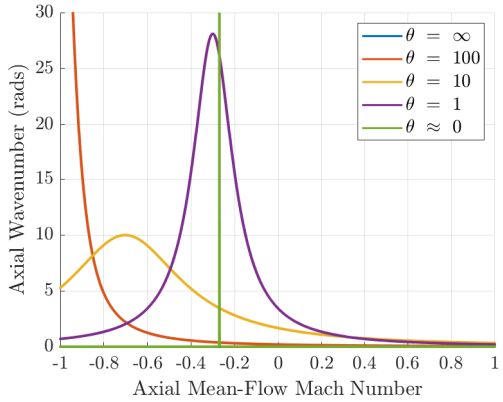

Figure 6.2: Imaginary Part of Forward Axial Wavenumber as a Function of Axial Mean-Flow Mach Number for Various Resistive Impedances with χ = +1

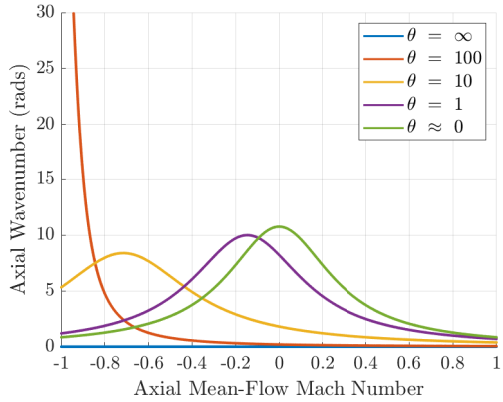

Figure 6.3: Imaginary Part of Forward Axial Wavenumber as a Function of Axial Mean-Flow Mach Number for Various Resistive Impedances with χ = -1

Figs. 5.78 and 5.79 show the pressure amplitude and phase, respectively for purely resistive transverse wall impedances. From section 5.1.3b it is known that resistive impedances effect both

the real and imaginary parts of the eigenfrequency. However, the effect on the real part is small until the impedance is close to the cut-off impedance value. For this duct, that cut-off impedance is $20/\pi$. Because the chosen resistive impedances are much larger than that, this frequency shifting is difficult to see in Fig. 5.78. However, if one looks closely at Fig. 5.78, the dashed-dotted curve which corresponds to $\theta = 50\rho_0 a_0$, the minimum appears to have shifted towards the right, which is the expected behavior as the eigenfrequency decreases. This is because as the eigenfrequency decreases the associated wavelength of that mode increases. Since the duct is fixed in length only so much of that mode can "fit" inside the duct. Thus, it appears that the nodes and anti-nodes of the given mode move towards the right end of the duct, z = 1 m. Because the real part of the eigenfrequency has not shifted very much, most of the decrease in amplitude is due to the damping from the negative imaginary part of the eigenfrequency. From Fig. 5.50, the imaginary part of the eigenfrequency becomes increasingly negative with decreasing resistive impedance, which is exactly what is seen in Fig. 5.78. The effect of resistive impedances on the pressure phase, Fig. 5.79, is the same as without mean-flow, i.e. the sharp jump around $z \approx 0.45$ meters is smoothed out. When compared directly with Fig. 5.27, Fig. 5.79 shows that the axial mean-flow overall increases the phase difference.

6.1.2c - Non-Zero Transverse Wall Mean-Flows

Next consider non-zero transverse mean-flows. As discussed in section 5.2.2c there are 3 possible scenarios: balanced transverse mean-flow, constant transverse mean-flow, and a general case.

The effect of the combination of axial and transverse mean-flows on the axial wavenumber is given by equation (5.2.18). The form of the axial wavenumber is very close to the baseline wavenumber, equation (5.2.6). The transverse mean-flow introduces a complex term equal to the impedance

parameter and scaled by the axial mean-flow in the same way as the baseline axial wavenumber. With the addition of an explicit imaginary term, the system experiences spatial damping/driving, depending on the sign of the impedance parameter. Thus, transverse mean-flows into the duct should cause damping, as they make the impedance parameter negative, while transverse mean-flows out of the duct should drive the system.

6.1.2d - Non-Zero Sub-Duct Temperature Difference

The axial wavenumber is given by

$$k_{z,1/2}^{\pm} = \frac{2\pi f / a_{0,1/2}}{1 \pm M_{z,0,1/2}} \tag{6.2.4}$$

This is essentially the same as equation (5.2.6), but now temperature dependent.

6.2 - General Trends

From the two example problems the CVA has been applied to it is abundantly clear that when multiple effects are included, making a sweeping generalization about the behavior of the system is difficult. Therefore, an analysis should be performed in order to understand a specific case. Nevertheless, there are certain general conclusions which can be drawn.

For finite transverse impedances the system can be driven or damped, depending on the signs and relative sizes of the transverse wall resistance and reactance. However, if the parameters considered are ‘realistic’ then finite transverse wall impedances will generally damp the system. With regards to the transverse wall impedances, there is one major drawback with this analysis. This analysis has been done without an impedance model. Therefore, trends which depend on the frequency and the axial and transverse mean-flows are expected to be inaccurate as the transverse

impedance depend on those parameters. However, it is straightforward to include an impedance model into this method.

Non-zero transverse wall impedances do not affect the eigenfrequency if the axial mean-flow is constant if mean-flows are the only effects considered. That is, if all the mean-flow that comes in through the transverse walls also leaves through other transverse walls, it does not change the eigenfrequency. This is a limitation of the CVA model in its current form. If a more robust boundary condition than the Myers-Ingard boundary condition were imposed on the transverse walls, then I suspect that the effect of any transverse mean-flow situation, even balanced, will have an appreciable effect on the eigenfrequencies. If any effect except axial mean-flow is considered in addition to transverse mean-flow, the previous observation does not hold. Even if the transverse mean-flow does not affect the eigenvalues, it can still cause spatial damping/driving or damping/driving in the frequency space. One of the most important effects of transverse mean-flow is the effect it has on the transverse mean-flow. If the transverse mean-flow is "un-balanced," it will influence the axial mean-flow. In this work, the effect is limited to the axial mean-flow in sub-duct 2. A good "ball-park" estimate is to simply look at the overall axial mean-flow in the duct and gauge any effect from the axial mean-flow alone.

The axial mean-flow has a very large effect on the system. However, the implementation of axial mean-flow for any application problem is highly dependent on the boundary conditions at the ends of the duct in the axial direction. In this work, the axial mean-flow will generally reduce the resonant frequencies and increase temporal damping in the system.

If one splits the duct into two and each sub-duct is at a different temperature the primary effect is an increase in the resonant frequency of the system. This makes sense, as one could imagine the average temperature of the duct increasing. This is because the temperature changes

the properties of the gas in the duct, most notably density and sound speed. A primary area where this comes into play is with the Mach numbers of the mean-flows, particularly the axial mean-flows. If the temperature is very high, small amounts of mean-flow coming into the system can cause the axial mean-flow, particularly in sub-duct 2, to become supersonic inside the duct. High Mach numbers most likely do not produce accurate results and is a main limiting factor in this analysis.

Chapter 7

Conclusions

The control volume analysis has been presented in this work. First the work was motivated from a combustion instability standpoint, but any acoustic problem in a simplified duct can be analyzed. Next the derivation of the method was laid out, followed by a presentation of the essential equations resulting from the analysis. Initial assessment of the analysis was done by comparing this method with duct acoustic methods presented by Munjal in *Acoustics of Ducts and Mufflers* [7]. Next the method was applied to two duct acoustics problems: a closed-closed duct and a constant mass flow-rate – nozzle duct. The two names denote the boundary conditions applied to the boundaries in the direction of wave-propagation. These results were discussed in detail in chapter 6.

Although what is shown here is detailed, a complete examination of the available parameter space would far too lengthy for this work. The aim of this work was to display the versatility and strength of the CVA. This method considers the effects of transverse impedance, transverse mean-flow, axial mean-flow, and sub-duct temperature differences all at once to provide sophisticated results unavailable to similar reduced order methods. The CVA is general enough to include non-uniform cross-sectional area ducts, although this was not chosen as an application problem in this thesis.

For all of benefits of the CVA method, there are limitations. The CVA assumes plane wave propagation. In combustors, fully 3D waves are present. This has been termed “low-frequency” throughout this work, and only refers to the transverse directions. Thus far, the CVA has only been carried out in a rectangular geometry, limiting its application to rectangular combustors. This analysis is also linear, and does not consider higher order effects, which are important when considering combustion instabilities. Finally, this method has not been compared with established numerical methods and experiments, a necessary next step.

7.1 - Future Work

The control volume analysis described in this thesis is still its infancy. There are several key steps to take to increase the usefulness of this model.

First and foremost, this model needs verification from experimental and numerical studies. Due to this methods flexibility, designing an experiment or simulation to compare with the CVA method presented here would be straightforward.

Second, impedance models need to be included to ensure accurate boundary conditions on the transverse walls.

Third, the corrections to the Myers-Ingard boundary mentioned in the introduction need to be incorporated, such as [24] or [25]. This further increases the fidelity of the results provided by the CVA.

Fourth, combustion models need to be included. This would change the matching conditions at the sub-duct boundary and introduce a heat release term, thus the energy equation would be needed. The inclusion of combustion models would be through the application of this method to problems which feature combustion.

Fifth, this CVA must be carried out on cylindrical and annular geometries to be more easily applicable to rockets and gas-turbines, respectively.

Sixth, fully utilizing the network model would allow the CVA to be applied to more complicated systems. For instance, it would be possible to create more complicated geometries by discretizing a variable cross-section duct, then combining each section with the same network model. In the same way one could include a 1D temperature gradient in the combustor.

Finally, is the possibility of allowing the axial mean-flow to be a function of the axial duct position, z. This would introduce an axial position dependence to the mean-flow, which would in turn cause the wavenumbers and eigenfrequency to also depend on the axial duct position. This will cause the transcendental equations solved in this method to become transcendental differential equations. An investigation into whether this added complexity would have a corresponding increase in accuracy, when one could simply discretize the change in axial mean-flow and use a network model using the current method.

References

[1] B. Higgins, "On the Sound Produced by a Current of Hydrogen Gas Passing Through a Tube," *Journal of Natural Philosophy, Chemistry, and the Arts,* vol. 1, pp. 129-131, February 1802.

[2] B. T. Zinn and T. C. Lieuwen, "Combustion Instabilities: Basic Concepts," in *Combustion Instabilities in Gas Turbine Engines: Operational Experience, Fundamental Mechanisms, and Modeling*, American Institute of Aeronautics and Astronautics, Inc., 2005, pp. 3-26.

[3] J. W. 3. B. R. Strutt, The Theory of Sound, London: Macmillan, 1877.

[4] G.-H. Y. C. L. Jiyuan Tu, Computational Fluid Dynamics: A Practical Approach, Cambridge: Elsevier, 2018.

[5] J. O'Connor, V. Acharya and T. Lieuwen, "Transverse Combustion Instabilities: Acoustic, Fluid Mechanic, and Flame Processes," *Progress in Energy and Combustion Science,* vol. 49, pp. 1-39, 2015.

[6] D. T. Blackstock, Fundamentals of Physical Acoustics, John Wiley & Sons, 2000.

[7] M. L. Munjal, Acoustics of Ducts and Mufflers with Application to Exhaust and Ventilation System Design, John Wiley & Sons, 1987.

[8] L. E. Kinsler, A. R. Frey, A. B. Coppens and J. V. Sanders, Fundamentals of Acoustics, John Wiley & Sons, 2000.

[9] H. Merk, "Analysis of Heat-Driven Oscillations of Gas Flows. I. General Considerations," *Applied Science Research,* pp. 317-335, 1956.

[10] G. Bloxsidge, A. Dowling and P. Langhorne, "Reheat Buzz: an Acoustically Coupled Combustion Instability," *Journal of Fluid Mechanics,* vol. 193, pp. 445-473, 1988.

[11] M. Heckl, "Active Control of the Noise from a Rijke Tube," *Journals of Sound and Vibration,* vol. 124, pp. 117-133, 1988.

[12] J. Keller, "Thermoacoustic Oscillations in Combustion Chamberes," *AIAA Journal,* vol. 33, no. 12, pp. 2280-2287, 1995.

[13] A. Putnam, Combustion-Driven Oscillations in Industry, New York: Elsevier, 1971.

[14] D. Bohn and E. Deuker, "An Acoustical Model to Predict Combustion Driven Oscillations," *20th International Congress on Combustion Engines,* 1993.

[15] S. Rienstra, "Solutions and Properties of the Pridmore-Brown Equations," *25th AIAA/CEAS Aeroacoustics Conference,* May 2019.

[16] K. U. Ingard, "Influence of Fluid Motion Past a Plane Boundary on Sound Reflection, Absorption and Transmission," *Journal of the Acoustical Society of America,* vol. 31, no. 7, pp. 1035-1036, 1959.

[17] M. Myers, "On the Acoustic Boundary Condition in the Presence of Flow," *Journal of Sound and Vibration,* vol. 71, no. 3, pp. 429-434, 1980.

[18] E. J. Brambley, "Fundamental Problems with the Model of Uniform Flow over Acoustic Linings," *Journal of Sound and VIbration,* vol. 322, pp. 1026-1037, 2009.

[19] Y. Renou and Y. Aurégan, "Failure of the Ingard-Myers Boundary Condition for a Lined Duct: An Experimental Investigation," *Journal of the Acoustical Society of America,* vol. 130, no. 1, pp. 52-60, 2011.

[20] E. Brambley, "Well-Posed Boundary Condition for Acoustic Liners in Straight Ducts with Flow," *AIAA Journal,* vol. 49, no. 6, pp. 1272-1282, 2011.

[21] S. Rienstra and M. Darau, "Boundary-Layer Thickness Effects of the Hydrodynamic Instability Along an Impedance Wall," *Journal of Fluid Mechanics,* vol. 671, pp. 559-573, 2011.

[22] Y. Aurégan, R. Starobinski and V. Pagneu, "Influence of Grazing Flow and Dissipation Effects on the Acoustic Boundary Conditions at a Lined Wall," *The Journal of the Acoustical Society of America,* vol. 109, no. 1, pp. 59-64, 2001.

[23] G. Gabard, "A Comparison of Impedance Boundary Conditions for Flow Acoustics," *Journal of Sound and Vibration,* vol. 332, pp. 714-724, 2013.

[24] D. Khamis and E. Brambley, "Acoustic Boundary Conditions at an Impedance Lining in Inviscid Shear Flow," *Journal of Fluid Mechanics,* vol. 796, pp. 386-416, 2016.

[25] D. Khamis and E. Brambley, "Viscous Effects on the Acoustics and Stability of a Shear Layer Over an Impedance Wall," *Journal of Fluid Mechanics,* vol. 810, pp. 489-534, 2017.

[26] D. Khamis and E. Brambley, "Viscous Effects on the Attenuation of a Plane Wave by an Acoustic Lining in Shear Flow," *The Journal of the Acoustical Society of America,* vol. 141, no. 4, pp. 2408-2417, 2017.

[27] T. Poinsot and D. Veynante, Theoretical and Numerical Combustion, Philadelphia: R.T. Edwards, 2001.

[28] U. Krüger, J. Hüren, S. Hoffman, W. Krebs, P. Flohr and D. Bohn, "Prediction and Measurement of Thermoacoustic Improvements in Gas Turbines with Annular Combustion Systems," *Journal of Engineering for Gas Turbines and Power,* vol. 123, pp. 557-556, 2001.

[29] W. Krebs, S. Bethke, J. Lepers and P. Flohr, "Thermoacoustic Design Tools and Passive Control: Siemens Power Generation Approaches," in *Combustion Instabilities in Gas Turbine Engines: Operational Experience, Fundamental Mechanisms, and Modeling*, American Institute of Aeronautics and Astronautics, 2005, pp. 89-112.

[30] A. Dowling and S. Stow, "Acoustic Analysis of Gas-Turbine Combustors," in *Combustion Instabilities in Gas Turbine Engines: Operational Experience, Fundamental Mechanisms, and Modeling*, Aerospace Institute of Aeronautics and Astronautics, 2005, pp. 369-414.

[31] G. Richards and D. Straub, "Passive Control of Combustion Instabilities in Stationary Gas Turbines," in *Combustion Instabilities in Gas Turbine Engines: Operational Experience, Fundamental Mechanisms, and Modeling*, American Institute of Aeronautics and Astronautics, 2005, pp. 533-579.

[32] C. Pankiewitz and T. Sattelmayer, "Time Domain Simulation of Combustion Instabilities in Annular Combustors," *J. Eng. Gas Turbines Power,* vol. 123, no. 3, pp. 677-685, 2003.

[33] A. Dowling, "The Calculation of Thermoacoustic Oscillations," *J. Sound. Vib.,* vol. 180, no. 4, pp. 557-581, 1995.

[34] J. Eckstein and T. Sattelmayer, "Low-Order Modeling of Low-Frequency Combustion Instabilities in AeroEngines," *Journal of Propulsion and Power,* vol. 22, no. 2, pp. 425-432, 2006.

[35] C. M. Institute, "Millenium Prize Problems - Navier-Stokes Equation," Clay Mathematics Institute, 27 March 2017. [Online]. Available: http://www.claymath.org/millennium-problems/navier%E2%80%93stokes-equation. [Accessed 19 7 2019].

[36] M. Lighthill, "On Sound Generated Aerodynamically I. General Theory," *Proceedings of the Royal Society,* vol. 211, no. 1107, 1952.

[37] F. Marble and S. Candel, "Acoustic Disturbance from Gas Non-Uniformities Convected Through a Nozzle," *Journal of Sound and Vibration,* vol. 55, no. 2, pp. 225-243, 1977.

[38] G. F. Roach, Green's Functions, Cambridge: Cambridge University Press, 1982.

[39] S. Evesque, A. Dowling and A. Annaswamy, "Adaptive Algorithms for Control of Combustion," *Proceedings of the AVT Symposium on Active Control Technology for Enhanced Performance Operation Capabilities,* p. 22, May 2000.